

REPORT DOCUMENTATION PAGE

Form Approved
OMB No. 0704-0188

Public reporting burden for this collection of information is estimated to average 1 hour per response, including the time for reviewing instructions, searching existing data sources, gathering and maintaining the data needed, and completing and reviewing the collection of information. Send comments regarding this burden estimate or any other aspect of this collection of information, including suggestions for reducing this burden, to Washington Headquarters Services, Directorate for Information Operations and Reports, 1215 Jefferson Davis Highway, Suite 1204, Arlington, VA 22202-4302, and to the Office of Management and Budget, Paperwork Reduction Project (0704-0188), Washington, DC 20503.

1. AGENCY USE ONLY (Leave blank)	2. REPORT DATE 1 MAY 1995	3. REPORT TYPE AND DATES COVERED Final Technical 1 JUL 93-31 DEC 94
----------------------------------	------------------------------	--

4. TITLE AND SUBTITLE Seismic Wave Radiation, Propagation and Event Location in Laterally Heterogeneous Media	5. FUNDING NUMBERS 2309/AS F49620-93-1-0424
--	---

6. AUTHOR(S) A. Ben-Menahem, M. Imhof, Y. Li, O. Mikhailov, W. Rodi, M.N. Toksöz	AFOSR-TR-93-0417
--	------------------

7. PERFORMING ORGANIZATION NAME(S) AND ADDRESS(ES) Massachusetts Institute of Technology 77 Massachusetts Avenue Cambridge, MA 02139	8. PERFORMING ORGANIZATION REPORT NUMBER 60441/60444
---	--

9. SPONSORING / MONITORING AGENCY NAME(S) AND ADDRESS(ES) AFOSR/NL 110 Duncan Avenue Suite B115 Bolling AFB DC 20332-0001 Dr. Stanley K. Dickinson	10. SPONSORING / MONITORING AGENCY REPORT NUMBER SELECTED JUN 16 1995 F
--	---

11. SUPPLEMENTARY NOTES

This document has been approved for public release and sale; its distribution is unlimited.

12. DISTRIBUTION / AVAILABILITY STATEMENT

Distribution Unlimited

19950614 062

13. ABSTRACT (Maximum 200 words)

Three studies related to nuclear monitoring and discrimination are reported. First, we present a new approach to modeling elastic wave scattering, based on multiple multipole expansions. Numerical examples demonstrate that the new algorithm is a very general tool for solving relatively large and complex two dimensional scattering problems. Second, we apply relative event location and waveform cross-correlation techniques to relocate four presumed nuclear explosions at the Balapan, Kazakhstan Test Site. The relative locations obtained from differential P and PcP arrival times at a small number of far-regional and teleseismic stations are more accurate than conventional seismic locations obtained with hundreds of arrival time picks. The third study addresses the effects of non-sphericity of an explosion cavity on seismic wave radiation. A new analytical technique is presented for computing the effects of cavities of arbitrary shape. The technique is applied to study far-field P and S wave radiation from explosions as a function of frequency.

DTIC QUALITY INSPECTED 3

14. SUBJECT TERMS Elastic wave scattering, multipole expansions, relative event location, non-spherical explosion cavities, nuclear discrimination	15. NUMBER OF PAGES 109
	16. PRICE CODE

17. SECURITY CLASSIFICATION OF REPORT Unclassified	18. SECURITY CLASSIFICATION OF THIS PAGE Unclassified	19. SECURITY CLASSIFICATION OF ABSTRACT Unclassified	20. LIMITATION OF ABSTRACT SAR
---	--	---	-----------------------------------

AFOSR/NL

SEISMIC WAVE RADIATION, PROPAGATION AND EVENT LOCATION
IN Laterally Heterogeneous Media

Ari Ben-Menahem
Matthias G. Imhof
Yingping Li
Oleg Mikhailov
William Rodi
M. Nafi Toksöz

Earth Resources Laboratory
Department of Earth, Atmospheric, and
Planetary Sciences
Massachusetts Institute of Technology
Cambridge, Massachusetts 02139

1 May 1995

Contract F49620-93-1-0424
Final Technical Report
July 1993 - December 1994

APPROVED FOR PUBLIC RELEASE; DISTRIBUTION UNLIMITED

Accession For	
NTIS CRA&I	<input checked="" type="checkbox"/>
DTIC TAB	<input type="checkbox"/>
Unannounced	<input type="checkbox"/>
Justification	
By	
Distribution /	
Availability Code	
Dist	Avail and/or Special
A-1	

TABLE OF CONTENTS

List of Contributing Scientists	v
List of Previous and Related Contracts	v
Bibliography of Publications Totally or Partially Supported by the Contract	vi
Preface	vii
Multiple Multipole Expansions for Elastic Scattering	1
Abstract	1
Introduction	2
Theoretical Background	3
Numerical Results	8
Discussion	12
Acknowledgments	14
References	15
Figures	17
Relocation of Explosions at the Balapan, Kazakhstan Test Site	27
Summary	27
Introduction	27
Data Processing	28
Relocation Results and Conclusions	33
References	35
Figures	37
Multipole Radiation of Seismic Waves from Explosions in Non-spherical Cavities and its Application fo Signal Identification	47
Abstract	48
Introduction	49
Spherical Mapping Approximation	53

Application to Realistic Cavity Shapes	58
Long-Wave Approximation and Corresponding Source Moment Tensor	60
Surface Waves from explosions in an Underground Cavity	65
Numerical Results for Radiation Patterns of Body and Surface Waves	69
Discussion	73
Acknowledgments	75
References	76
Legend of Figures	79
Appendix A: Fundamental Elastodynamic Vectors, Associated Functions, and Coordinate Transformation Relations	81
Appendix B: Quadrature of the Cavity Integrals	86
Figures	88

List of Contributing Scientists

Ari Ben-Menahem, Visiting Scientist, Massachusetts Institute of Technology

Richard L. Gibson, Jr., Research Scientist, Massachusetts Institute of Technology

Matthijs Haartsen, Graduate Research Assistant, Massachusetts Institute of Technology

Matthias G. Imhof, Graduate Research Assistant, Massachusetts Institute of Technology

Yingping Li, Postdoctoral Associate, Massachusetts Institute of Technology

Oleg Mikhailov, Graduate Research Assistant, Massachusetts Institute of Technology

William Rodi, Research Scientist, Massachusetts Institute of Technology

M. Nafi Toksöz, Professor of Geophysics, Massachusetts Institute of Technology

List of Previous and Related Contracts

DARPA/AFGL Contract F19628-89-K-0020, "Regional Seismograms: Attenuation and Scattering", July 1989 to June 1991.

DARPA/AFPL Contract F19628-90-K-0057, "Research in Regional Seismology: The Effect of Anisotropy", August 1990 to July 1992.

DARPA/AFPL Contract F29601-91-K-DB15, "Research on Monitoring at Regional Distances", September 1991 to September 1993.

AFOSR Contract F49620-92-J-0413, "Basic Research in Nuclear Test Monitoring", July 1992 to July 1994.

AFOSR Contract F49620-93-1-0424 "Seismic Wave Radiation, Propagation and Event Location in Laterally Heterogeneous Media", July 1993 to December 1994.

AFOSR Grant F49620-94-1-0282, "Effect of 3D Heterogeneities and Topography on Seismic Wave Propagation and the Use of Empirical Green's Functions for Source Characterization and Discrimination", May 1994 to November 1995.

AFOSR Grant F49620-94-1-0273, "Characterization of Seismic Sources Using Empirical Green's Functions", July 1994 to June 1997.

Bibliography of Publications Totally or Partially Sponsored by the Contract

- A. Ben-Menahem and O. Mikhailov, 1995. Multipole radiation of elastic body and surface waves from explosions in non-spherical cavities, submitted to *J. Acoust. Soc. Am.*
- M. Haartsen and M.N. Toksöz, 1994. A study of seismic/acoustic wave propagation through a laterally varying multi layered medium using the boundary-integral-equation discrete wavenumber method , *J. Acoust. Soc. Am.*, to appear.
- A. Ben-Menahem and R.L. Gibson, Jr., 1994. Radiation of elastic waves from sources embedded in anisotropic inclusions, *Geophys. J. Int.*, accepted.
- M.G. Imhof, 1995. Multiple multipole expansions for acoustic scattering, *J. Acoust. Soc. Am.*, **97**, 754-763.
- M.G. Imhof, 1995. Multiple multipole expansions for elastic scattering, *J. Acoust. Soc. Am.*, submitted.
- Y. Li, M.N. Toksöz and W. Rodi, 1995, Source time functions of nuclear explosions and earthquakes in central Asia determined using empirical Green's functions, *J. Geophys. Res.*, 100, 659-674.
- Y. Li, W. Rodi and M. N. Toksöz, 1994, Seismic source characterization with empirical Green's function and relative location techniques, Proceedings of the 16th Annual Seismic Research Symposium, Thornwood, New York, Air Force Phillips Laboratory, 231-237.

PREFACE

The project on which we report here had three objectives. The first was to develop new methods for modeling regional wave propagation in laterally heterogeneous media. Toward this end we developed some new computational techniques for seismic wave scattering based on the boundary element method and multipole expansions. In this report we include a preprint of a paper entitled, "Multiple multipole expansions for elastic scattering," which has been submitted to *Journal of the Acoustical Society of America*. The second objective was to develop techniques for relative event location and apply them to problems of nuclear monitoring. The second part of this report is the application of a relative event location method we developed, based on waveform cross-correlation, to the location of presumed explosions at the Balapan, Kazakhstan Test Site. Events at this test site have been located very accurately on the basis of satellite images, and this provides the opportunity to test the accuracy of our approach and compare it to the location accuracy achievable with conventional seismic techniques. Our third objective was to study the effects of non-spherical cavities on the seismic wave radiation from explosions. The final section of this report is a preprint of a paper, "Multipole radiation of seismic waves from explosions in non-spherical cavities," which will appear in the *Journal of the Acoustical Society of America*.

MULTIPLE MULTIPOLE EXPANSIONS FOR ELASTIC SCATTERING

Matthias G. Imhof

Earth Resources Laboratory

Department of Earth, Atmospheric, and Planetary Sciences

Massachusetts Institute of Technology

42 Carleton Street

Cambridge, MA 02142 - 1324

ABSTRACT

The paper presents a new approach to solve scattering of elastic waves in two dimensions. Traditionally, wave fields are expanded into an orthogonal set of basis functions. Unfortunately, these expansions converge rather slowly for complex geometries. The new approach enhances convergence by summing multiple expansions with different centers of expansions. This allows irregularities of the boundary to be resolved locally from the neighboring center of expansion. Mathematically, the wavefields are expanded into a set of non-orthogonal basis functions. The incident wavefield and the fields induced by the scatterers are matched by evaluating the boundary conditions at discrete matching points along the domain boundaries. Due to the non-orthogonal expansions, more matching points are used than actually needed resulting in an overdetermined system which is solved in the least squares sense.

Since there are free parameters such as location and number of expansion centers as well as kind and orders of expansion functions used, numerical experiments are performed to measure the performance of different discretizations. An empirical set of rules governing the choice of these

parameters is found from these experiments. The resulting algorithm is a very general tool to solve relatively large and complex two-dimensional scattering problems.

INTRODUCTION

The calculation of synthetic seismograms has been of interest for many years. Various methods have been proposed for modeling waves in heterogeneous media. Each of them has its own range of validity and interest. Fully numerical techniques in the space-time domain, either in the finite difference formulation (Kelly *et al.*, 1976; Virieux, 1986) (FD) or in the finite element formulation (Smith, 1974) (FE), handle any kind of waves in complex media. Unfortunately, they are limited due to computer memory and runtime considerations, since for many problems the distances between scatterer, source and receiver are large. An area containing the source, the receiver and the scatterers plus a substantial neighborhood around them has to be discretized, which might result in prohibitive computation times. The (generalized) ray theory (Červený *et al.*, 1977; Hong and Helmberger, 1978; Červený and Pšenčík, 1984) can be used when the scatterers and their radii of curvature are large compared to the wavelength. For small or weak scatterers, the Born approximation (Miles, 1960) allows an efficient calculation of the seismogram.

In other cases, the problem can be simplified by assuming the medium to consist of homogeneous regions with sharp boundaries inbetween. Then, reflectivity (Müller, 1985; Kennett, 1983) and global matrix methods (Chin *et al.*, 1984) are routinely used for planarly or cylindrically layered media. For laterally heterogeneous media, numerical integration over wavenumber can be used (Aki and Larner, 1970; Bouchon and Aki, 1977; Haartsen *et al.*, 1994). In the elastic case, the classical eigenfunction expansion (Morse and Feshbach, 1953) (SMP) allows the analysis only of simple shapes such as circular cylinders or spheres since the eigenmodes do not decouple otherwise (Pao and Mow, 1973). Methods based on the perturbation of a prescribed geometry, such as the T-matrix method (Waterman, 1976; Boström, 1980) work extremely well for certain geometries but are harder to apply efficiently in general situations.

The method we present is a derivative of the boundary element methods (Brebbia and Dominguez, 1989) (BEM). It was first presented as a more general approach for electromagnetic scattering (Ballisti and Hafner, 1983; Hafner, 1990) and later adapted to acoustic scattering problems (Imhof, 1995). In contrast to more traditional approaches, the wavefields are expanded into a set of *non-*

orthogonal and *non-complete* basis-functions. Actually, non-complete basis-functions are not a new concept since for numerical and computational reasons we can never use infinitely many basis-functions. But the application of a non-orthogonal expansion allows the reduction of the truncation errors (Hafner, 1993).

To solve for the unknown weighting coefficients of the basis-functions, discrete matching points are chosen along the boundary of the scattering object. In the elastic case, each matching point provides four boundary conditions and thus four equations involving the unknowns. Because the expansion is non-orthogonal, we require more equations than unknowns, build an overdetermined matrix system and solve it the *least-squares sense*. Mathematically speaking, we search for the set of weighting coefficients which solves the problem at hand “best” employing the expansions chosen. There will always be an error in the boundary conditions at each matching point, though on the average these errors are small. Furthermore, the fields in between matching points are forced to be smooth, such that no wild jumps or oscillations can occur. Thus, as an added bonus, we control the behavior of the expansions in between matching points where we have no control using traditional methods. Also, this allows us to see in which parts of the boundary the expansions chosen can solve the problem and where they need further refinement.

This paper will be structured as follows: First, we will adapt the method from acoustical (Imhof, 1995) to elastic scattering. Then we present results from several calculations and compare them to solutions obtained by the finite difference method and the classical eigenfunction expansion. We show how different discretizations affect the solution. Finally, we will compile these findings into an empirical set of rules which allows us to set a problem up in a fashion which yields satisfactory results without having to do it on a trial and error basis.

THEORETICAL BACKGROUND

We would like to model how an incident wavefield $\vec{u}^{inc}(\vec{x}, \omega)$ scatters from an object. The situation is depicted in Figure 1. For the sake of clarity, we will suppress the time factor $e^{-i\omega t}$ in all following expressions. Superscripts denote the region to which a material property or fields belongs to, and, to distinguish different regions or domains, we use the symbol Γ^d . The boundary between the two regions Γ^0 and Γ^1 will be denoted by $\partial\Gamma_{01}$. We also call the region Γ^0 the background and define Γ^1 to be the scatterer.

In the frequency domain, elastic P-SV waves travelling in a two-dimensional, homogeneous medium are described by (Pao and Mow, 1973)

$$\frac{1}{k^2} \nabla \nabla \cdot \vec{u} - \frac{1}{l^2} \nabla \times \nabla \times \vec{u} + \vec{u} = 0 \quad (1)$$

where we defined the wave vectors $k = \omega/\alpha$ and $l = \omega/\beta$ for a particular frequency ω and the propagation velocities $\alpha = \sqrt{\lambda + 2\mu/\rho}$ and $\beta = \sqrt{\mu/\rho}$. The parameter ρ , λ and μ denote the density and the Lamé parameters of the medium, respectively.

In a local cylindrical coordinate system (r, θ, y) centered at a point \vec{x}_p (Figure 2), the strains due to a displacement \vec{u} are expressed as (Pao and Mow, 1973)

$$\epsilon_{rr} = \frac{\partial u_r}{\partial r} \quad (2a)$$

$$\epsilon_{\theta\theta} = \frac{\partial u_\theta}{\partial \theta} + \frac{\partial u_r}{\partial r} \quad (2b)$$

$$\epsilon_{r\theta} = \epsilon_{\theta r} = \frac{1}{2} \left(\frac{1}{r} \frac{\partial u_r}{\partial \theta} + \frac{\partial u_\theta}{\partial r} - \frac{u_\theta}{r} \right) \quad (2c)$$

All other components are zero since they involve the u_y component or cross-derivatives with respect to y . Thus, the stresses are linearly related to the strains by (Pao and Mow, 1973)

$$\sigma_{pq} = \lambda \delta_{pq} \sum_k \epsilon_{kk} + 2\mu \epsilon_{pq} \quad \text{where} \quad p, q \in \{r, \theta\} \quad (3)$$

A displacement field $\vec{u}^{inc}(\vec{x})$ incident on the scatterer will induce two scattered fields: $\vec{u}^0(\vec{x}, \omega)$ outside the scattering object and $\vec{u}^1(\vec{x}, \omega)$ on the inside. The displacements and stresses inside and outside the scatterer are related by the boundary conditions. For the problem posed, these conditions are continuities of displacement and stresses in both normal and tangential direction. We define the normal \hat{n} to point from medium Γ^0 into medium Γ^1 as depicted in Figure 2. Using the subscripts n and t to denote the normal and tangential direction, we write

$$u_n^0 + u_n^{inc} = u_n^1 \quad (4a)$$

$$u_t^0 + u_t^{inc} = u_t^1 \quad (4b)$$

$$\sigma_{nn}^0 + \sigma_{nn}^{inc} = \sigma_{nn}^1 \quad (4c)$$

$$\sigma_{nt}^0 + \sigma_{nt}^{inc} = \sigma_{nt}^1 \quad (4d)$$

Since we express the displacements and stresses in a local cylindrical coordinate system (r, θ, y) , but want to specify the boundary in a local cartesian system (n, t, y) , we have use the rotation

matrix \mathbf{M} to transform the individual components

$$\vec{u}^{nty} = \mathbf{M} \cdot \vec{u}^{r\theta y} \quad (5)$$

$$\sigma^{nty} = \mathbf{M} \cdot \sigma^{r\theta y} \cdot \mathbf{M}^T \quad (6)$$

where the rotation matrix \mathbf{M} is defined by the unit vectors \hat{r} , $\hat{\theta}$, \hat{n} and \hat{t} .

$$\mathbf{M} = \begin{pmatrix} \hat{n} \cdot \hat{r} & \hat{n} \cdot \hat{\theta} & 0 \\ \hat{t} \cdot \hat{r} & \hat{t} \cdot \hat{\theta} & 0 \\ 0 & 0 & 1 \end{pmatrix} \quad (7)$$

Instead of using the displacement \vec{u} directly, we break it into two parts

$$\vec{u}(\vec{x}) = \nabla \Phi(\vec{x}) + \nabla \times \{\Psi(\vec{x})\hat{y}\} \quad (8)$$

using the scalar potentials $\Phi(\vec{x})$ and $\Psi(\vec{x})$. Then, equation (1) separates into two independent Helmholtz equations:

$$(\nabla^2 + k^2) \Phi(\vec{x}, \omega) = 0 \quad (9a)$$

$$(\nabla^2 + l^2) \Psi(\vec{x}, \omega) = 0 \quad (9b)$$

Therefore, we replace the induced displacement fields $\vec{u}^0(\vec{x}, \omega)$ and $\vec{u}^1(\vec{x}, \omega)$ by the potentials $\Phi^0(\vec{x}, \omega)$, $\Psi^0(\vec{x}, \omega)$, $\Phi^1(\vec{x}, \omega)$ and $\Psi^1(\vec{x}, \omega)$. Similar to the acoustic case (Imhof, 1995), we expand the potential fields as:

$$\Phi^d(\vec{x}, \omega) = \sum_{p=0}^P \sum_{n=-N}^{+N} a_{pn}^d \phi_{pn}^d(\vec{x}, \vec{x}_p^d, k^d, \omega) + e_{\Phi}^d \quad (10a)$$

$$\Psi^d(\vec{x}, \omega) = \sum_{p=0}^P \sum_{n=-N}^{+N} b_{pn}^d \psi_{pn}^d(\vec{x}, \vec{x}_p^d, l^d, \omega) + e_{\Psi}^d \quad (10b)$$

where $\phi_{pn}^d(\vec{x}, \vec{x}_p^d, k^d, \omega)$ and $\psi_{pn}^d(\vec{x}, \vec{x}_p^d, l^d, \omega)$ are solutions to either Helmholtz equation (9a) or (9b), respectively. The error terms e_{Φ}^d and e_{Ψ}^d are included not only since the series are truncated after $\pm N$ terms but also because an expansion of this form is mathematically *non-orthogonal*.

An expansion of the form (10a) or (10b) is known as a multiple multipole (MMP) expansion (Ballisti and Hafner, 1983; Hafner, 1990). Setting P to zero yields the classical eigenfunction

(SMP) expansion (Morse and Feshbach, 1953). In the background region Γ^0 , we choose propagatory solutions for the expansion functions ϕ_{pn}^0 and ψ_{pn}^0 :

$$\phi_{pn}^0(\vec{x}, \vec{x}_p^0, k^0, \omega) = H_{|n|}^{(1)}(k^0 |\vec{x} - \vec{x}_p^0|) e^{in\theta} \quad (11a)$$

$$\psi_{pn}^0(\vec{x}, \vec{x}_p^0, l^0, \omega) = H_{|n|}^{(1)}(l^0 |\vec{x} - \vec{x}_p^0|) e^{in\theta} \quad (11b)$$

For the sake of clarity, the notation \vec{x}_p^1 for an expansion center means the p^{th} center for the expansions of $\Phi^1(\vec{x}, \omega)$ and $\Psi^1(\vec{x}, \omega)$. The location is not fixed yet. We can either set the center \vec{x}_p^1 *inside the scatterer* Γ^1 and thus $\vec{x}_p^1 \in \Gamma^1$ or we can place it *in the background* ($\vec{x}_p^1 \in \Gamma^0$). For a finite scatterer Γ^1 , we have two possible choices for the expansions of the fields $\Phi^1(\vec{x}, \omega)$ and $\Psi^1(\vec{x}, \omega)$. First, we can place the expansion centers into the scatterer itself ($\vec{x}_p^1 \in \Gamma^1$) and use expansions involving the Bessel solutions $J_{|n|} e^{in\theta}$ corresponding to standing waves (Morse and Feshbach, 1953).

$$\phi_{pn}^1(\vec{x}, \vec{x}_p^1, k^1, \omega) = J_{|n|}(k^1 |\vec{x} - \vec{x}_p^1|) e^{in\theta} \quad \text{if } \vec{x}_p^1 \in \Gamma^1 \quad (12a)$$

$$\psi_{pn}^1(\vec{x}, \vec{x}_p^1, l^1, \omega) = J_{|n|}(l^1 |\vec{x} - \vec{x}_p^1|) e^{in\theta} \quad \text{if } \vec{x}_p^1 \in \Gamma^1 \quad (12b)$$

Second, we can place the the expansion centers into the background ($\vec{x}_p^1 \in \Gamma^0$) and use propagatory solutions $H_{|n|}^1 e^{in\theta}$ involving the Hankel functions of the first kind.

$$\phi_{pn}^1(\vec{x}, \vec{x}_p^1, k^1, \omega) = H_{|n|}^{(1)}(k^1 |\vec{x} - \vec{x}_p^1|) e^{in\theta} \quad \text{if } \vec{x}_p^1 \in \Gamma^0 \quad (13a)$$

$$\psi_{pn}^1(\vec{x}, \vec{x}_p^1, l^1, \omega) = H_{|n|}^{(1)}(l^1 |\vec{x} - \vec{x}_p^1|) e^{in\theta} \quad \text{if } \vec{x}_p^1 \in \Gamma^0 \quad (13b)$$

These expansions represent waves propagating from the expansion center toward the scatterer (Morse and Feshbach, 1953). In the scatterer, we need waves propagating in all the directions. Thus, we place expansion centers all around the scatterer and “illuminate” the region Γ^1 from all sides.

To emphasize the difference between the expansions (12) and (13): if \vec{x}_p^1 is placed inside the scatterer Γ^1 , then we have to use (12) because the Bessel solutions $J_{|n|} e^{in\theta}$ represent standing waves. Contrary to the Hankel solutions, the Bessel solutions do not have a singularity at their origin. Expansion functions involving Hankel functions $H_{|n|}^{(1)}$ may never be used for the wavefields of the domain in which their expansion center \vec{x}_p is located in since the singularities at the origin represent sources. But by definition, the only source in the problem posed is the incident field

\vec{u}^{inc} . But if \vec{x}_p^1 is located outside the scatterer, then we have to use (13) with the Hankel solutions $H_{|n|}^{(1)} e^{in\theta}$ representing wavefields propagating towards the scatterer. The singularities pose no problem anymore since they are not located in the domain Γ^1 . Figure 3 illustrates this subtlety.

We solve for the unknown coefficients a_{pn}^d and b_{pn}^d by enforcing the boundary conditions (4a) - (4d) on M discrete matching points \vec{x}_m along the domain boundary $\partial\Gamma_{01}$. Since we have four boundary conditions, each matching point also provides four rows of the linear matrix system. Altogether, we have $4J = 2 \cdot 2 \cdot P \cdot (2N + 1)$ unknown coefficients a_{pn}^d, b_{pn}^d . To simplify the notation, we eliminate an index by sequentially renumbering the double-indexed expansion functions $\phi_{pn}^d(\vec{x}, \vec{x}_p^d, k^d, \omega)$ and the coefficients a_{pn}^d which results in $\phi_j^d(\vec{x}, \vec{x}_j^d, k^d, \omega)$ and a_j^d , respectively. The same is done with the $\psi_{pn}^d(\vec{x}, \vec{x}_p^d, l^d, \omega)$ and the coefficients b_{pn}^d resulting in $\psi_j^d(\vec{x}, \vec{x}_j^d, l^d, \omega)$ and b_j^d , respectively. Putting all together, we have to solve a matrix system of the form

$$\begin{pmatrix} -\Phi_n^0 & -\Psi_n^0 & \Phi_n^1 & \Psi_n^1 \\ -\Phi_t^0 & -\Psi_t^0 & \Phi_t^1 & \Psi_t^1 \\ -\Phi_{nn}^0 & -\Psi_{nn}^0 & \Phi_{nn}^1 & \Psi_{nn}^1 \\ -\Phi_{nt}^0 & -\Psi_{nt}^0 & \Phi_{nt}^1 & \Psi_{nt}^1 \end{pmatrix}_{4M \times 4J} \cdot \begin{pmatrix} \bar{a}^0 \\ \bar{b}^0 \\ \bar{a}^1 \\ \bar{b}^1 \end{pmatrix}_{4J} = \begin{pmatrix} \bar{u}_n \\ \bar{u}_t \\ \bar{\sigma}_{nn} \\ \bar{\sigma}_{nt} \end{pmatrix}_{4M} + \begin{pmatrix} \bar{e}_n \\ \bar{e}_t \\ \bar{e}_{nn} \\ \bar{e}_{nt} \end{pmatrix}_{4M} \quad (14)$$

where we used the submatrices Φ_n^d and Ψ_n^d to denote the normal displacements u_n at the matching points due to ϕ_j^d and ψ_j^d , respectively. The submatrices Φ_t^d and Ψ_t^d are the same but for the tangential displacements u_t . The submatrices Φ_{nn}^d and Ψ_{nn}^d contain the normal stresses σ_{nn} , while Φ_{nt}^d and Ψ_{nt}^d contain the tangential stresses σ_{nt} .

Defining the matching points by their location \vec{x}_m , we can write these submatrices as

$$\Phi_{n,mj}^d = u_n(\phi_j^d(\vec{x}_m)) \quad \Psi_{n,mj}^d = u_n(\psi_j^d(\vec{x}_m)) \quad (15a)$$

$$\Phi_{t,mj}^d = u_t(\phi_j^d(\vec{x}_m)) \quad \Psi_{t,mj}^d = u_t(\psi_j^d(\vec{x}_m)) \quad (15b)$$

$$\Phi_{nn,mj}^d = \sigma_{nn}(\phi_j^d(\vec{x}_m)) \quad \Psi_{nn,mj}^d = \sigma_{nn}(\psi_j^d(\vec{x}_m)) \quad (15c)$$

$$\Phi_{nt,mj}^d = \sigma_{nt}(\phi_j^d(\vec{x}_m)) \quad \Psi_{nt,mj}^d = \sigma_{nt}(\psi_j^d(\vec{x}_m)) \quad (15d)$$

where we used the index $m \in \{1, \dots, M\}$ to denote the matching points \vec{x}_m , the index $j \in \{1, \dots, J\}$ for the expansion functions ϕ_j^d, ψ_j^d and the index $d \in \{0, 1\}$ for the domain. The notation $u_n(\phi_j^d(\vec{x}_m))$ stands for the normal displacement due to the expansion function ϕ_j^d evaluated at the matching point \vec{x}_m . The other ones are to be interpreted similarly.

The vectors \bar{a}^0 , \bar{b}^0 , \bar{a}^1 and \bar{b}^1 in equation (14) contain the unknown coefficients a_j^0 , b_j^1 , a_j^1 , b_j^1 for the expansion functions ϕ_j^0 , ψ_j^0 , ϕ_j^1 and ψ_j^1 , respectively. The vectors \bar{u}_n , \bar{u}_t , $\bar{\sigma}_{nn}$, and $\bar{\sigma}_{nt}$ hold the normal and tangential displacements as well as normal and tangential stress at the M matching points due to the incident field \vec{u}^{inc} .

$$u_{n,m} = u_n^{inc}(\vec{x}_m) \qquad u_{t,m} = u_t^{inc}(\vec{x}_m) \qquad (16a)$$

$$\sigma_{nn,m} = \sigma_{nn}^{inc}(\vec{x}_m) \qquad \sigma_{nt,m} = \sigma_{nt}^{inc}(\vec{x}_m) \qquad (16b)$$

Finally, the matrix equation (14) contains the residual vectors \bar{e}_n , \bar{e}_t , \bar{e}_{nn} , \bar{e}_{nt} with the misfit of the boundary conditions at the individual matching points.

NUMERICAL RESULTS

To reduce numerical noise, we make the materials slightly lossy by adding a small imaginary component ω_I to the frequency (Bouchon and Aki, 1977). Thus, we have to evaluate Bessel functions with a complex argument (Amos, 1986). After the transformation from the frequency domain into the time domain, we recover the true amplitude by a multiplication with $e^{\omega_I t}$. The matrix system is solved by QR decomposition using Givens rotations (Wilkinson, 1988) which allows to build the matrix system row by row while only a triangular matrix with dimensions of the number of unknowns has to be kept in memory (George and Heath, 1980). Since we want to calculate synthetic seismograms using a frequency domain method, we have to solve the scattering problem for a range of frequencies and later apply a Fourier transformation to obtain the seismograms. All these problems can be solved independently of each other. Consequently, the algorithm is implemented on an nCUBE2 parallel computer where each processor will calculate a few frequencies.

We will now show how the method performs solving a very simple problem using different ways to discretize it. For the sake of simplicity, the incident field \vec{u}^{inc} is an explosive line source modulated with a Ricker wavelet (Hosken, 1988; Paillet and Cheng, 1991) of 50 Hz center frequency. Altogether, 64 receivers will measure the u_z component of the scattered field \vec{u}^0 in the background.

The rather generic scatterer is depicted in Figure 4. Its size is roughly 240m in length and 50m thickness. The velocities in the background are $\alpha^0 = 2000\text{m/s}$ and $\beta^0 = 1155\text{m/s}$, while in the scatterer they are $\alpha^1 = 3000\text{m/s}$ and $\beta^1 = 1732\text{m/s}$. Thus, the Poisson's ratio is the same for both regions ($\sigma = 0.25$). To facilitate the comparison with a solution obtained by finite differences,

the density $\rho = \rho^0 = \rho^1$ is kept constant at 2000kg/m^3 . The center frequency of 50Hz yields wavelengths of essentially of same size as the scatterer.

In order to have a reference seismogram to compare the different solutions with, we calculate the solution using a finite difference (FD) method (Kelly *et al.*, 1976; Peng and Toksöz, 1994). The resulting reference seismogram is shown in Figure 5. As a measure of how well the MMP seismogram $u_z^{MMP}(r, t)$ correlates with the FD reference seismogram $u_z^{FD}(r, t)$, we define the root mean square error RMS by summing over the squared difference between the two seismograms

$$\text{RMS} = \frac{1}{\sqrt{RT}} \sqrt{\sum_{r=1}^R \sum_{t=1}^T \{u_z^{MMP}(r, t) - u_z^{FD}(r, t)\}^2} \quad (17)$$

where $u_z(r, t)$ denotes the vertical displacement measured at recorder r at time sample t . $R = 64$ is the number of recorders and $T = 256$ is the total number of time samples.

MMP versus the Finite Difference Reference Solution

As a first example, we show both a solution obtained by MMP expansions and the reference solution as obtained by finite differences. For the finite difference case, we used a grid spacing of 1m and a grid of 750 by 750 points. The grid dimensions are larger than needed to prevent any reflection from the boundaries to reach the receivers. The timestep was 0.05ms. The runtime on a nCUBE2 using 64 nodes was 23 minutes. The seismogram calculated by finite differences is presented in Figure 5.

For the MMP expansion, we used a total of 256 expansion functions, 128 matching points, 8 expansion centers and 64 frequencies. The resulting runtime on a nCUBE2 using again 64 nodes was 12 minutes. The two methods yield very similar results. Figure 6 shows the seismogram calculated using the MMP expansion. As can be seen, they agree very well in both traveltimes and phases.

Effect of the Number of Expansion Functions

As a second experiment, we study how the number of expansion functions affects the solutions obtained. We start with totally 32 expansion functions located at 8 expansion centers. Thus, we have one monopole for each potential and each region at every expansion center.

We calculate the resulting seismogram and estimate the RMS error. Then we double the number of expansion functions per expansion center, calculate the seismograms anew, estimate the RMS error and so on until 1024 expansion functions are used. The number of matching points is kept constant at $M = 1024$ while the number of expansion centers is kept constant at $P = 8$. Figure 7 shows the resulting RMS error as a function of the total number of expansion functions used. A first observation is that 256 expansion functions seems to be the critical amount. Using fewer yields solutions which cannot capture important features of the reference seismogram, the solutions do not converge. Figure 8 shows a seismogram which is typical for a not converged solution. The seismogram was obtained with 64 expansion functions. For more than 256 expansion functions, we have convergence where RMS error decreases slowly with increasing number of expansions functions.

MMP versus SMP Expansion

The next numerical experiment we perform is to show the enhanced convergence of the MMP expansion compared to the classical eigenfunction expansion (SMP). As mentioned priorly, the eigenfunction expansion corresponds to an expansion (10a) or (10b) with only one expansion center. Thus, we perform the same experiment as before but use only one expansion center. Again, we start with one expansion function per domain and potential which yields totally 4 expansion functions. We calculate the resulting seismograms and estimate the RMS error. The resulting seismogram is presented in Figure 9. The seismogram is clean enough to be mistaken as correct but has no resemblance with the reference solution shown in Figure 5. Then we double the number of expansion functions per expansion center, calculate the seismograms, estimate the RMS error and so on. The number of matching points is kept constant at $M = 1024$.

Figure 7 shows the resulting RMS error as a function of the total number of expansion functions used. We notice that the MMP expansion using 8 expansion centers always performs better. Unfortunately, using more than 256 expansion functions in the SMP expansion yields no useful result anymore because the expansion functions of higher order violate the sampling condition (Hafner, 1990; Imhof, 1995). The maximum order N^{max} of a multipole is given by the largest angle φ^{max} between any two adjacent matching points and the location of the multipole:

$$N^{max} < \frac{\pi}{\varphi^{max}} \quad (18)$$

The increased error in the SMP expansion for 32 and 64 expansion function is an effect of the

error measure (17) which cannot account for phase shifts. Contrary to the MMP expansion, a SMP expansion cannot solve the problem posed in Figure 5.

Effect of Number and Location of Expansion Centers

The next numerical experiment is to examine the importance and effect of the number, location and distribution of expansion centers. As priorly mentioned, we have the choice of placing the expansion centers for the $\Phi^1(\vec{x}, \omega)$ and $\Psi^1(\vec{x}, \omega)$ fields either in- or outside the scatterer and thus expanding either into standing waves $J_{|n|}(kr) e^{in\theta}$ or into propagating waves $H_{|n|}^{(1)}(kr) e^{in\theta}$, respectively. We will use both to study the difference.

We calculate the solutions for a range of expansion centers while keeping the total number of expansion functions constant at 256. Also, the number of matching points is kept constant at 256. The overall computational effort to calculate one seismogram is kept constant. The resulting RMS errors are shown in Figure 10. It is surprising how broad the ‘U’ shaped minimal-error region is. The range from 4 up to 17 expansion centers converges. Indeed, the minimal RMS error obtained by 11 expansion center is only slightly better any other discretization employing 4 to 17 centers. Remarkably, MMP expansions seem to be very insensitive to the discretization used! Neither the number of expansion centers nor the kind of expansions changes the RMS errors by much, although the use of $H_{|n|}^{(1)}(kr) e^{in\theta}$ produces a smoother RMS error curve.

The pathological case with 23 expansion centers shows that the RMS error finally increases when more and more expansion centers are used. In this particular case, the expansion centers were separated by only a quarter of the dominant wavelength. The different expansion functions begin to interact by approximating higher order solutions to the wave equation: it is well known that two monopoles of opposite sign placed closely together are equivalent to a dipole. Thus, the matrix system becomes more and more ill-conditioned since each expansion center could be replaced by the adjacent ones. Moreover, we add more and more similar equations to the matrix system which renders it more and more ill-conditioned.

For comparison, we also use a simple boundary element (BEM) discretization with the same number of matching points and expansion functions. Along the boundary inbetween matching points, we place rotational and compressional monopole sources. As in the MMP cases, we use point matching and solve the system in the least-squares sense. The resulting large RMS error

indicates that the seismogram obtained is not correct. Indeed, it contains mainly the reflections from the top of the scatterer. Both reflections from the bottom and internal multiple scattering are mostly missing.

Effect of the Number of Matching Points

The last numerical experiment examines how the number of matching points affects the solutions. Actually, not the number of matching points but the ratio between the total number of equations in the matrix system and the number of expansion functions used is the important parameter. In accordance with the earlier experiments, we choose 12 expansion centers and keep the number of expansion functions constant at 256. Since each matching point provides 4 equations (one for each boundary condition), we start out with 64 matching points along the boundary which provide 256 equations altogether. We calculate the resulting seismogram, estimate the RMS error, double the number of matching points and so on. Figure 11 shows the RMS error against the number of equations per expansion function. Since the expansion is non-orthogonal, it is not surprising that we get a large RMS error when we use as many equations as we have unknowns. Using twice as many equations as unknowns provides the optimal result. Afterwards, the more equations we add, the more the RMS increases since the matrix system becomes more ill-conditioned with each additional equation we add. The result is more errors due to roundoff and other numerical effects.

Using twice as many equations as unknowns yields a distance of 4m between matching points. This spacing corresponds to 10 matching points per dominant wavelength (40m). Assuming that the highest frequency in the propagating seismic wavelet is 3 times the center frequency of 50Hz, the boundary is sampled with 3 matching points per wavelength for the highest frequency. The sampling theorem which states that the boundary has to be sampled at least twice per wavelength to prevent aliasing (Bouchon and Aki, 1977), is just satisfied. Thus, it is also theoretically reasonable to have about 10 matching points per dominant wavelength.

DISCUSSION

Combining these numerical experiments with prior experiences with electromagnetic (Hafner, 1990) and acoustical MMP methods (Imhof, 1995), we obtain a set of empirical rules how to discretize elastic scattering problems. A very important parameter is the radius of greatest influence of a

multipole which is $\sqrt{2}$ times the distance between the center of expansion and the closest matching point.

- The radius of greatest influence should be on the order of the dominant wavelength.
- No expansion center should be within the radius of greatest influence of any other expansion center.
- There should be ≈ 10 matching points per dominant wavelength
- There has to be at least half a matching point per expansion function or similarly two equations per expansion function.
- The maximum order N of a multipole is given by the sampling theorem: $N < \pi/\varphi^{max}$
- Expansions of the form $H_{|n|}^{(1)}(kr) e^{in\theta}$ should not be used for the region their expansion center \vec{x}_p is located in.

All of these rules, except the last one, are only general guidelines. Adhering to these guidelines yields satisfactory results. As the numerical experiments show, all parameters can be varied by large amounts while only perturbing the resulting solution. The MMP method is not very sensitive to the actual discretization used.

As shown, the MMP expansion converges faster than the classical multipole or simple boundary element expansions for complex scattering geometries. The method is either able to solve scattering problems involving harmonic sources or to calculate seismograms by Fourier synthesis. For the problem posed, we also found the MMP expansions to be faster than finite difference modeling with approximately the same degree of accuracy. In the example, source, receivers and scatterers were located close to each other. For problems with larger distances between them, we can expect an even greater decrease in computation time compared to finite differences. Furthermore, due to its spectral nature, attenuation can easily be accounted for. Thus, the MMP method is well suited for a large range of scattering problems since both acoustic and elastic media with different boundary conditions (fluid-fluid, elastic-elastic and others) can be treated exactly the same way in this algorithm.

ACKNOWLEDGMENTS

This work was supported by the Air Force Office of Scientific Research under contract no. F49620-93-1-0424DEF. Also, the author was supported by the nCUBE fellowship.

References

- Aki, K. and K. Larner, Surface motion of a layered medium having an irregular interface due to incident plane SH-waves, *Journal of Geophysical Research*, 75, 933–954, 1970.
- Amos, D. , ALGORITHM 644: a portable package for Bessel functions of a complex argument and nonnegative order, *ACM Transactions of Mathematical Software*, 12, 265–273, September 1986.
- Ballisti, R. and C. Hafner, The multiple multipole method in electro- and magnetostatic problems, *IEEE Transactions on Magnetics*, 19, 2367–2370, November 1983.
- Boström, A. , Scattering by a smooth elastic obstacle, *Journal of the Acoustical Society of America*, 67, 1904–1912, June 1980.
- Bouchon, M. and K. Aki, Discrete wavenumber representation of seismic-source wave fields, *Bull. Seis. Soc. Am.*, 67, 259–277, April 1977.
- Brebbia, C. and J. Dominguez (eds.), *Boundary Elements, an introductory course*, McGraw-Hill, New York, 1989.
- Červený, V. , I. Molotkov, and I. Pšenčík, *Ray Methods in Seismology*, University Karbva, Praha, 1977.
- Chin, R. , G. Hedstrom, and L. Thigoen, Matrix methods in synthetic seismograms, *Geophysical Journal of the Royal Astronomical Society*, 77, 483–502, 1984.
- George, A. and M. Heath, Solutions of sparse linear least squares problems using Givens rotations, *Linear Algebra and its Applications*, 34, 69–83, 1980.
- Haartsen, M. , M. Bouchon, and M. Toksöz, A study of seismic acoustic wave propagation through a laterally varying medium using the boundary-integral-equation- discrete wave-number method, *Journal of the Acoustical Society of America*, 96, 3010–3021, November 1994.
- Hafner, C. , *The generalized multipole technique for computational electromagnetics*, Artech House, Inc, Boston, 1990.
- Hafner, C. , On the design of numerical methods, *IEEE Antennas and Propagation Magazine*, 35, 13–21, August 1993.

- Hong, T. and D. Helmberger, Glorified optics and wave propagation in non-planar structure, *Bull. Seis. Soc. Am.*, 68, 2013–2032, 1978.
- Hosken, J. , Ricker wavelets in their various guises, *First Break*, 6, 24–33, January 1988.
- Imhof, M. , Multiple multipole expansions for acoustic scattering, *Journal of the Acoustical Society of America*, 97, 754–763, February 1995.
- Kelly, K. , R. Ward, S. Treitel, and R. Alford, Synthetic seismograms: a finite difference approach, *Geophysics*, 41, 2–27, February 1976.
- Kennett, B. , *Seismic wave propagation in stratified media*, Cambridge University Press, 1983.
- Miles, J. , Scattering of elastic waves by small heterogeneities, *Geophysics*, 25, 642–648, 1960.
- Morse, P. and H. Feshbach, *Methods of Theoretical Physics*, McGraw-Hill, 1953.
- Müller, G. , The reflectivity method: a tutorial, *Journal of Geophysics*, 58, 153–174, 1985.
- Paillet, F. and C. Cheng, *Acoustic waves in boreholes*, CRC Press, Boca Raton, 1991.
- Pao, Y. and C. Mow, *Diffraction of Elastic Waves and Dynamic Stress Concentrations*, The Rand Corporation, New York, 1973.
- Peng, C. and M. Toksöz, An optimal absorbing boundary condition for finite difference modeling of acoustic and elastic wave propagation, *Journal of the Acoustical Society of America*, 95, 733–745, 1994.
- Smith, W. , The application of finite element analysis to body wave propagation problem, *Geophysical Journal of the Royal Astronomical Society*, 42, 747–768, 1974.
- Červený, V. and I. Pšenčík, Gaussian beams in elastic 2-D laterally varying layered structures, *Geophysical Journal of the Royal Astronomical Society*, 78, 65–91, 1984.
- Virieux, J. , P-SV wave propagation in heterogeneous media: velocity stress finite difference method, *Geophysics*, 51, 889–901, 1986.
- Waterman, P. , Matrix theory of elastic wave scattering, *Journal of the Acoustical Society of America*, 60, 567–580, September 1976.
- Wilkinson, J. , *The Algebraic Eigenvalue Problem*, Oxford University Press, 1988.

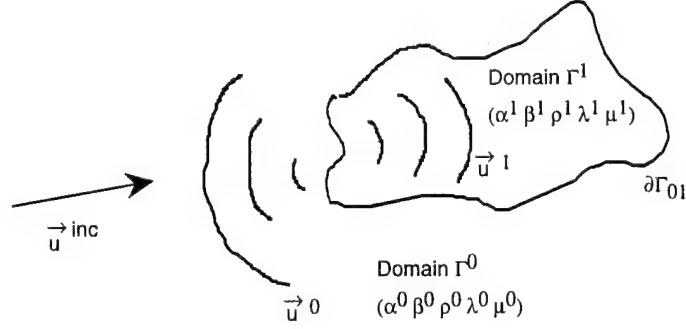


Figure 1: Schematic representation of the scattering experiment. An incident field $\vec{u}^{inc}(\vec{x}, \omega)$ illuminates a bounded two-dimensional inhomogeneity which induces a scattered field $\vec{u}^0(\vec{x}, \omega)$ in the background medium $(\alpha^0, \beta^0, \rho^0)$ as well as a field $\vec{u}^1(\vec{x}, \omega)$ in the scatterer itself $(\alpha^1, \beta^1, \rho^1)$.

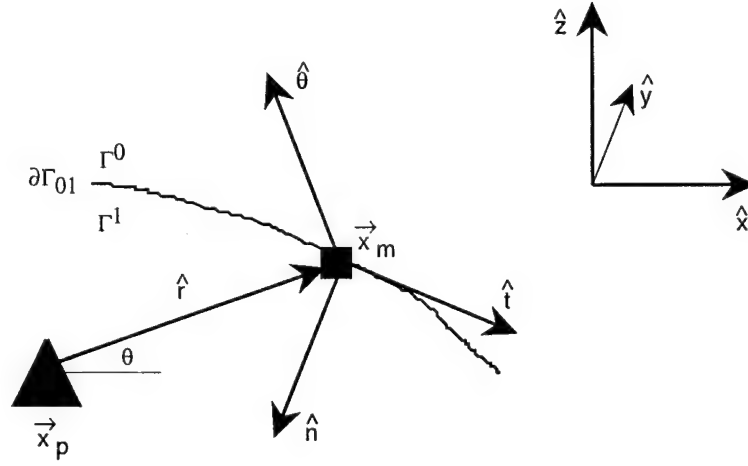
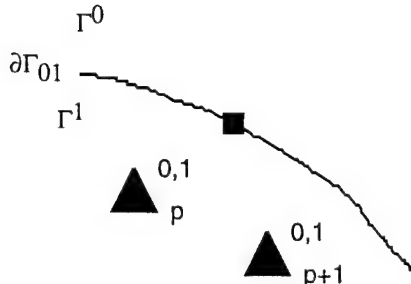
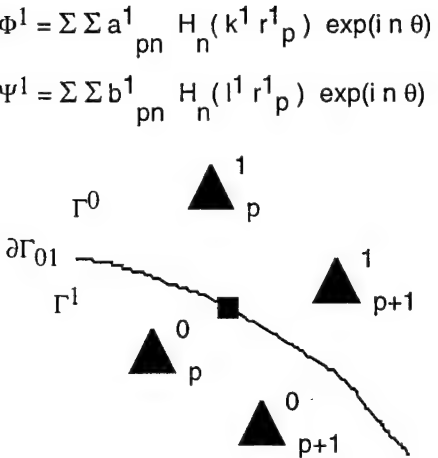


Figure 2: Schematic of the coordinate systems used. Additional to a global cartesian coordinate frame (x, z, y) , local cylindrical systems (r, θ, y) with origins at \vec{x}_p are used. Such a local origin or expansion center is depicted by the triangle. Boundaries between different media are defined by discrete matching points located at \vec{x}_m where normal \hat{n} and tangential \hat{t} directions are specified. The matching points are denoted by squares.



$$\begin{aligned}\Phi^0 &= \sum \sum_{pn} a_{pn}^0 H_n(k^0 r_p^0) \exp(in\theta) \\ \Psi^0 &= \sum \sum_{pn} b_{pn}^0 H_n(l^0 r_p^0) \exp(in\theta) \\ \Phi^1 &= \sum \sum_{pn} a_{pn}^1 J_n(k^1 r_p^1) \exp(in\theta) \\ \Psi^1 &= \sum \sum_{pn} b_{pn}^1 J_n(l^1 r_p^1) \exp(in\theta)\end{aligned}$$



$$\begin{aligned}\Phi^1 &= \sum \sum_{pn} a_{pn}^1 H_n(k^1 r_p^1) \exp(in\theta) \\ \Psi^1 &= \sum \sum_{pn} b_{pn}^1 H_n(l^1 r_p^1) \exp(in\theta) \\ \Phi^0 &= \sum \sum_{pn} a_{pn}^0 H_n(k^0 r_p^0) \exp(in\theta) \\ \Psi^0 &= \sum \sum_{pn} b_{pn}^0 H_n(l^0 r_p^0) \exp(in\theta)\end{aligned}$$

Figure 3: Basis functions can either contain Hankel functions H_n or Bessel functions J_n . If the same expansion center is to be used for ϕ_p^0 as for ϕ_p^1 , then the inside field has to be expanded using the Bessel functions J_n since they represent standing waves. If the inside and the outside scattered field are to be represented by Hankel functions H_n , different expansion centers have to be used. Expansion centers are depicted by a triangle while squares are used for matching points.

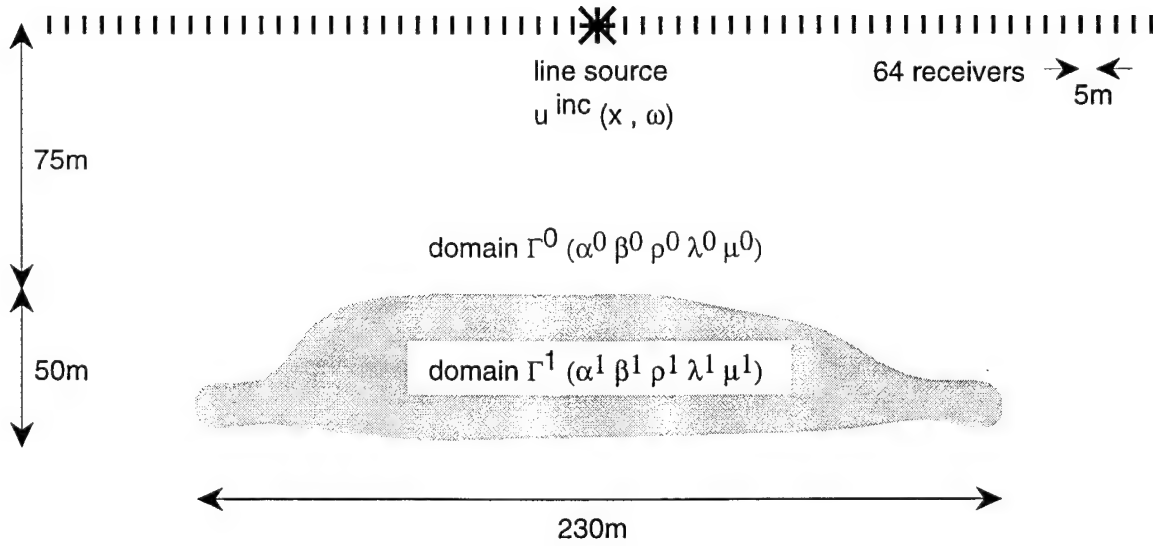


Figure 4: Generic scatterer used for numerical experiments. The scatterer is illuminated by an explosive line source modulated by a Ricker wavelet of 50Hz center frequency. The velocities in the background domain Γ^0 are $\alpha^0 = 2000\text{m/s}$ and $\beta^0 = 1155\text{m/s}$. The velocities in the scatterer Γ^1 are $\alpha^1 = 3000\text{m/s}$ and $\beta^1 = 1732\text{m/s}$. The Poisson's ratio is the same for both regions ($\sigma = 0.25$). For simplicity, the density is kept constant at $\rho = 2000\text{kg/m}^3$.

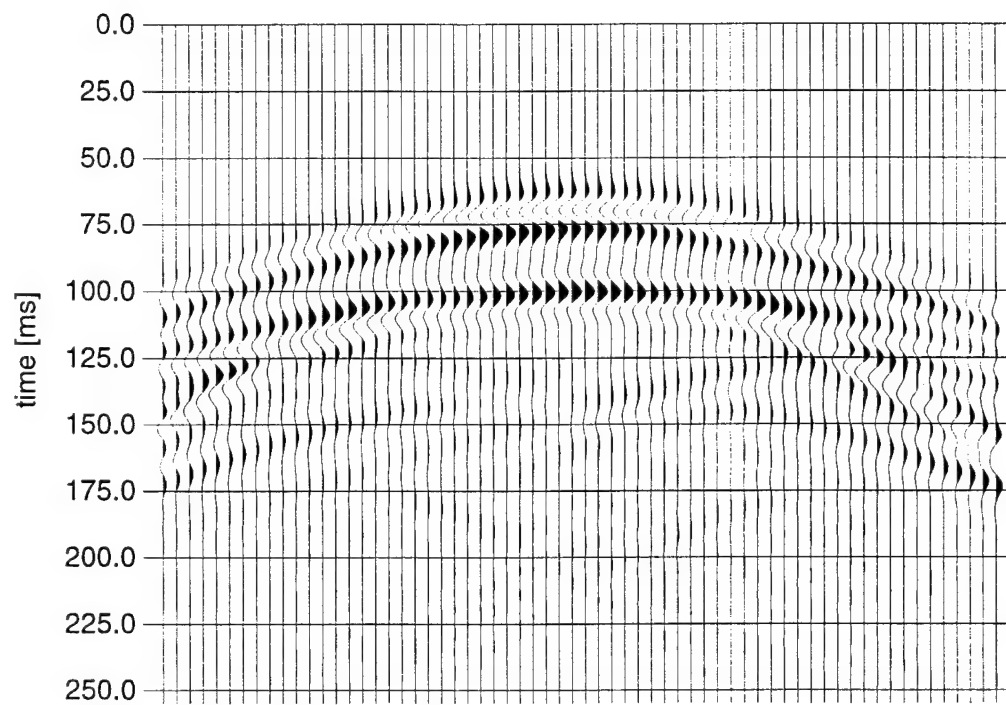


Figure 5: The seismogram of the model shown in Figure 4 calculated using a finite difference method. This seismogram is used as a reference to compare the ones calculated with different MMP expansions against.

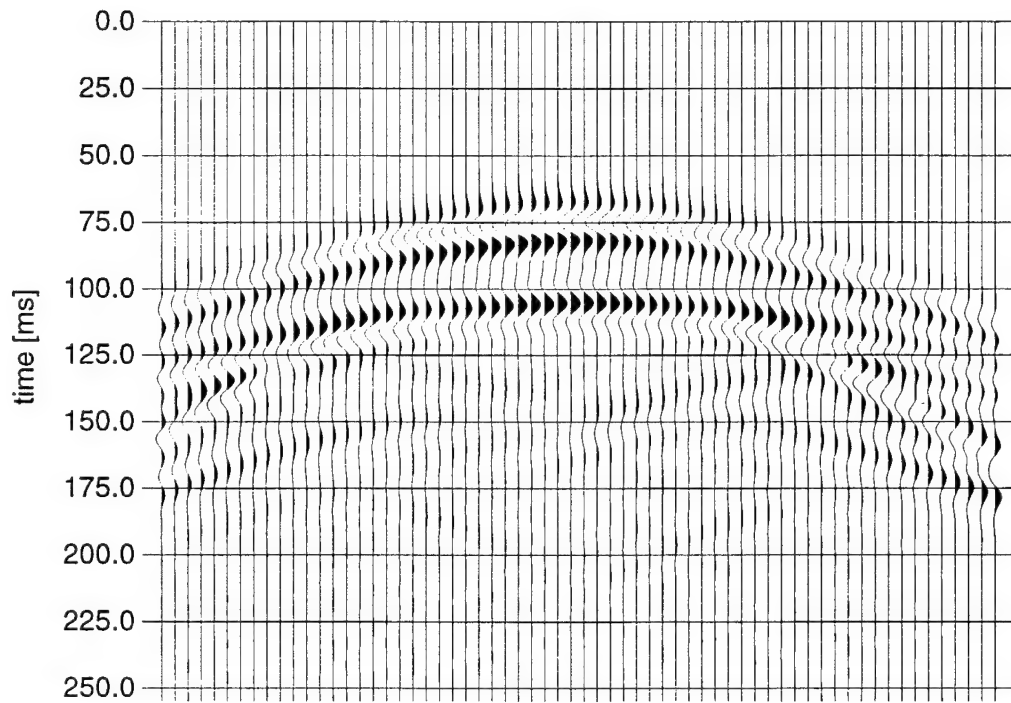


Figure 6: The seismogram of the model shown in Figure 4 calculated using the MMP algorithm. Altogether, 256 expansion functions, 8 expansion centers, 128 matching points and 64 frequencies were used. As can be seen, the MMP solution agrees very well with the finite difference reference seismogram shown in Figure 5.

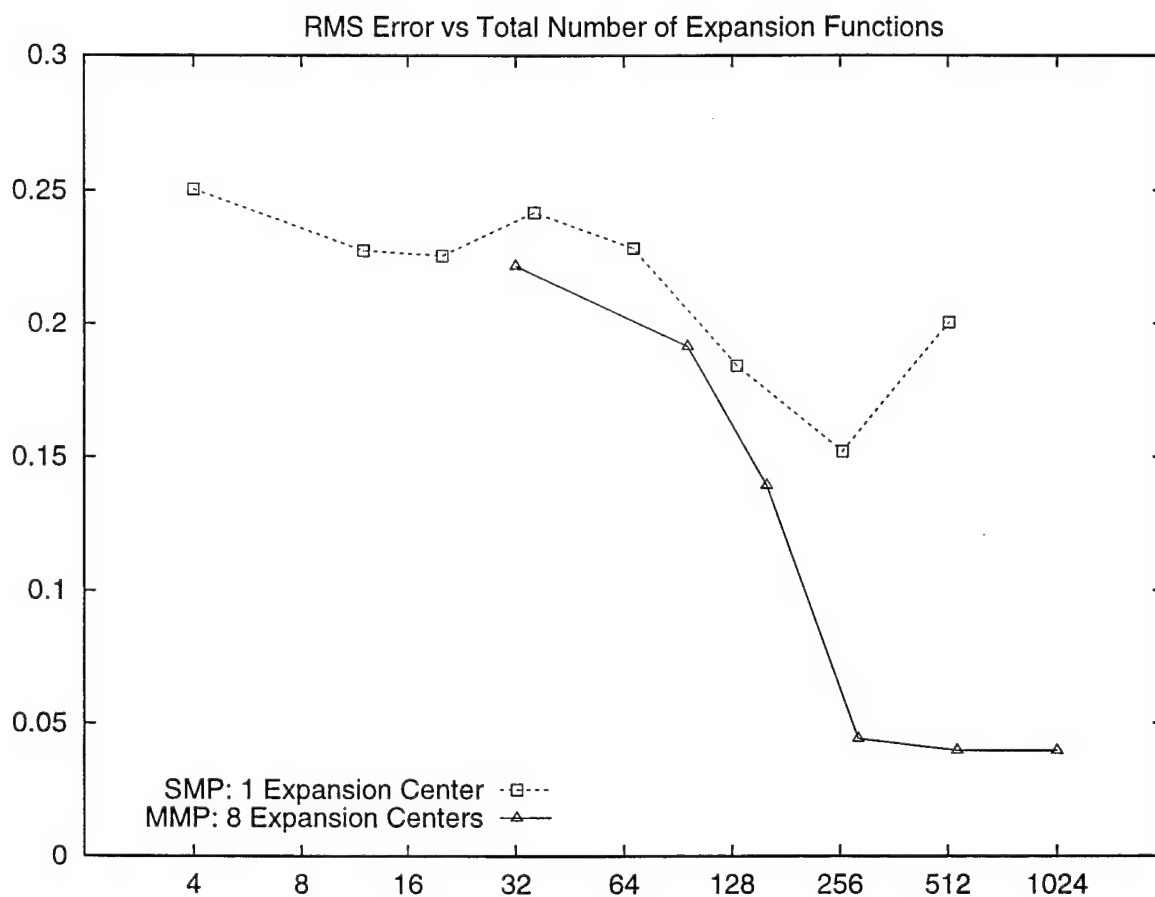


Figure 7: Comparison between the traditional eigenfunction expansion SMP (dashed) and the MMP expansion (solid). Shown is how the total number of expansion functions affects the RMS error compared to the FD reference. The SMP actually never converges since for 512 expansion functions it violates the sampling condition. For 256 and more expansion functions, the MMP expansion converge.

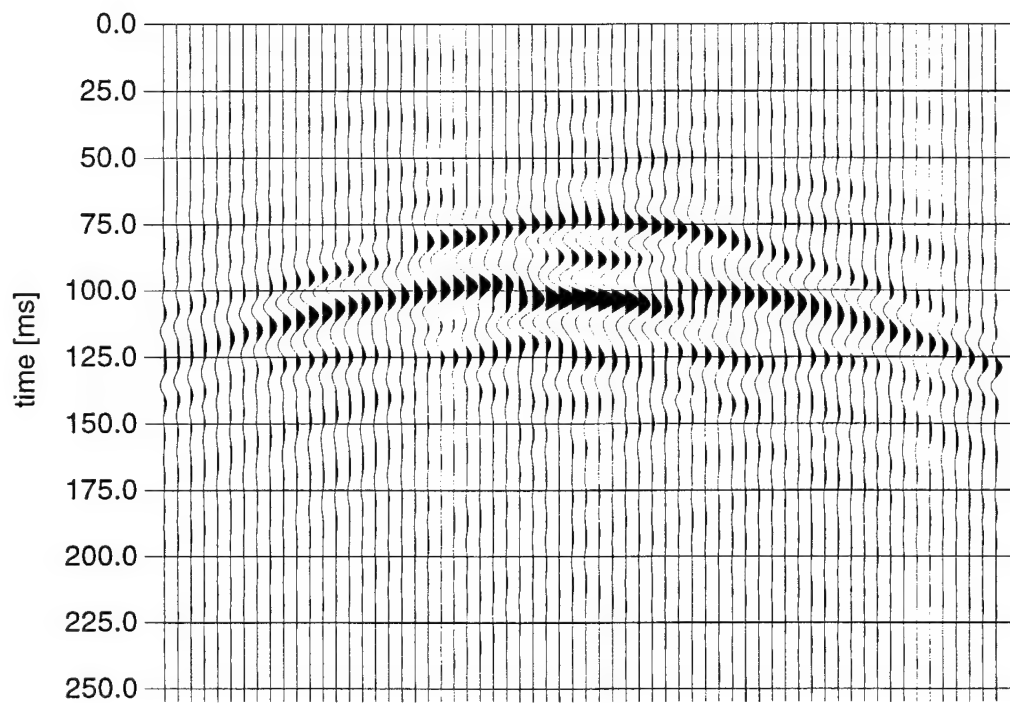


Figure 8: The seismogram for the case when 64 expansion functions are used. The seismogram is very noisy. Some of the prominent features in Figure 5 begin to show up, but the expansions have not converged yet. More terms have to be used to obtain convergence.

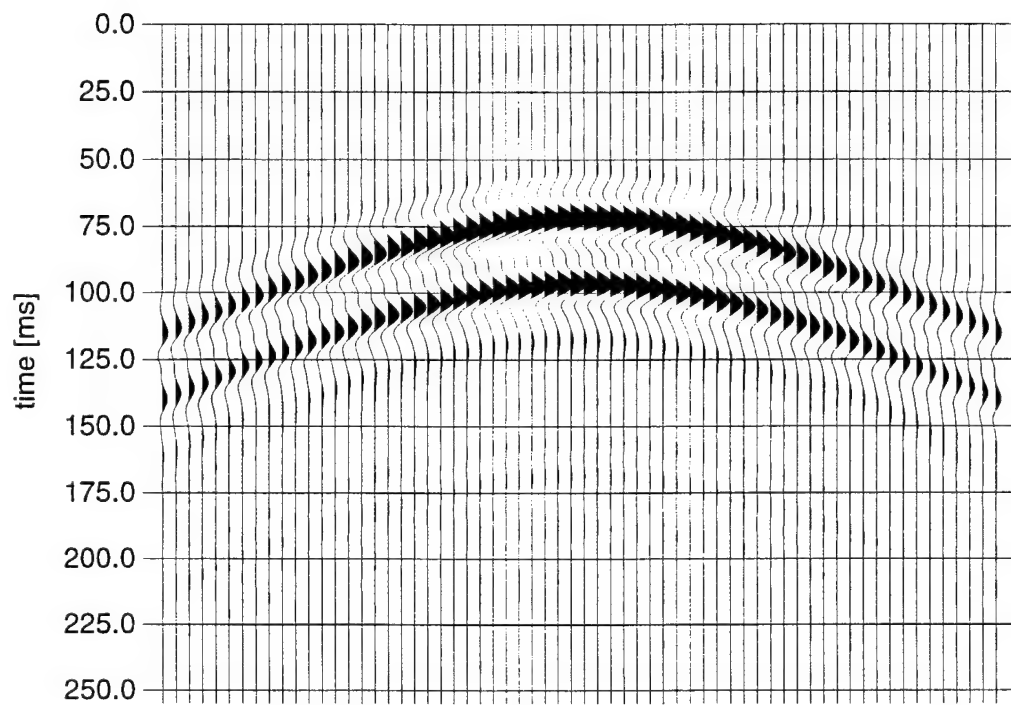


Figure 9: The seismogram for the case when only 4 expansion functions are used. Clearly, no self-interaction of the scattered wavefields is possible. Unfortunately, the seismogram is clean enough to be mistaken as correct.

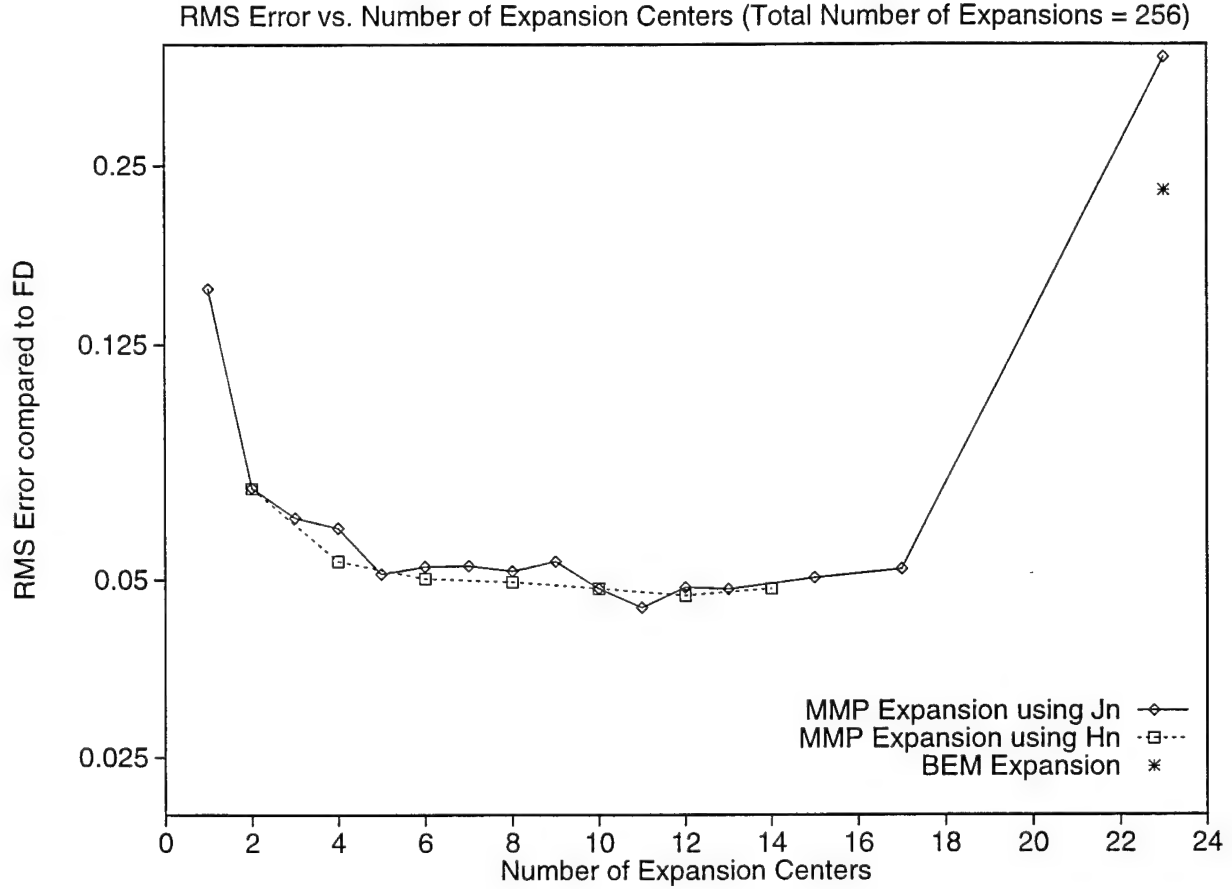


Figure 10: The effect of number and location of the expansion centers. The total number of expansion functions is kept constant at 256 while the number of expansion centers is varied from 1 up to 23. Expansions using the same expansion centers $\tilde{x}_p^d \in \Gamma^1$ for $\phi^0, \psi^0, \phi^1, \psi^1$ and thus Bessel functions J_n as well as expansions using expansion centers $\tilde{x}_p^0 \in \Gamma^1$ for ϕ^0, ψ^0 and $\tilde{x}_p^1 \in \Gamma^0$ for ϕ^1, ψ^1 and thus Hankel functions H_n are tested. The difference between these two kinds of expansions is rather small. Placing all expansion centers onto the boundary and using only the 0th order terms which corresponds to a simple boundary element expansions fails surprisingly.

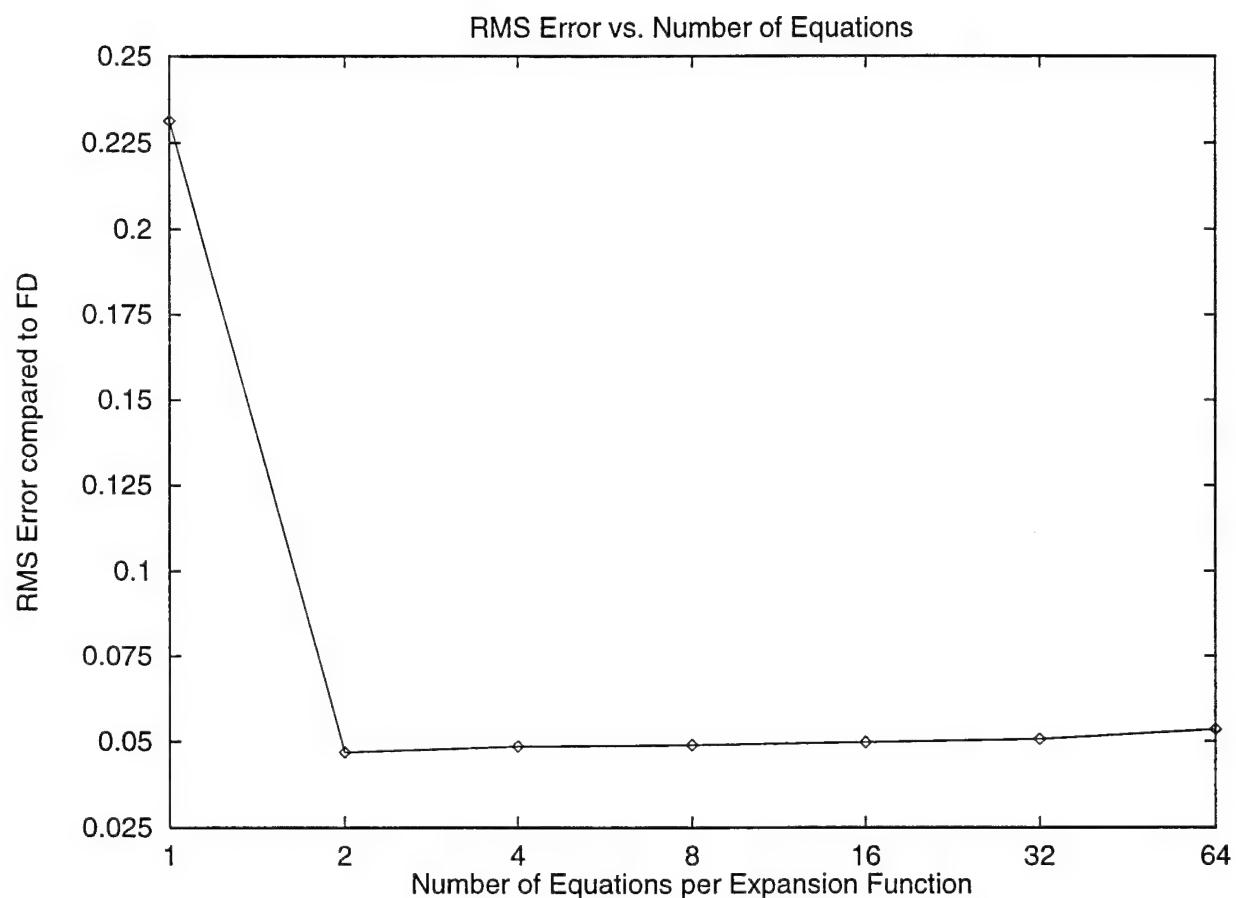


Figure 11: Influence of the number of matching points on an expansion with 256 expansion functions and 8 centers of expansion. Each matching point provides 4 equations. Since the expansion is non-orthogonal, using as many equations as unknowns to be resolved does not yield a correct result. Adding more and more equations to the system increases the condition number and thus the RMS error is increased due to numerical errors.

RELOCATION OF EXPLOSIONS AT THE BALAPAN, KAZAKHSTAN TEST SITE

Yingping Li, William Rodi, and M. Nafi Toksöz Earth Resources Laboratory
Department of Earth, Atmospheric, and Planetary Sciences
Massachusetts Institute of Technology
Cambridge, MA 02142-1324

SUMMARY

We apply a technique for relative event location with differential arrival times to relocate four presumed nuclear explosions occurring at the Balapan, Kazakhstan test site during 1987. Waveform cross-correlation analysis was performed on seismograms from ten far-regional and teleseismic stations to determine differential arrival times for P waves and some PcP waves relative to the Joint Verification Event of 14 September 1988. The resulting differential arrival time data were used to determine the epicenters of the four events relative to the epicenter of the JVE event. We compare our locations to highly precise epicenters determined from satellite images, and to teleseismic locations obtained with the conventional location method applied to hundreds of absolute arrival time picks. Our locations differ from the satellite locations by 2 to 3 kilometers and are more accurate than the locations obtained from hundreds of data.

INTRODUCTION

The ability to accurately locate seismic events is of crucial importance for seismic identification and discrimination. We have developed a high precision relative event location method based on seismic waveform cross-correlation analysis. Previously, we reported the application of this method to quarry blasts in Estonia using near regional data from the Scandinavian arrays FINESA, NORESS and ARCESS (Toksöz *et al.*, 1993; Rodi *et al.*, 1994). The results of this study showed a significant improvement in location accuracy compared to routine locations done by the Intelligent Monitoring System, with relative epicenters between events estimated

to have accuracies of approximately one kilometer. In the present report, we extend our method to locate nuclear explosions in the Balapan, Kazakhstan test site (KTS) using far-regional and teleseismic waveform data.

During the years 1965 through 1989, 101 presumed nuclear explosions from the Balapan, Kazakhstan Test Site (KTS) were detected and located teleseismically (e.g., Marshall *et al.*, 1984; Ringdal *et al.*, 1992). There have been a number of teleseismic location studies of Balapan events using the joint epicenter determination (JED) method of Douglas (1967). Marshall *et al.* (1984) located 61 Balapan explosions through 1982, using the location of event 650115, which is determined by LANDSAT satellite imaging, as a master event. Lilwall and Farthing (1990) relocated presumed nuclear explosions from 1973 to 1989 using seven master events. Furthermore, Thurber *et al.* (1994) used 27 master events to constrain the teleseismic locations with both JED and a master event location algorithm. The locations of an additional 20 master events were determined by analyzing a SPOT satellite image (Thurber *et al.*, 1993). The locations of these presumed nuclear explosions have also been routinely determined by ISC and NEIC. The ISC and NEIC generally used several hundred arrival time data recorded by all available stations around the world to determine the epicenters. However, none of these previous location studies have utilized the seismic waveforms recorded from the events.

Using both SPOT and LANDSAT satellite images, Thurber *et al.* (1993, 1994) determined the locations of 101 presumed explosions at KTS with 100 m to 200 m precision. These studies found that the teleseismic locations (JED) of most events agreed with the LANDSAT/ SPOT shot points to within about 1 to 2 km. The high precision locations based on satellite images also provide a ground truth database for testing our relative location method. In this report, we apply our method to seismic waveform data from five nuclear explosions recorded at ten stations, with epicentral distances from 23 to 67 degrees.

DATA PROCESSING

Figure 1 is a world map showing locations of five presumed nuclear explosions (circles) at Balapan, KTS, and ten seismic stations (triangles) used in this study. All stations have vertical short-period seismic instruments and a few of them also were equipped with three-component broadband sensors. The sampling rate is from 20 to 40 samples per second. Figure 2 shows the locations of the five presumed explosions, as determined by satellite imaging (Thurber *et al.*, 1993) and the PDE using teleseismic arrival time data (NEIC/USGS, 1987, 1988). The hypocentral parameters of the events are also listed in Table 1. In order to examine the relative locations among the events, we use the satellite image location of event 94, the JVE (Joint

Table 1: Hypocentral Parameters of Five Presumed Underground Nuclear Explosions at the Balapan Test Site

<i>Event</i>	<i>YrMoDa</i>	<i>HrMinSec</i>	<i>Latitude</i>	<i>Longitude</i>	<i>m_b</i>
		(a)	(b)	(b)	(c)
85	870620	005304.8	49.9367	78.7464	6.0
86	870802	005806.8	49.8806	78.8750	5.8
88	871213	032104.9	49.9614	78.7933	6.1
89	871227	030504.8	49.8789	78.7253	6.0
94	880914	035957.4	49.8781	78.8239	6.0

Notes: (a) Origin time is from NEIC/USGS. (b) Latitude and longitude are from Thurber *et al.* (1993). (c) m_b is from Ringdal *et al.* (1992),

Verification Experiment) event, as a common reference point. In Figure 2, the locations of the other four events are plotted relative to this reference point. We can see from the figure that location differences between the satellite image and PDE locations vary from 2 to 10 km. We will use our waveform correlation/relative event location algorithm to examine what relative location accuracy can be achieved with waveforms from only ten stations. The stations are listed in Table 2, together with their distances and azimuths from the JVE event.

Figure 3 shows the seismograms of the JVE event ($m_b=6.0$) recorded at the ten stations shown in Figure 1. We took the JVE event to be a master event, and determined differential arrival times between it and the other four events. Figure 4 shows vertical seismograms of the five study events recorded at station LZH, with an epicentral distance of 23 degrees and an azimuth of 118 degrees. We note that the P waveforms for the first few seconds are very similar to one another, implying these events do not have significant hypocentral separation. Since the epicentral distance from station LZH to the test site is at a far-regional distance, the P waveforms are more complex than those recorded at teleseismic distance. This can be seen in Figure 5, which shows vertical component seismograms of the five events recorded at station COL, at an epicentral distance of 60 degrees and an azimuth of 21 degrees. In contrast to Figure 4, the P waveforms recorded at station COL are relatively simple. Like LZH, the waveforms of the five events are similar to one another. For some events, we can also clearly identify the PcP arrival.

To accurately measure the differential arrival times we used a waveform cross-correlation technique. Cross-correlation analysis either in the frequency domain (e.g., Poupinet *et al.*,

Table 2: Distances and Azimuths From JVE Event to Stations

<i>Station</i>	<i>Distance</i> (deg)	<i>Azimuth (deg.</i> <i>c.w. from N)</i>
ANTO	33.5	-89.4
BJI	27.9	96.2
COL	59.7	20.9
GBAR	36.3	-177.7
GRFO	42.1	-63.1
HIA	26.2	75.4
KMI	30.9	134.4
KONO	39.2	-48.4
LZH	22.7	117.8
YKAR	67.1	6.6

1984, Ito, 1985; Fremont and Malone, 1987; Moriya *et al.*, 1994) or in the time domain (e.g., Frankel, 1982; Pechmann and Kanamori, 1982; Phillips *et al.*, 1992; Deichmann and Garcia-Fernandez, 1992; Rodi *et al.*, 1993; Li *et al.*, 1995) have been developed to quantitatively characterize the degree of similarity of seismic waveforms from a cluster of earthquakes close in space and to measure their differential arrival times in an accurate, objective, and consistent manner. The conventional time domain analysis typically enables arrivals times to be read, at best, to an accuracy of one sample interval, while the cross-spectral method (Poupinet *et al.*, 1984, Ito, 1985, 1990) and interpolation techniques in the time domain (Deichmann and Garcia-Fernandez, 1992; Li *et al.*, 1995) can improve the timing precision to between 0.1 and 0.5 sampling intervals. For our data set used here, the accuracy of differential arrival time measurements typically ranges from 0.01 to 0.02 seconds.

Figure 6 is an example of the waveform cross-correlation analysis procedure. The top frame of Figure 6 shows three vertical P waveforms of three Balapan explosions recorded at station BJI. The epicentral distance and azimuth are 28 and 96 degrees, respectively. The waveforms are aligned by the origin times published by the NEIC/USGS (1987, 1988). We used the JVE explosion (event 94) as a master event and explosions 85 and 86 (Table 1) as slave events. The cross-correlation function between a master and a slave event was calculated for a P wave window to measure the differential arrival time between events, as inferred from the time lag between the maximum peaks of the auto- and cross-correlation functions. The P wave window length used here is 6 s. The bottom frame of Figure 6 shows the cross-correlation functions for

events 85 and 86, as well as the auto-correlation function for event 94. The peak correlation values are 0.95 and 0.9 for events 85 and 86, respectively, suggesting that the slave events (85, 86) are indeed located very close to the master event 94. The differential arrival times relative to event 94 are 0.475 and -0.245 s for events 85 and 86, respectively.

Figure 7 shows the analogous waveform correlation results for station ANTO, which has an epicentral distance of 34 degrees and an azimuthal of 271 degrees from the test site. The top frame of Figure 7 shows the vertical component P waveforms for events 85, 86 and 94, while the cross-correlation and auto-correlation functions are depicted in the bottom frame of Figure 7. The P wave window length used here is 6 s. The cross-correlation coefficients are again very high, 0.92 to 0.94, and differential P wave arrival times are measured to be about -0.475 and 0.36 s for events 85 and 86, respectively, relative to event 94.

We also calculated the cross-correlation functions for PcP waves at some stations. Three vertical component seismograms showing both P and PcP waves recorded at station ANTO (distance = 34 degrees, azimuth = 271 degrees) are shown on the top frame of Figure 8. Using a 6 second window around the PcP wave, we calculated the cross-correlation functions for events 85 and 86 and the auto-correlation function for event 94 (bottom frame of Figure 8). The cross-correlation coefficients are 0.8 and 0.72 for events 85 and 86, respectively. Using event 94 as a reference, the PcP differential arrival times are measured to be -0.175 s and 0.165 s for events 85 and 86, respectively.

Table 3 lists all the differential times that were determined together with their estimated accuracies (σ). Figure 9 summarizes the results of the waveform correlation analysis (Figures 6 to 8). The top and middle frames of Figure 9 are results for P waves. Two stations BJI and ANTO have a similar epicentral distance, but with an azimuth difference of about 174 degrees they are in opposite directions from the events. For event 85, the P wave differential time is 0.475 s at station BJI and -0.475 s at station ANTO, indicating the event is closer than the master (94) to station ANTO and farther away from station BJI. This observation agrees with the determination by Thurber *et al.* (1993), based on satellite imaging, that event 85 is located about 5 km west of event 94 (Figure 2). In contrast, for event 86, the P wave differential time is -0.245 s at station BJI and 0.36 s at station ANTO, indicating that this event is east of event 94, which is also consistent with Thurber *et al.* (1993).

Table 3: Differential Arrival Times Relative to JVE Event

<i>Station</i>	<i>Phase</i>	<i>Slave Event</i>	<i>Time (s)</i>	<i>σ (s)</i>
ANTO	P	85	-0.475	0.025
ANTO	PcP	85	-0.175	0.03
ANTO	P	86	0.360	0.01
ANTO	PcP	86	0.165	0.015
BJI	P	85	0.475	0.01
BJI	P	86	-0.245	0.01
BJI	P	88	0.290	0.01
BJI	P	89	0.765	0.015
COL	P	85	-0.365	0.015
COL	PcP	85	-0.360	0.01
COL	P	86	-0.250	0.01
COL	PcP	86	-0.215	0.015
COL	P	88	-0.565	0.015
COL	PcP	88	-0.520	0.02
GBAR	P	85	0.660	0.01
GBAR	PcP	85	0.340	0.01
GBAR	P	86	0.315	0.015
GBAR	PcP	86	0.315	0.015
GBAR	P	88	1.000	0.015
GBAR	PcP	88	0.480	0.02
GBAR	P	89	0.120	0.02
GBAR	PcP	89	0.060	0.01
GRFO	P	85	-0.680	0.02
GRFO	P	86	0.330	0.02
GRFO	P	88	-0.410	0.01
GRFO	P	89	-0.345	0.01
HIA	P	85	0.262	0.02
HIA	PcP	85	0.075	0.01
HIA	P	86	-0.275	0.015
HIA	PcP	86	-0.050	0.01
HIA	P	88	0.063	0.015
HIA	PcP	88	0.060	0.01
HIA	P	89	0.775	0.015
HIA	PcP	89	0.350	0.01
KMI	P	85	0.600	0.01
KMI	P	86	-0.112	0.015
KMI	P	88	0.690	0.01
KMI	P	89	0.425	0.05
KONO	P	85	-0.770	0.02
KONO	P	86	0.270	0.02
KONO	P	88	-0.515	0.015
LZH	P	85	0.685	0.015
LZH	P	86	-0.260	0.01
LZH	P	88	0.650	0.01
LZH	P	89	0.715	0.01
YKAR	P	89	0.360	0.01
YKAR	PcP	89	0.285	0.015

Table 4: Locations of Five Presumed Underground Nuclear Explosions Determined from Differential Arrival Times

<i>Event</i>	<i>Latitude</i>	<i>Longitude</i>	<i>North (km)</i>	<i>East (km)</i>
85	49.9574	78.7591	8.8	-4.6
86	49.9050	78.8874	3.0	4.5
88	49.9786	78.8052	11.2	-1.3
89	49.8601	78.7117	-2.0	-8.0
94	49.8781	78.8239	0.0	0.0

Table 5: 90% Confidence Ellipses on Locations Relative to Event 94

<i>Event</i>	<i>Strike (deg c.w. from N)</i>	<i>Semi-major axis (km)</i>	<i>Semi-minor axis (km)</i>
85	42	1.3	1.1
86	18	1.4	0.9
88	31	1.6	0.9
89	30	1.7	1.0

RELOCATION RESULTS AND CONCLUSIONS

We applied our multiple event location algorithm (Rodi *et al.*, 1994) to the differential arrival time data listed in Table 3. The epicenters and origin times of the four slave events (85, 86, 88, 89) were fit to the data in a weighted least squares sense. The epicenter and origin time of event 94 were fixed to the values given in Table 1 (Thurber *et al.*, 1993; NEIC/USGS, 19987, 1988). The depths of all events were constrained to the earth's surface. The forward model for traveltimes was computed from the IASP91 tables, retrieved from the Center for Monitoring Research in Arlington, Virginia. Our relocated epicenters are listed in Table 4 and plotted in Figure 10.

The final residuals of fit to the differential arrival time data averaged 5.4 standard deviations. Allowing for degrees of freedom, this implies posterior estimates of the data standard deviations equal to 6.2 times the assumed (prior) standard deviations shown in Table 3. We attribute the large residuals to two major causes. First, the events were fixed to a common depth while the true depths of the events vary. Second, the IASP91 traveltime tables do not reflect the relatively lower velocity layers at shallower depths at the KTS site (Priestley *et al.*, 1988; Li

and Thurber, 1991; Quin and Thurber, 1992); nor do they reflect lateral velocity variations at the site.

Figure 10 compares our locations (stars) with the NEIC/USGS locations (octagons) and satellite locations of Thurber *et al.* (1993) (squares). The USGS locations have been shifted so as to align event 94 with its satellite location. Our location for event 94 coincides with the satellite location as a constraint. We see that our locations for the remaining four events are within 2 to 3 km of the satellite locations of Thurber *et al.* (1993). Our location for event 85 is comparable to the NEIC location for this event, but for the other three events (86, 88 and 89) our locations are better than the NEIC locations, with mislocations reduced by factors of about 2 to 5. We also note that if we had used more accurate traveltime tables, allowing for slower shallow velocities, our pattern of locations would shrink and its agreement with the satellite image locations would improve slightly. In Table 5 we list the formal confidence ellipses for the location of each slave event relative to the location of the JVE event (94). (These error estimates include the posterior variance factor.) We see that the 90% confidence ellipses have semi-axes of about 1 and 1.5 km, which is about half of the actual location errors.

We conclude from these results that a relative event location method applied to differential P and PcP arrival times at a small number of far-regional and teleseismic stations yields relative location accuracies for explosions as good as, or better, than conventional locations obtained with hundreds of arrival time picks from a large network of globally distributed stations. The reason for this is that the waveforms of explosions differing in location by only several kilometers are very similar, allowing the measurement of highly accurate arrival time differences between events using cross-correlation techniques. Therefore, waveform analysis and relative event location methods can be valuable assets for nuclear monitoring and discrimination.

REFERENCES

- Deichmann, N. and M. Garcia-Fernandez, 1992. Rupture geometry from high-precise relative hypocenter locations of microearthquake clusters, *Geophys. J. Int.*, **110**, 501-517.
- Douglas, A., 1967. Joint epicentre determination, *Nature*, **215**, 47-48.
- Frankel, A., 1982. Precursors to a magnitude 4.8 earthquake in the Virgin Islands: spatial clustering of small earthquakes, anomalous focal mechanisms and earthquakes doublets, *Bull. Seism. Soc. Am.*, **72**, 1277-1294.
- Fremont, M.J. and S.D. Malone, 1987. High precision relative locations of earthquakes at Mount St. Helens, Washington, *J. Geophys. Res.*, **92**, 10223-1023.
- Ito, A., 1985. High resolution relative hypocenters of similar earthquakes by cross-spectral analysis method, *J. Phys. Earth*, **33**, 279-294.
- Ito, A., 1990. Earthquake swarm activity revealed from high-resolution relative hypocenters - clustering of microearthquakes, *Tectonophysics*, **175**, 47-66.
- Li, Y., and C. Thurber, 1991. Hypocenter constraint with regional seismic data: a theoretical analysis for the Natural Resources Defense Council Network in Kazakhstan, USSR, *J. Geophys. Res.*, **96**, 10159-10176.
- Li, Y., C. Doll and M.N. Toksöz, 1995. Source characterization and fault plane determinations for $M_{blg} = 1.2$ to 4.4 earthquakes in the Charlevoix Seismic Zone, Quebec, Canada, submitted to *Bull. Seism. Soc. Am.*
- Lilwall, R.C., and J. Farthing, 1990. Joint epicentre determination of Soviet underground nuclear explosions at the Semipalatinsk test site, Atomic Weapons Research Establishment, *Technical Report O 12/90*.
- Marshall, P.D., T.C. Bache and R.C. Lilwall, 1984. Body wave magnitudes and locations of Soviet underground nuclear explosions at the Semipalatinsk test site, Atomic Weapons Research Establishment, *Technical Report O 16/84*.
- Moriya, H., K. Nagano and H. Niitsuma, 1993. Precise source location of AE doublets by spectral matrix analysis of triaxial hodogram, *Geophysics*, **59**, 36-45.
- NEIC/USGS, 1987. Preliminary Determination of Epicenters.
- NEIC/USGS, 1988. Preliminary Determination of Epicenters.
- Pechmann, J.C. and H. Kanamori, 1982. Waveforms and spectra of preshocks and aftershocks of the 1979 Imperial Valley, California, earthquake: Evidence of fault heterogeneity? *J. Geophys. Res.*, **87**, 10579-10597.
- Phillips, W.S., L.S. House and M.C. Fehler, 1992. V_p/V_s and the structure of microearthquake clusters, *Seismol. Res. Lett.*, **63**, 56-57.

- Poupinet, G., W. L. Ellsworth and J. Frechet, 1984. Monitoring velocity variations in the crust using earthquake doublets: An application to the Calaverza fault, California, *J. Geophys. Res.*, *89*, 5719-5731.
- Priestley, K.F., G. Zandt and G.E. Randall, 1988. Crustal structure in eastern Kazakh, USSR, from teleseismic receiver functions, *Geophys. Res. Lett.*, *15*, 613-616.
- Quin, H.R., and C.H. Thurber, 1992. Seismic velocity structure and event relocation in Kazakhstan from secondary P phases, *Bull. Seism. Soc. Am.*, *82*, 2494-2510.
- Ringdal, F., P.D. Marshall and R.W. Alewine, 1992. Seismic yield determinations of Soviet underground nuclear explosions, *Geophys. J. Int.*, *109*, 65-67.
- Rodi, W., Y. Li and M.N. Toksöz, 1994. Research on monitoring at regional distances: multiple event location, Earth Resources Laboratory, Massachusetts Institute of Technology, *Final Technical Report* to Advanced Research Projects Agency.
- Rodi, W., Y. Li, and C.H. Cheng, 1993. Location of microearthquakes induced by hydraulic fracturing, *Annual Report*, Borehole Acoustic Logging Consortium, MIT, Cambridge, Massachusetts, 369-410.
- Thurber, C.H., H.R. Quin and P.G. Richards, 1993. Accurate locations of explosions in Balapan, Kazakhstan, 1987 to 1989, *Geophys. Res. Lett.*, *20*, 399-402.
- Thurber, C.H., H.R. Quin, and R. Saleh, 1994. Catalog of locations of nuclear explosions at Balapan, Kazakhstan, 1965 to 1985, *Bull. Seism. Soc. Am.*, *84*, 458-461.
- Toksöz, M.N., Y. Li and W. Rodi, 1993. Seismic source characterization with empirical green's function and relative location techniques, in J. F. Lewkowitz and J. M. McPhetres (eds.) *Proceedings of the 15th Annual Seismic Research Symposium*, Vail, Colorado, Air Force Phillips Laboratory, 398-404.

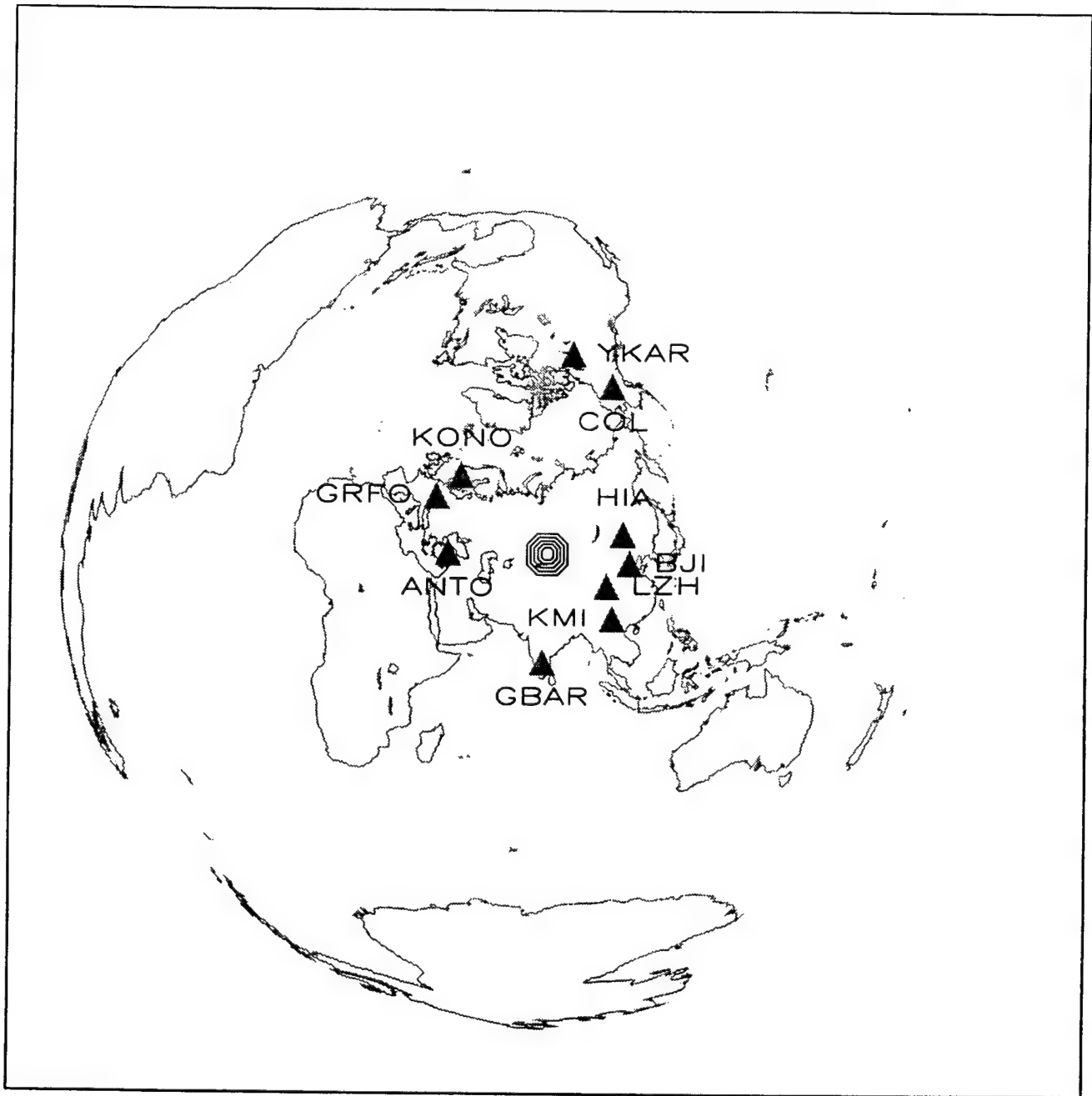


Figure 1: World map showing the locations of five presumed nuclear explosions (octagons) in Balapan, Kazakhstan test site (KTS) and ten seismic stations (triangles) with epicentral distances ranging from 23 to 67 degrees.

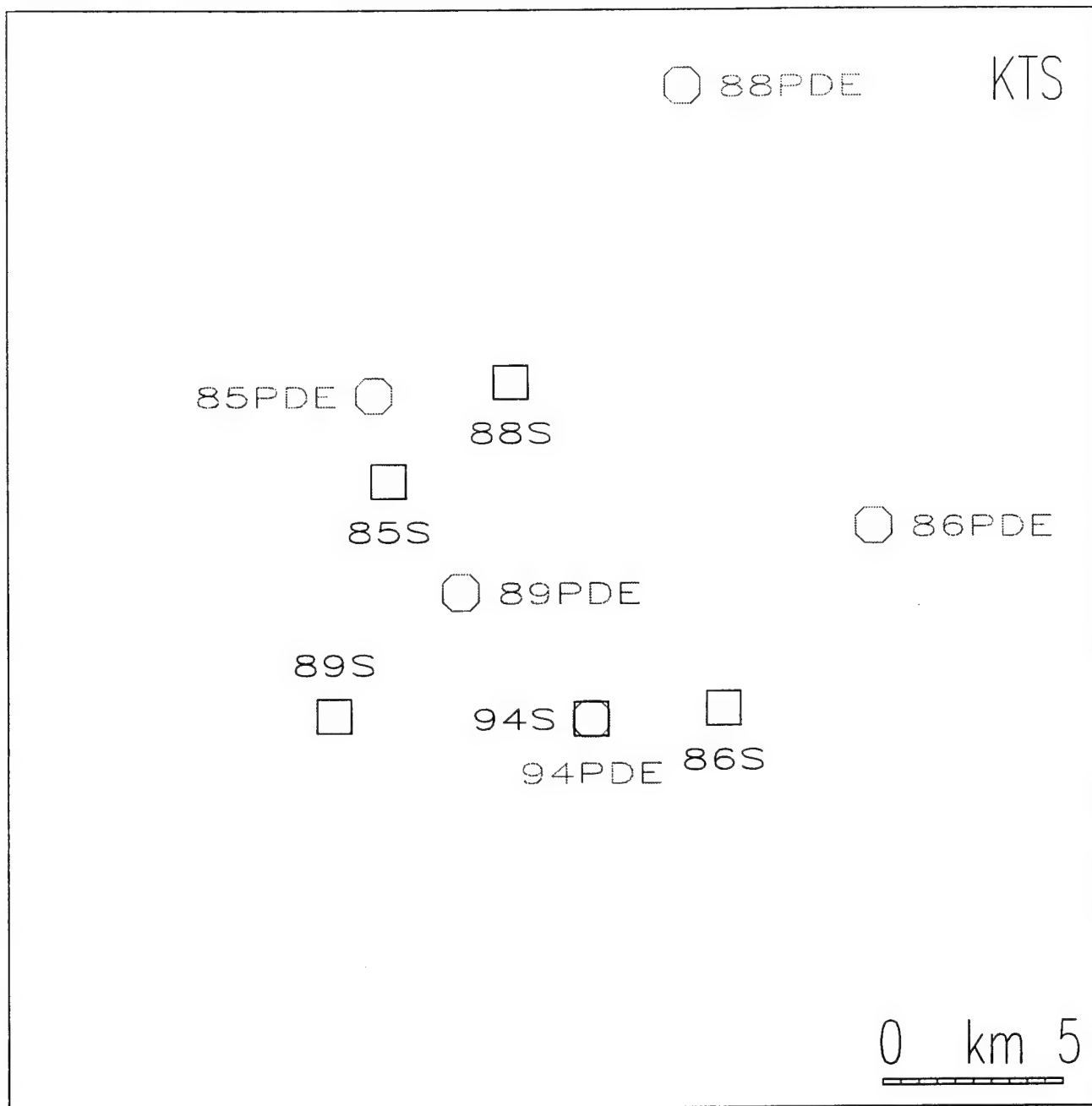


Figure 2: Map of Kazakhstan test site (KTS) showing relative locations of five presumed nuclear explosions determined by Thurber, Quin and Richards (1993) using a satellite imaging technique (squares), and by the USGS with hundreds of arrival time picks (octagons).

Balapan Explosion 94 (880914-03:59:57.4) Recorded at 10 Stations

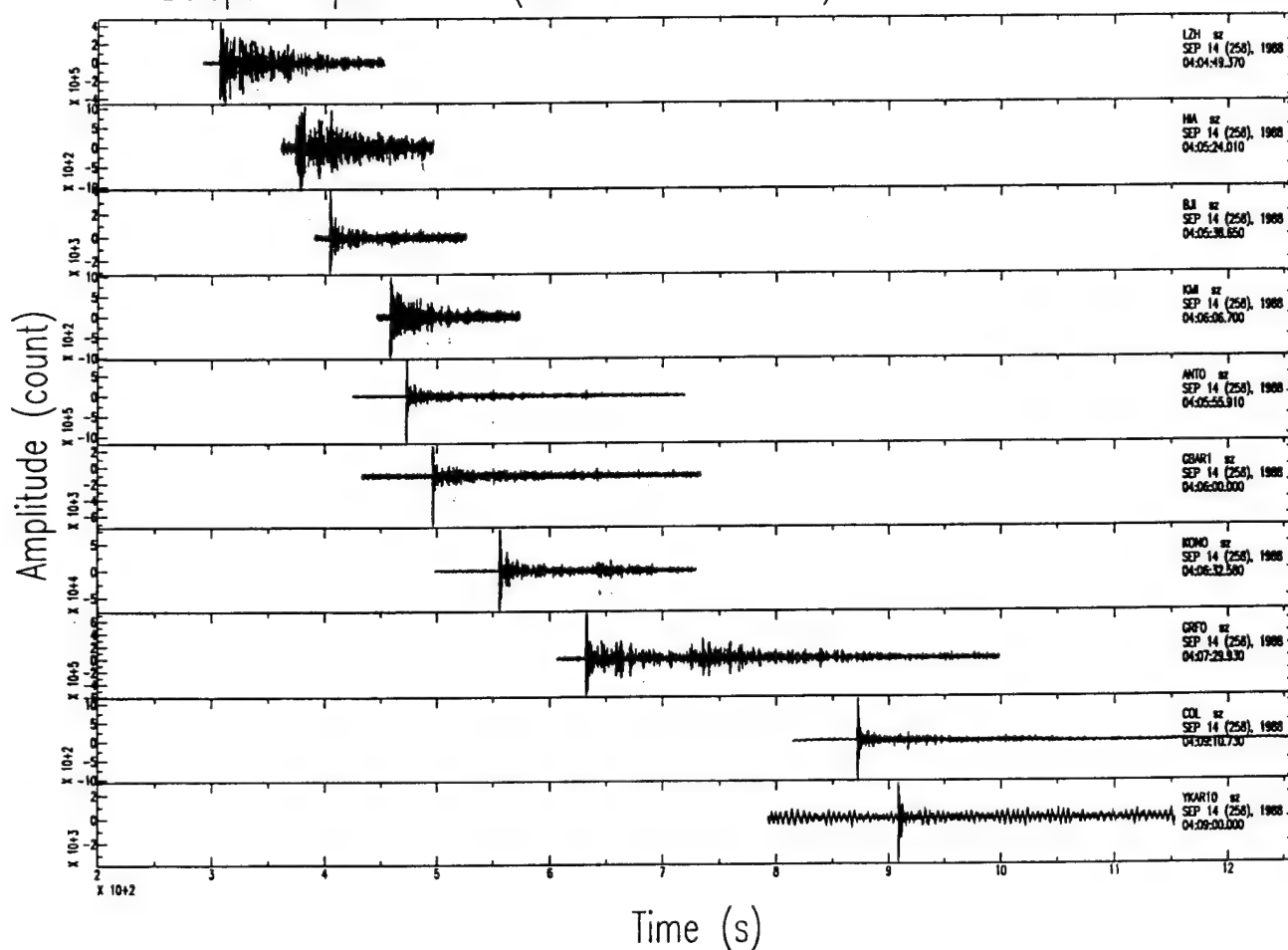


Figure 3: Short-period, vertical component seismograms of the 14 September 1988 Joint Verification Experiment (JVE) explosion (event 94) at KTS recorded at ten seismic stations at far-regional and teleseismic distances.

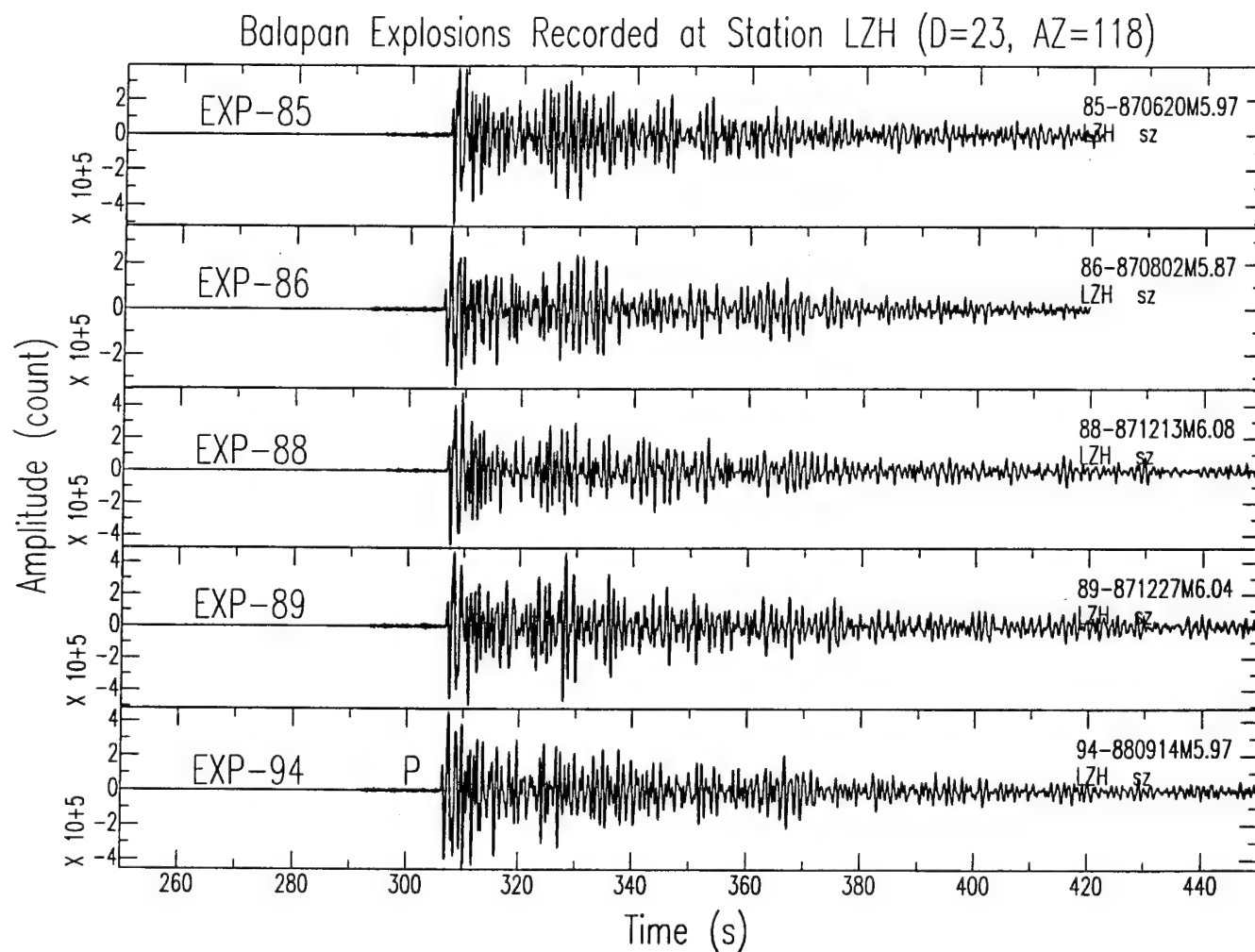


Figure 4: Vertical component seismograms of five presumed nuclear explosions recorded by station LZH at a far-regional distance. Distance (D) and azimuth (AZ) are given in the title in degrees.

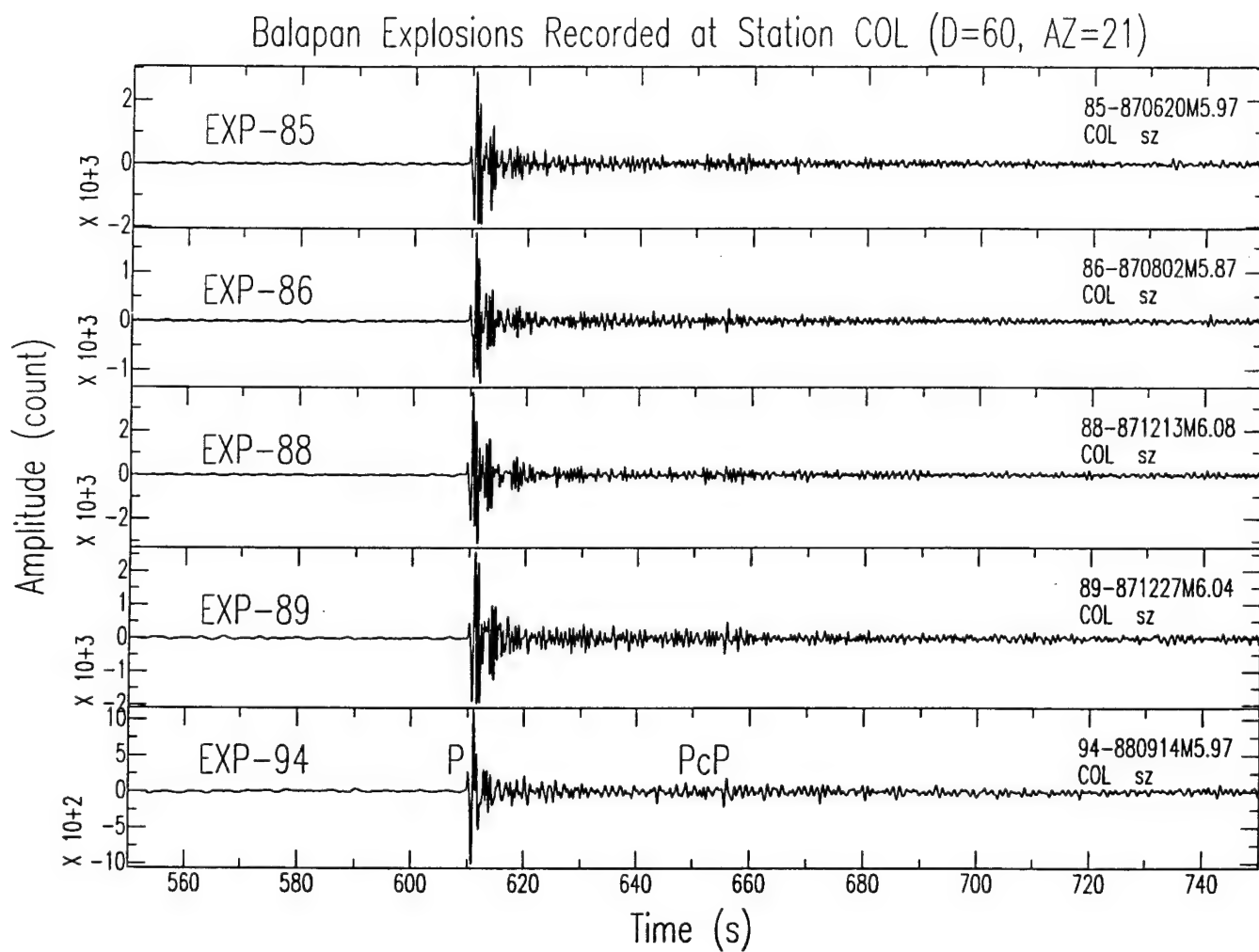


Figure 5: Vertical component seismograms of five presumed nuclear explosions recorded by station COL at a teleseismic distance.

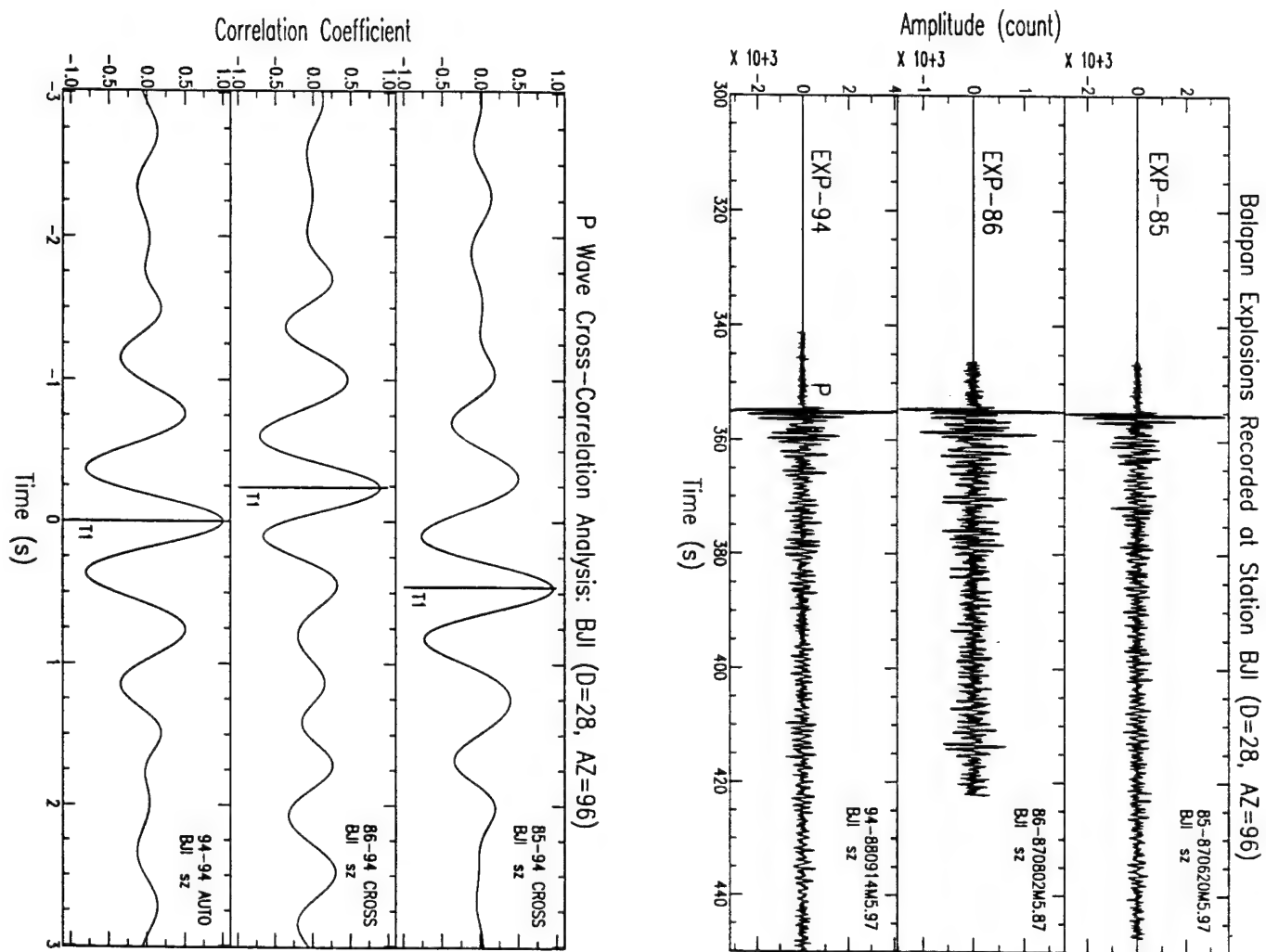


Figure 6: *Top frame*: P waves on vertical component seismograms of three explosions at KTS recorded at station BJI. *Bottom frame*: P wave cross-correlation functions for events 85 and 86 and auto-correlation function for event 94 (master event).

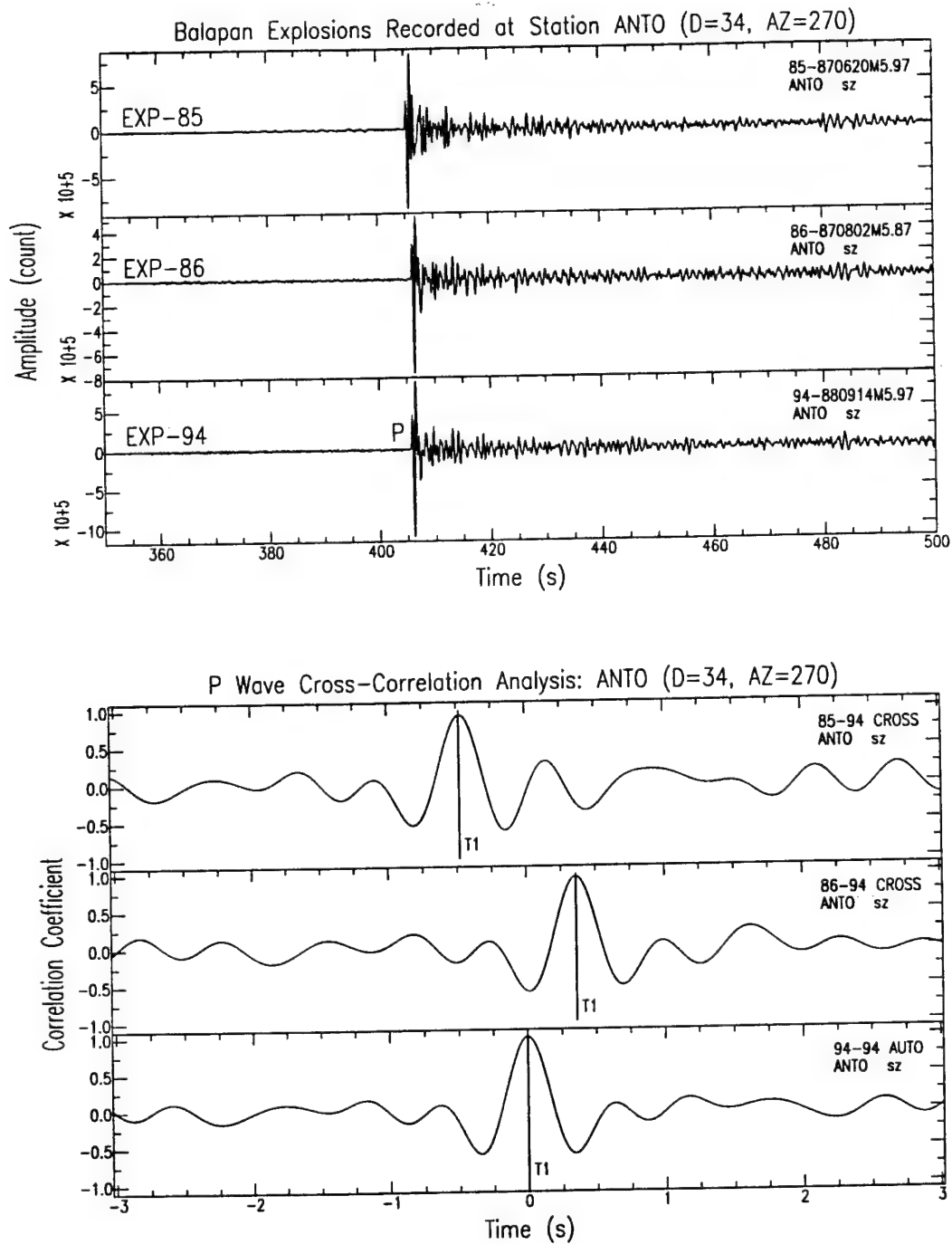


Figure 7: *Top frame*: P waves on vertical component seismograms of three explosions at KTS recorded at station ANTO. *Bottom frame*: P wave cross-correlation functions for events 85 and 86 and auto-correlation function for event 94 (master event).

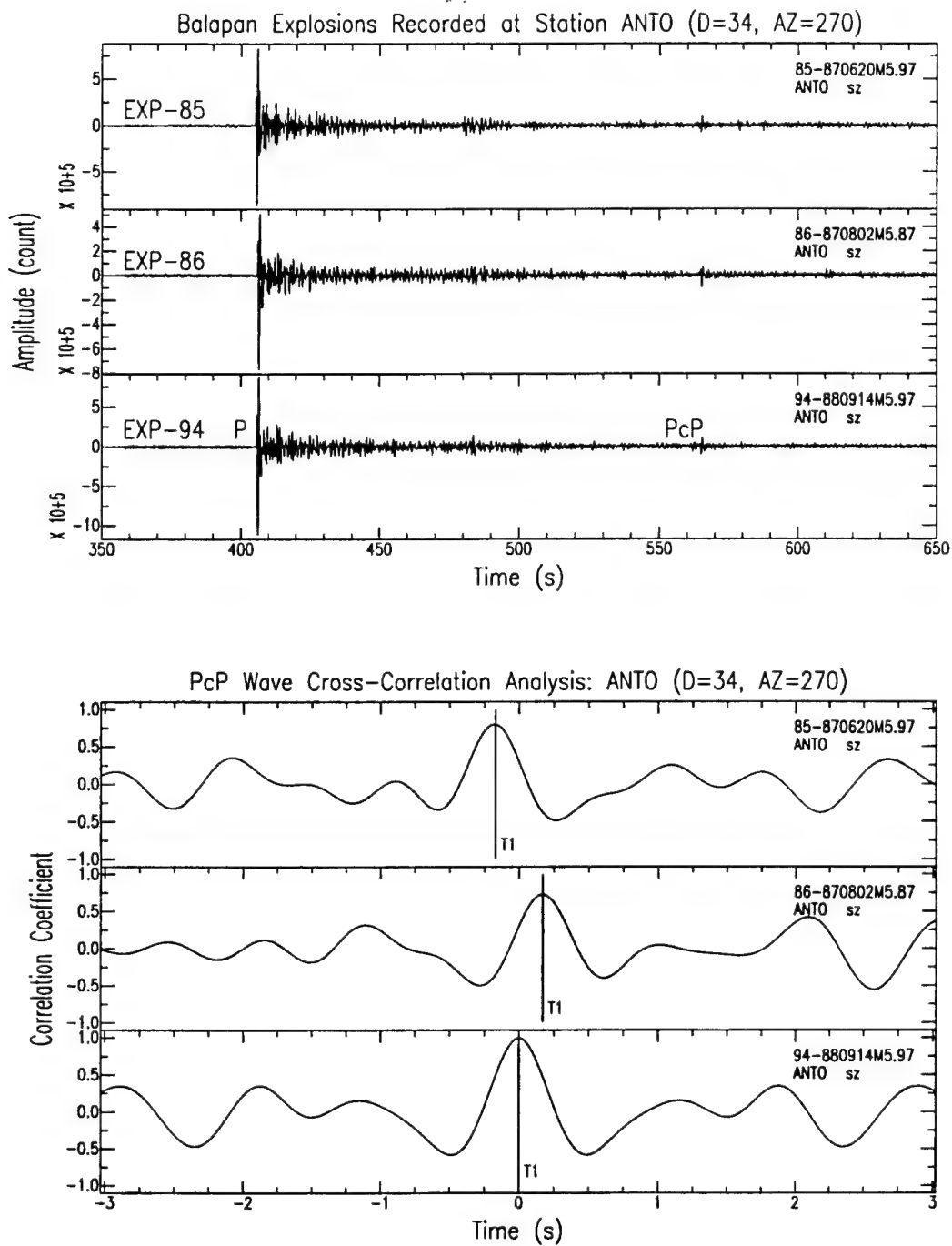


Figure 8: *Top frame:* P and PcP waves on vertical component seismograms of three explosions at KTS recorded at station ANTO. *Bottom frame:* PcP wave cross-correlation functions for events 85 and 86 and the auto-correlation function for event 94 (master event).

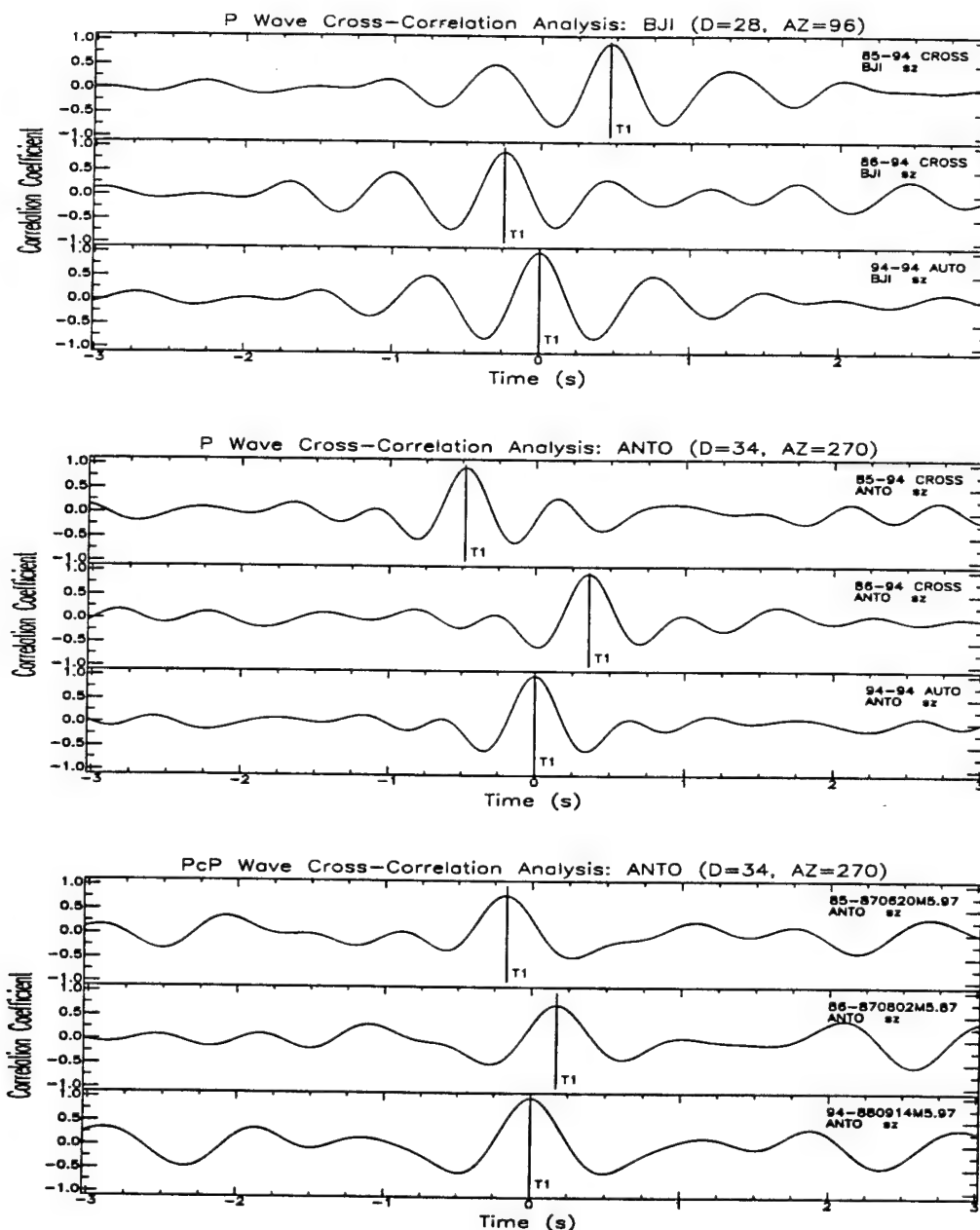


Figure 9: Comparison of cross-correlation functions at different stations and calculated with different phases. *Top frame:* P wave cross-correlation functions calculated for events 85 and 86 at station BJI. *Middle frame:* P wave cross-correlation functions calculated for events 85 and 86 at station ANTO. Note the differences between the P wave differential arrival times for the same event at different stations. *Bottom frame:* PcP wave cross-correlation functions calculated for events 85 and 86 at station ANTO.

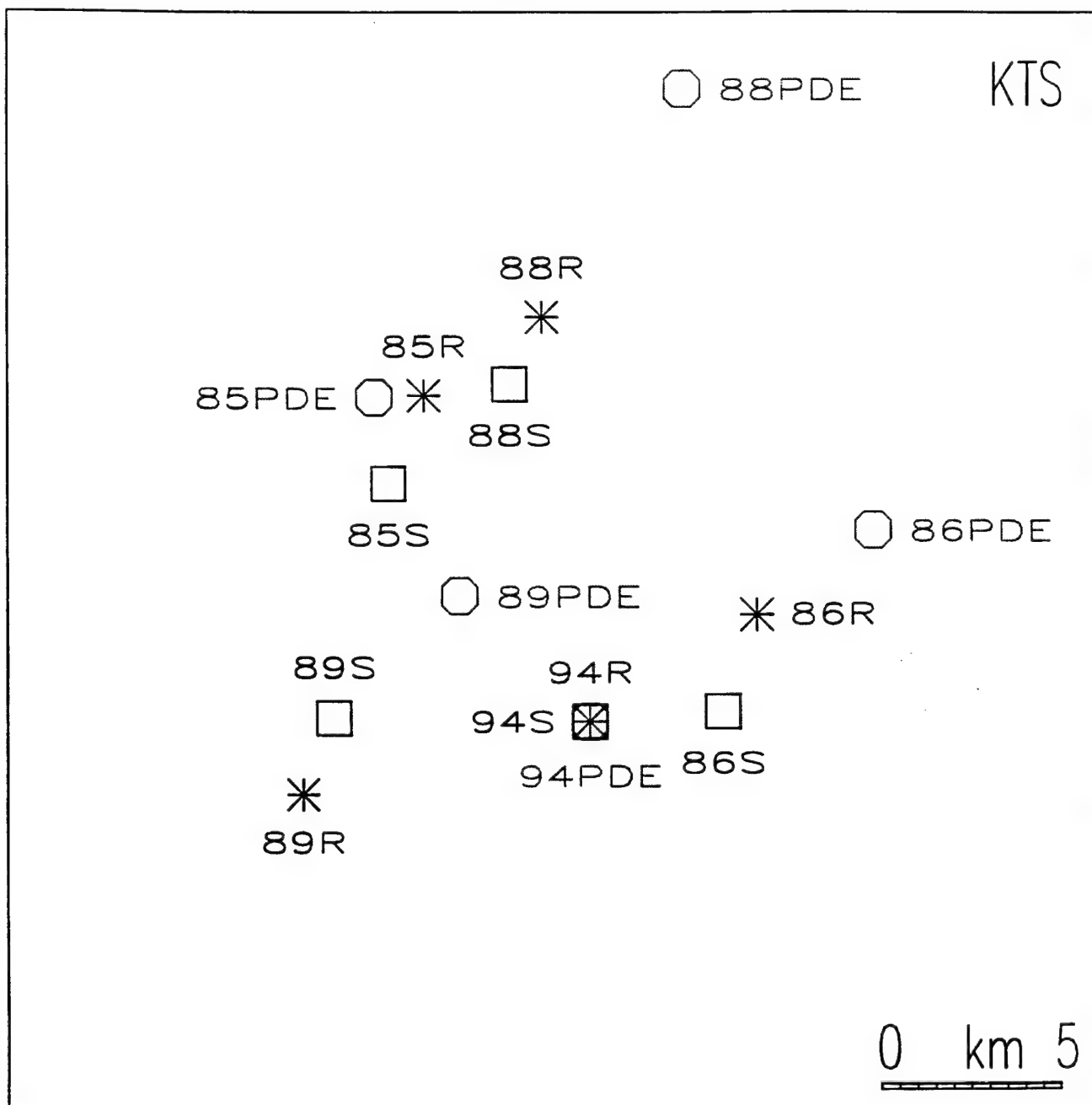


Figure 10: Comparison of our relocation results (stars) with the locations determined with satellite image analysis (squares) by Thurber, Quin and Richards (1993), and with hundreds of absolute arrival time picks by USGS (octagons).

Multipole Radiation of Seismic Waves from Explosions in Non-Spherical Cavities and its Application to Signal Identification

*Ari Ben-Menahem** and *Oleg Mikhailov*

Earth Resources Laboratory
Department of Earth, Atmospheric and Planetary Sciences
Massachusetts Institute of Technology
Cambridge, MA 02139

*On leave from the Faculty of Mathematical Sciences, Weizmann Institute of Science, Rehovot 76100, Israel.

ABSTRACT

A new method, which we name *Spherical Mapping Approximation* (SMA), is developed for the evaluation of displacement fields of body waves and surface waves from explosions in non-spherical cavities embedded in elastic media.

Under SMA, the explosion-generated stress distribution on the surface of an arbitrary cavity is mapped onto the surface of an *equivalent virtual spherical cavity* having the volume of the true cavity. The analytical results express the displacement field in terms of a multipole double-sum expansion of spherical eigenvectors with coefficients in the form of a finite *Legendre transform* of the components of the normal vector of the cavity boundary. These 'cavity integrals' can be evaluated exactly for spheroidal and cylindrical inclusions.

In the long-wave far-field approximation, symmetric finite cavities are shown to be equivalent to a linear combination of *point dipoles* directed along the principal cavity-axes. The ensuing radiation patterns yield, in general, 4-lobe patterns for S-waves, two-lobe patterns for P-waves and single to two-lobe Rayleigh-wave patterns, independent of the details of the cavities' shape. However, all radiation patterns are modulated by a frequency-dependent 'cavity-factor' that embodies the boundary conditions on the cavity surface.

Moreover, it is shown that the radiation pattern for P-waves from a non-spherical symmetrical cavity in the long-wave far-field approximation is always *dipolar*. Since the radiation pattern of radiated P-waves from a standard earthquake is always *quadrupolar*, the cavity explosion behaves like a *non double-couple earthquake*. Thus, the examination of the deviatoric moment tensor of a given seismic event enables one, in principle, to state whether it is a standard earthquake or perhaps (if the S-wave pattern is quadrupolar) an evasion of the test-ban treaty.

Displacement patterns for body and surface waves are calculated for spheroidal and cylindrical cavities for a wide range of aspect ratios and corresponding aperture angles, exhibiting the whole range of cavity shapes from a *line source* to a *disc*. The moments of the equivalent dipoles are shown to depend on the corresponding cavity-integrals, the elastic constants of the medium in the neighborhood of the source, and the initial energy injection.

All non-spherical cavities generate strong shear-waves, except for special aperture angles at which a spherical P-wave is generated, unaccompanied by S-waves.

The wave-spectra of body waves (surface waves) exhibit a corner-frequency (peak frequency) at a wavelength equal to the radius of the equivalent sphere. This enables

one to deduce the size of the cavity from the spectrum of its far-field displacement signals, provided that the explosion is fully *decoupled* and that the interaction of the shock wave with the medium occurred in the elastic regime.

The results of the present research are applicable to the detection and identification of seismic signals from clandestine underground nuclear explosions.

1. Introduction

The advent of testing underground nuclear explosions during 1957–1966 gave rise to intensive research efforts on the subject of seismic wave radiation from explosions in spherical cavities. The concept that it might be possible to significantly reduce the radiated seismic signal by detonating the device in a cavity (known as *decoupling*), was first proposed publicly by A.L. Latter at the 1959 Nuclear Test Ban Conference in Geneva (Latter *et al.*, 1961). The possibility of concealing nuclear explosions then became a vital issue in connection with the test-ban treaty, and its importance has presently increased due to the new treaty to be signed and ratified internationally in 1996.

In spite of the existence of a vast literature of the subject of decoupling [Latter *et al.*, 1959; Latter *et al.*, 1961a,b; Haskell, 1961; Herbst *et al.*, 1961; Patterson, 1966; Springer, 1966; Werth and Randolph, 1966; Rogers, 1966; Lewin and Treiman, 1966; Rawson *et al.*, 1966; Haskell, 1967; Springer *et al.*, 1968; King *et al.*, 1989; Stevens *et al.*, 1991; Adushkin *et al.*, 1993; Florence and Miller, 1993; Glenn, 1993], a number of major issues of importance w.r.t. seismic monitoring still remain unsolved.

Elastodynamical problems associated with spheres and spherical cavities were solved throughout the 19th century by many mathematical physicists (Love, 1927). However, the first application of a problem of this type to seismology was made only in 1942 by Sharpe; he gave explicit expressions for the time-domain ground displacements produced by chemical explosion pressure in a finite cavity embedded in an unbounded elastic solid.

Sharpe's solution assumes total spherical symmetry of the source *and* the medium. It therefore predicts a radial displacement everywhere and the absence of shear waves.

However, seismograms produced by underground nuclear explosions are considerably more complicated than what one would expect from Sharpe's simple model (e.g. Toksöz *et al.*, 1964; Johnson, 1988; Taylor *et al.*, 1991).

Numerous attempts were made during the past four decades to account for

these observations in terms of *media complexities* (inhomogeneity, anisotropy, pre-stress, nonlinearity) or *source complexities* (asphericity, spall). But a serious attempt to extend Sharpe's analytical solution beyond that of a spherical cavity was lacking. For this reason, all scaling laws used to date (King *et al.*, 1989; Stevens *et al.*, 1991; Adushkin *et al.*, 1993; Florence and Miller, 1993) to estimate the yield of nuclear explosions from the seismic data are still based on a modification of Sharpe's solution given by Haskell (1961, 1967).

In surveying the literature on the subject since 1942, we could discern two main avenues of approach:

I. Helmholtz-type integral formulas: These illustrate Huygen's principle for the two wave fronts of the elastic wave field via a vector Green's theorem. It is known also as the 'Representation Theorem' (Ben-Menahem and Singh, 1981, p. 174) and states that the displacement field \vec{u} outside the source region is given by two surface integrals over the confining cavity S

$$\vec{u}(\vec{r}) = \int_S \vec{F}(\vec{\xi}) \cdot \vec{G}(\vec{r} | \vec{\xi}) dS(\vec{\xi}) - \int_S \vec{u}(\vec{\xi}) \vec{n}(\vec{\xi}) : \overset{3}{T}_{\xi} \{ \vec{G}(\vec{r} | \vec{\xi}) \} dS(\vec{\xi}). \quad (1)$$

Here $\vec{\xi}$ are source-coordinates, $\vec{n}(\vec{\xi})$ is the outward unit normal vector to S , $\vec{F}(\vec{\xi}) = \vec{n}(\vec{\xi}) \cdot \vec{T}(\vec{u})$ is the normal traction vector, dS is the surface area element, $\vec{G}(\vec{r} | \vec{\xi})$ is the Green's tensor for the elastic medium (finite or infinite), $\vec{T}(\vec{u}) = \lambda \vec{I} \text{div } \vec{u} + \mu(\nabla \vec{u} + \vec{u} \nabla)$ is the stress dyadic, while $\overset{3}{T}$ is a stress tryadic (third rank Green's stress tensor). It is given explicitly in either index-free or indicial form

$$\begin{aligned} \overset{3}{T}_{\xi}(\vec{r} | \vec{\xi}) &= \lambda \vec{I} \text{div}_{\xi} \vec{G}(\vec{r} | \vec{\xi}) + \mu(\vec{\nabla}_{\xi} \vec{G} + \vec{G}_{\xi} \vec{\nabla}), \\ \{\overset{3}{T}\}_{\ell mn} &= \lambda \delta_{\ell n} \partial_k G_{\ell m} + \mu \partial_{\ell} G_{mn} + \partial_m G_{\ell n}, \end{aligned} \quad (2)$$

where $\partial_m = \frac{\partial}{\partial x_m}$.

Since $\vec{F}(\vec{\xi})$ is usually given and \vec{G} is known, the first integral of (1) can be evaluated, analytically or numerically, on S . The second integral, requires the preknowledge of the displacements on S . Since in most cases, this function is apriori unknown, it must be first calculated from (1) itself, acting to this end as an *integral equation* for \vec{u} on S . This drawback, apart from the nontrivial integration over S , makes this approach quite tedious.

Varadan (1976), mitigated the hardships of the integral-formula approach by applying to it the method of eigenfunction-expansion, well-known from the theory of integral equations (e.g. Kondon, 1991). He expands $\vec{F}(\vec{\xi})$, \vec{u} , \vec{G} , and $\overset{3}{T}(\vec{G})$ in

terms of a spherical eigenvector base, and solves for the unknown coefficients of the expansion of the displacements $\vec{u}(\vec{r})$. An infinite matrix is involved, but in many cases good accuracy can be obtained with a truncated matrix of 60×60 .

Glenn *et al.* (1985) and Rial and Moran (1986) solved (1) numerically for the surface displacement over a spheroid. A finite element code was used to compute the displacement on the cavity surface and then (1) was used again to find the displacements in the far-field. No analytic solution was given. But the singular nature of the integral, when the observer point is on the surface, makes it difficult to apply this scheme to arbitrary cavity geometries. Also, the finite-element solution is computationally inefficient for direct calculation of the far-field.

Stevens *et al.* (1991) reported non-analytic finite difference simulations of partially-coupled explosions in an ellipsoidal cavity having an aspect ratio of 4 to 1. Since their report includes no visible mathematics, except for a flat statement that they have integrated Eq. (1) numerically in the time domain for the far-field, a straightforward evaluation of their results is not feasible.

II. Boundary-value solutions for non-spherical configuration: Heelan (1953) has tried to solve the problem of radiation from a cylindrical cavity in an isotropic infinite elastic space. He assumed a cylindrical hole of infinite length with a prescribed stress applied to a finite length of its wall, which is *not* a cavity. But even so, his solution is plagued with serious analytical inaccuracies (Abo-Zena, 1977; Usami and Hirono, 1956). Hazebroek (1966) considered a special case of a finite line source given as a limit of a narrow elongated ellipsoid of revolution whose minor axis tends to zero. The interior surface of this ellipsoid is subjected to a pressure which is a given function of the time only. It was concluded that the shape and magnitude of the compressional waves were independent of direction and that the magnitude of the shear wave is maximum at an angle of 45° to the direction of the line source.

Usami and Hirono (1956) and Usami (1958) considered the elastic wave generated from prolate and oblate spheroidal cavities whose walls were subjected to normal harmonic stress. The above authors used spheroidal coordinates from the start, and their solution is therefore expressed in terms of the spheroidal Baer eigenfunctions (Moon and Spencer, 1971) which are eventually expanded in terms of spherical Bessel functions. Their numerical calculations revealed for the ratio $d = \left\{ \frac{\text{radiation's wavelengths}}{\text{source's length}} \right\} \sim 3$, a 4-lobe radiation pattern for compressional waves in the far-field.

Zhao and Harkrider (1992) gave an analytic formulation for the wave fields from an off-center explosion in an embedded solid sphere in an elastic whole-space. Their calculations show that the degree of shear-wave generation is determined by the asymmetry of the source region. The radiation patterns at different periods for different parameters of the media suggest that the asymmetry of the source

region has significant effects on spectral components with the ratio $d \leq 7$. Their model was intended to simulate a *tamped* nuclear explosion.

A more realistic model of an underground nuclear explosion in a preexisting cavity requires the presence of a stress-free planar boundary to accommodate for the earth's surface. Analytically, this problem is of a higher degree of complexity since it involves the simultaneous use of two different coordinate system — the spherical and the cylindrical.

The first attempt to solve this difficult problem is due to Ben-Menahem and Cisternas (1963), who used the 'Erdelyi Integral Formula' to transform the elastic fields between the two said coordinates. The convergence of their solution was later established by Thiruvengkatachar and Viswanathan (1965) and Gregory (1967).

The present paper offers a new simplified approach which is especially suitable to the physical conditions prevailing in underground nuclear explosions. The basic assumption (supported by observations over the past forty years) states that irrespective of the shape of the cavity or the point at which explosive device is placed in it — the *direction* of pressure on its walls is always normal to the walls at every point, such that there is no initial tangential force. The pressure on the walls is activated practically *simultaneously* at all points of the boundary.

We analyze comparatively three typical situations, listed in increasing order of complexity (Fig. 1):

- (a) Source at the center of a spherical cavity. The initial traction vector on the wall is radial and uniform at all points. No shear waves are produced in the outside homogeneous elastic medium at any time (Fig. 1a).
- (b) Source is at the center of a spheroidal cavity (Fig. 1b). Since the normal is not in the radial direction from the center, *shear waves* are produced ab initio in the elastic medium. One can then simulate the problem in terms of a *mapping* of the stress distribution on the surface of an *equivalent virtual spherical cavity*. Details of this process are given in Section 2.
- (c) A stress-free planar boundary is introduced to model an underground explosion in a tunnel whose major axis is parallel to the free surface (Fig. 1c).

With this step accomplished, the source-field of an *oblate* spheroid in an infinite medium is obtained¹. The second step included the integral transformation of the spherical eigenvectors into cylindrical eigenvectors, appropriate for the new boundary conditions needed over the planar boundary. Once the boundary conditions are stated, the residues at the poles of the integral expressions are evaluated in order to obtain a closed-form expressions for the *Rayleigh wave field*.

The results of the above cases are calculated and exhibited in graphical form

¹ By 'oblate' we mean here that the cavity has a horizontal axis of symmetry.

which emphasize the dependence of the field on the explosion geometry and source frequency. The shape of the cavity strongly affect the ensuing *radiation patterns*.

The new idea of the equivalent spherical cavity is very helpful in bringing about the essential features of the resulting elastodynamic field that is transmitted outwards from the cavity. Clearly, we are not able to quantify the entire complex physical process of an underground nuclear explosion, due to lack of measurements in the cavity and its adjacent neighborhood during the first few milliseconds or so after the explosion. But practically we are interested only in that tiny fraction of energy that is converted into seismic waves. Since the boundary conditions associated with this conversion are only vaguely known, there is no sense in being too exact in the mathematical elastic model. Thus, instead of giving an exact mathematical solution to an approximate physical situation, we prefer to give an approximate mathematical solution to an equivalent physical model, which we have precisely formulated.

2. The Spherical Mapping Approximation

Consider first a *spherical* cavity of radius $r = r_0$ that is subjected to a prescribed distribution of stresses on its inner wall. To establish the displacement field \vec{u} at an observation point \vec{r} outside the cavity we assume an expansion of the field in terms of the Hansen spherical eigenvectors (Appendix A),

$$\vec{u}(\vec{r}) = \sum_{m,\ell} [\alpha_{m\ell} \vec{M}_{m\ell}^-(k_s r) + \beta_{m\ell} \vec{N}_{m\ell}^-(k_s r) + \gamma_{m\ell} \vec{L}_{m\ell}^-(k_p r)], \quad (3)$$

where $k_p = \frac{\omega}{v_p}$, $k_s = \frac{\omega}{v_s}$ and ω is the angular frequency. Let the boundary conditions at the surface of the cavity be

$$\vec{e}_r \cdot \vec{T}(\vec{u}) = \vec{F}(\theta, \varphi) \quad \text{at} \quad r = r_0, \quad (4)$$

where \vec{e}_r is a unit vector in the direction of increasing r , and $\vec{T}(\vec{u}) = \lambda I \text{div} \vec{u} + \mu(\nabla \vec{u} + \vec{u} \nabla)$ is the stress dyadic in a medium having the Lamé coefficients λ, μ . Since \vec{F} is known, it can be expanded into a series of vector spherical harmonics $\{\vec{P}_{m\ell}, \vec{B}_{m\ell}, \vec{C}_{m\ell}\}$ with determinable coefficients $\{\alpha_{m\ell}^0, \beta_{m\ell}^0, \gamma_{m\ell}^0\}$ (Ben-Menahem and Singh, 1981, pp. 221-222)

$$\vec{F}(\theta, \varphi) = \sum_{m,\ell} [\alpha_{m\ell}^0 \sqrt{\ell(\ell+1)} \vec{C}_{m\ell} + \beta_{m\ell}^0 \vec{P}_{m\ell} + \gamma_{m\ell}^0 \sqrt{\ell(\ell+1)} \vec{B}_{m\ell}]. \quad (5)$$

The explicit expressions for the vectors $\{\vec{M}_{m\ell}^\pm, \vec{N}_{m\ell}^\pm, \vec{L}_{m\ell}^\pm\}$ and $\{\vec{P}_{m\ell}, \vec{B}_{m\ell}, \vec{C}_{m\ell}\}$ is given in Appendix A.

Inserting \vec{u} from (3) into (4), straightforward calculations lead to the explicit expressions for the unknown displacement coefficients in terms of the known stress distribution

$$\alpha_{m\ell} = \frac{\alpha_{m\ell}^0}{\mu k_s} \frac{1}{\chi F_{\ell,1}(\chi)}, \quad (6)$$

$$\beta_{m\ell} = \frac{1}{\mu k_s} \frac{\beta_{m\ell}^0 F_{\ell,1}(\zeta) - \gamma_{m\ell}^0 F_{\ell,3}(\zeta)}{\Delta_\ell}, \quad (7)$$

$$\gamma_{m\ell} = \frac{1}{2\mu k_p} \frac{-\beta_{m\ell}^0 F_{\ell,2}(\chi) + 2\ell(\ell+1)\gamma_{m\ell}^0 F_{\ell,1}(\chi)}{\Delta_\ell},$$

where

$$\left. \begin{aligned} \chi &= k_s r_0, & \zeta &= k_p r_0, \\ \Delta_\ell &= 2\ell(\ell+1)F_{\ell,1}(\chi)F_{\ell,1}(\zeta) - F_{\ell,2}(\chi)F_{\ell,3}(\zeta), \\ F_{\ell,1}(x) &= \frac{\ell-1}{x^2}h_\ell^{(2)}(x) - \frac{1}{x}h_{\ell+1}^{(2)}(x), \\ F_{\ell,2}(x) &= \left[\frac{2}{x^2}(\ell^2-1) - 1 \right] h_\ell^{(2)}(x) + \frac{2}{x}h_{\ell+1}^{(2)}(x), \\ F_{\ell,3}(x) &= \left[\frac{1}{x^2}\ell(\ell-1) - \frac{1}{2}\left(\frac{\alpha}{\beta}\right)^2 \right] h_\ell^{(2)}(x) + \frac{2}{x}h_{\ell+1}^{(2)}(x), \\ h_\ell^{(2)} &= \text{spherical Hankel function of the second kind.} \end{aligned} \right\} \quad (8)$$

The above analysis can be applied to model an explosion in a preexisting cavity; whatever the geometrical shape of the cavity, the explosion gas is assumed to exert on its walls a uniform pressure equal to $p_0(\omega)\vec{n}$, where \vec{n} is a unit normal to any given point and $p_0(\omega)$ is the Fourier transform of the time-dependence of the initial stress-pulse. In the case of a sphere $\vec{n} = \vec{e}_r$ is the unit radial vector in spherical coordinates. In the general case $\vec{n} = \vec{\nabla}S/|\vec{\nabla}S|$, where $S(x, y, z) = 0$ is the equation of the cavities' surface. Because the boundary conditions require that the normal stress \vec{F}_n at the surface of the cavity be equal to the negative of the applied pressure, we write

$$\begin{aligned} \vec{F}_n[r(\theta, \varphi); \theta, \varphi] \big|_s &= -p_0(\omega)\vec{n} \\ &= -p_0(\omega)[f(\theta, \varphi)\vec{e}_r + g(\theta, \varphi)\vec{e}_\theta + h(\theta, \varphi)\vec{e}_\varphi], \end{aligned} \quad (9)$$

where $\{r, \theta, \varphi\}$ are the spherical coordinates of a point on S (Fig. 1), and $\{f, g, h\}$ depend on the geometry of the surface S . Since the surface of the cavity after the explosion does not remain intact due to non-elastic deformations, the physics of the problem can accommodate a mathematical simplification: instead of applying the boundary conditions on the aspherical cavity, we map them on the walls of

a *virtual spherical cavity* which has the *same volume as the real cavity*. The geometry of the original cavity still enters via the angular dependence of \vec{n} .

With this provision, the mathematical apparatus expounded in (1)-(7) can be applied directly. Since in nuclear explosions the distances involved in changing from S to the sphere $r = r_0$ are of the order of a few meters only, the travel-time error incurred will be of the order of a few milliseconds, which is totally negligible. Hence, we are able to avoid the use of horrendous integrations over aspherical surfaces as required by other methods (e.g. Varatharajulu and Pao, 1976).

Let $S(r, \theta, \varphi; \epsilon) = 0$ represent a smooth surface in three dimensional Euclidean space, where (r, θ, φ) are the spherical coordinates of a general point of S relative to some origin (usually chosen inside S) and $0 < \epsilon < 1$ is a dimensionless geometrical parameter. We shall assume that the components of $\vec{\nabla}S$, together with their first and second derivatives are continuous functions of θ and φ in the range $0 < \theta < \pi$, $0 < \varphi < 2\pi$.

The explicit expression for the normal to S is

$$\vec{n} = \frac{\vec{\nabla}S}{|\vec{\nabla}S|} = f(\theta, \varphi; \epsilon)\vec{e}_r + g(\theta, \varphi; \epsilon)\vec{e}_\theta + h(\theta, \varphi; \epsilon)\vec{e}_\varphi, \quad (10)$$

where

$$\begin{aligned} f &= \frac{1}{\Delta} \frac{\partial S}{\partial r}, & g &= \frac{1}{\Delta r} \frac{\partial S}{\partial \theta}, & h &= \frac{1}{\Delta r \sin \theta} \frac{\partial S}{\partial \varphi}, \\ \Delta &= \left[\left(\frac{\partial S}{\partial r} \right)^2 + \frac{1}{r^2} \left(\frac{\partial S}{\partial \theta} \right)^2 + \frac{1}{r^2 \sin^2 \theta} \left(\frac{\partial S}{\partial \varphi} \right)^2 \right]^{1/2}. \end{aligned} \quad (11)$$

For a given surface S , such that (f, g, h) together with their first and second derivatives are continuous functions of θ and φ over the entire range of (θ, φ) , we may seek an expansion of the vector normal \vec{n} in terms of the *vector spherical harmonics* (Appendix A)

$$\vec{n} = \sum_{\ell=0}^{\infty} \sum_{m=-\ell}^{\ell} [f_{\ell m} \vec{P}_{\ell m} + g_{\ell m} \sqrt{\ell(\ell+1)} \vec{B}_{\ell m} + h_{\ell m} \sqrt{\ell(\ell+1)} \vec{C}_{\ell m}]. \quad (12)$$

Using the orthogonality relations of the scalar spherical harmonics, the coefficients $\{f_{\ell m}, g_{\ell m}, h_{\ell m}\}$ are explicitly recoverable in terms of the *known* functions $\{f, g, h\}$

$$\begin{aligned} f_{\ell m} &= \frac{2\ell+1}{4\pi} \frac{(\ell-m)!}{(\ell+m)!} \int_0^{2\pi} d\varphi \int_0^\pi f(\theta, \varphi; \epsilon) \{P_\ell^m(\cos \theta) e^{-im\varphi}\} \sin \theta d\theta, \\ g_{\ell m} &= \frac{2\ell+1}{4\pi \ell(\ell+1)} \frac{(\ell-m)!}{(\ell+m)!} \int_0^{2\pi} d\varphi \int_0^\pi \left\{ g(\theta, \varphi; \epsilon) \frac{\partial}{\partial \theta} + \frac{1}{\sin \theta} h(\theta, \varphi; \epsilon) \frac{\partial}{\partial \varphi} \right\} \end{aligned} \quad (13)$$

$$\times \{P_\ell^m(\cos \theta)e^{-im\varphi}\} \sin \theta d\theta, \quad (14)$$

$$h_{m\ell} = \frac{2\ell+1}{4\pi\ell(\ell+1)} \frac{(\ell-m)!}{(\ell+m)!} \int_0^{2\pi} d\varphi \int_0^\pi \left\{ \frac{1}{\sin \theta} g(\theta, \varphi; \epsilon) \frac{\partial}{\partial \varphi} - h(\theta, \varphi; \epsilon) \frac{\partial}{\partial \theta} \right\} \\ \times \{P_\ell^m(\cos \theta)e^{-im\varphi}\} \sin \theta d\theta. \quad (15)$$

In the special case of azimuthally-symmetric surfaces $[\frac{\partial S}{\partial \varphi} = 0, h \equiv 0]$, the above results simplify to

$$f_\ell = \frac{2\ell+1}{2} \int_0^\pi f(\theta, \varphi; \epsilon) P_\ell(\cos \theta) \sin \theta d\theta, \quad (16)$$

$$g_\ell = \frac{2\ell+1}{2\ell(\ell+1)} \int_0^\pi g(\theta, \varphi; \epsilon) \frac{\partial}{\partial \theta} P_\ell(\cos \theta) \sin \theta d\theta, \quad \ell \geq 1, \quad (17)$$

$$g_0 = 0.$$

Applying the stress distribution given in (9)–(10) to (6), using (6)–(8), we find by comparison, for all values of ℓ and m

$$\beta_{m\ell}^0 = -p_0(\omega) f_{m\ell}, \quad \gamma_{m\ell}^0 = -p_0(\omega) g_{m\ell}, \quad \alpha_{m\ell}^0 = -p_0(\omega) h_{m\ell}. \quad (18)$$

The final expressions for the respective compressional (P) and shear (S) displacement fields at locations $r > r_0$, are obtained via (3)–(8)

$$\vec{u}_p(\vec{r}; \omega) = \frac{p_0(\omega)}{2\mu k_p} \sum_{m,\ell} \frac{f_{m\ell} F_{\ell,2}(k_s r_0) - 2\ell(\ell+1) g_{m\ell} F_{\ell,1}(k_s r_0)}{\Delta_\ell} \vec{L}_{m\ell}^-(k_p r), \quad (19)$$

$$\vec{u}_s(\vec{r}; \omega) = -\frac{p_0(\omega)}{\mu k_s} \sum_{m,\ell} \left[\frac{h_{m\ell}}{(k_s r_0) F_{\ell,1}(k_s r_0)} \vec{M}_{m\ell}^-(k_s r) \right. \\ \left. + \frac{f_{m\ell} F_{\ell,1}(k_p r_0) - g_{m\ell} F_{\ell,3}(k_p r_0)}{\Delta_\ell} \vec{N}_{m\ell}^-(k_s r) \right]. \quad (20)$$

For azimuthally-symmetric surfaces, (19)–(20) degenerate into the simpler form

$$\vec{u}_p(\vec{r}, \omega) = \frac{p_0(\omega)}{2\mu k_p} \sum_{\ell=0,2,4,\dots} \left[f_\ell(\epsilon) \frac{F_{\ell,2}(k_s r)}{\Delta_\ell} - 2\ell(\ell+1) g_\ell(\epsilon) \frac{F_{\ell,1}(k_s r)}{\Delta_\ell} \right] \\ \times \vec{L}_{0\ell}^-(k_p r_0), \quad (21)$$

$$\vec{u}_s(\vec{r}, \omega) = -\frac{p_0(\omega)}{\mu k_s} \sum_{\ell=0,2,4,\dots} \left[f_\ell(\epsilon) \frac{F_{\ell,1}(k_p r)}{\Delta_\ell} - g_\ell(\epsilon) \frac{F_{\ell,3}(k_p r)}{\Delta_\ell} \right] \\ \times \vec{N}_{0\ell}^-(k_s r), \quad (22)$$

where $\bar{N}_{0,0}^-(k_s r) \equiv 0$.

The above equations are recastable in the explicit component-form:

P-waves:

$$\begin{aligned} u_r &= \frac{p_0(\omega)}{\mu k_p} \sum_{\ell} A_{\ell}(k_s r_0; \epsilon) P_{\ell}(\cos \theta) h_{\ell}^{(2)}(k_p r) \\ u_{\theta} &= \frac{p_0(\omega)}{\mu k_p} \sum_{\ell} A_{\ell}(k_s r_0; \epsilon) \frac{\partial P_{\ell}(\cos \theta)}{\partial \theta} \frac{h_{\ell}^{(2)}(k_p r)}{k_p r}. \end{aligned} \quad (23)$$

S-waves:

$$\begin{aligned} u_r &= -\frac{p_0(\omega)}{\mu k_p} \sum_{\ell} B_{\ell}(k_p r_0; \epsilon) \ell(\ell+1) P_{\ell}(\cos \theta) \frac{h_{\ell}^{(2)}(k_s r)}{k_s r}, \\ u_{\theta} &= -\frac{p_0(\omega)}{\mu k_p} \sum_{\ell} B_{\ell}(k_p r_0; \epsilon) \frac{\partial P_{\ell}(\cos \theta)}{\partial \theta} \left[h_{\ell}^{(2)}(k_p r) + \frac{h_{\ell}^{(2)}(k_p r)}{k_p r} \right], \end{aligned} \quad (24)$$

where

$$A_{\ell}(k_s r_0; \epsilon) = f_{\ell}(\epsilon) \frac{F_{\ell,2}(k_s r_0)}{2\Delta_{\ell}} - \ell(\ell+1) g_{\ell}(\epsilon) \frac{F_{\ell,1}(k_s r_0)}{\Delta_{\ell}}, \quad (25)$$

$$B_{\ell}(k_p r_0; \epsilon) = \left[f_{\ell}(\epsilon) \frac{F_{\ell,1}(k_p r_0)}{\Delta_{\ell}} - g_{\ell}(\epsilon) \frac{F_{\ell,3}(k_p r_0)}{\Delta_{\ell}} \right] \frac{k_p}{k_s}. \quad (26)$$

For a *spherical* cavity $g_{\ell} \equiv 0$, $f_{\ell} \equiv \delta_{\ell 0}$ and (21)–(22) reduce to the well known result (Ben-Menahem and Singh, 1981, p. 222):

$$\vec{u}_p = -\frac{p_0(\omega)}{2\mu k_p} \frac{1}{F_{0,3}(k_p r_0)} \vec{L}_{0,0}^-(k_p r), \quad \vec{u}_s \equiv 0. \quad (27)$$

This expression can also be recast in the more explicit form

$$\begin{aligned} \vec{u}_p(\vec{r}, \omega) &= -\text{grad} \left[\frac{e^{i\omega(t-(r/v_p))}}{r} \frac{p_0(\omega) a^3}{4\mu} \frac{\omega_0^2 c^{i\omega/\omega_0}}{\omega_0^2 + i\omega\omega_0 - \omega^2 \frac{\lambda+2\mu}{4\mu}} \right] \\ &= -\text{grad} \Psi, \end{aligned} \quad (28)$$

where $\Psi(t \rightarrow \infty) = \Psi(\omega \rightarrow 0) = \frac{p_0 a^3}{4\mu r}$, $\omega_0 = \frac{v_p}{a}$ and $u(t \rightarrow \infty) = \frac{p_0 a^3}{4\mu r^2}$ (static deformation field).

3. Application to Realistic Cavity Shapes

We next apply our ideas to the simplest departure from a sphere that is adequate to model underground tunnels. A *spheroidal* cavity with semi-major axis c (directed along the z axis) and semi-minor axes equal to a is surrounded by an infinite homogeneous and isotropic elastic solid with Lamé coefficients λ , μ , density ρ and a Poisson ratio σ . The origin of the coordinates coincides with the spheroid's center (Fig. 2).

Let the spheroidal surface be given by the equation

$$S(x, y, z) = \frac{1}{a^2}(x^2 + y^2) + \frac{1}{c^2}z^2 - 1 = 0, \quad (29)$$

where $c > a$ is the major semi-axis, and (x, y, z) are the cartesian coordinates of any point P on the surface. The normal at the surface is given by the unit vector $\vec{n} = \nabla S / |\nabla S|$. Expressing this vector in spherical coordinates at $P(r, \theta, \varphi)$, we obtain, after simple analysis

$$\vec{n} = \vec{e}_r f(\theta; \epsilon) + \vec{e}_\theta g(\theta; \epsilon); \quad \epsilon = \frac{a}{c} < 1, \quad f^2 + g^2 \equiv 1, \quad (30)$$

where $(\vec{e}_r, \vec{e}_\theta, \vec{e}_\varphi)$ are unit vectors in the spherical system, and

$$f(\theta; \epsilon) = \frac{1 - (1 - \epsilon^2) \cos^2 \theta}{\sqrt{1 - (1 - \epsilon^4) \cos^2 \theta}}, \quad g(\theta; \epsilon) = \frac{(1 - \epsilon^2) \sin \theta \cos \theta}{\sqrt{1 - (1 - \epsilon^4) \cos^2 \theta}}. \quad (31)$$

According to (16)–(17), the explicit expression for the coefficients f_ℓ and g_ℓ will be of the form of *finite Legendre transforms*

$$f_\ell = \left(\ell + \frac{1}{2}\right) \int_0^\pi \frac{1 - (1 - \epsilon^2) \cos^2 \theta}{\sqrt{1 - (1 - \epsilon^4) \cos^2 \theta}} P_\ell(\cos \theta) \sin \theta d\theta, \quad (32)$$

$$g_\ell = -\frac{\ell + \frac{1}{2}}{\ell(\ell + 1)} \int_0^\pi \frac{(1 - \epsilon^2) \sin \theta \cos \theta}{\sqrt{1 - (1 - \epsilon^4) \cos^2 \theta}} P'_\ell(\cos \theta) \sin^2 \theta d\theta, \quad g_0 \equiv 0, \quad (33)$$

where prime indicates differentiation w.r.t. $(\cos \theta)$.

Both integrals vanish for *odd* values of ℓ . It is shown in Appendix B that f_ℓ and g_ℓ can be represented as a *finite* sum of integrals of the type

$$I_{2j} = \int_{\xi_0}^{\pi/2} \cos^{2j} \xi d\xi, \quad (34)$$

where j is an integer and $\cos \xi_0 = \sqrt{1 - \epsilon^4}$. This integral is given explicitly by Gradshteyn and Ryzhik (p. 131)

$$I_{2j} = \frac{(2j-1)!!}{2^j j!} \left(\frac{\pi}{2} - \xi_0 \right) - \frac{\sin \xi_0}{2^j} \left[\cos^{2j-1} \xi_0 + \sum_{q=1}^{j-1} \frac{(2j-1)(2j-3)\cdots(2j-2q+1)}{2^q(j-1)\cdots(j-q)} \cos^{2j-2q-1} \xi_0 \right]. \quad (35)$$

Hence, the coefficients f_ℓ and g_ℓ can be calculated as finite double sums. Once these are ready, the displacements at $r > r_0$ are a special case of (19)–(20).

The expressions for \vec{u}_p and \vec{u}_s are then those given in (21)–(22) with ℓ *terminating* at some even finite value.

Our second example is that of a right circular cylinder of length H and radius R . Denoting $\theta_0 = \tan^{-1}(\frac{2R}{H})$, the normal to the surface is given by $\vec{n} = f\vec{e}_r + g\vec{e}_\theta$, with

$$f = \begin{cases} \cos \theta & 0 < \theta < \theta_0 \\ \sin \theta & \theta_0 < \theta < \pi - \theta_0 \\ -\cos \theta & \pi - \theta_0 < \theta < \pi \end{cases} \quad (36)$$

$$g = \begin{cases} -\sin \theta & 0 < \theta < \theta_0 \\ \cos \theta & \theta_0 < \theta < \pi - \theta_0 \\ \sin \theta & \pi - \theta_0 < \theta < \pi \end{cases}$$

At the points $\theta = \theta_0, \pi - \theta_0$ the normal is not defined. According to (16)–(17), the coefficients f_ℓ and g_ℓ are explicitly given by the integrals:

$$f_\ell = (2\ell + 1) \left[\frac{1 + (-)^\ell}{2} \right] \left[\int_0^{\theta_0} P_\ell(\cos \theta) \sin \theta \cos \theta d\theta + \int_{\theta_0}^{\pi/2} P_\ell(\cos \theta) \sin^2 \theta d\theta \right], \quad (37)$$

$$g_\ell = \frac{2\ell + 1}{\ell(\ell + 1)} \left[\frac{1 + (-)^\ell}{2} \right] \left[\int_0^{\theta_0} P'_\ell(\cos \theta) \sin^3 \theta d\theta - \int_{\theta_0}^{\pi/2} P'_\ell(\cos \theta) \sin^2 \theta \cos \theta d\theta \right], \quad \left(' = \frac{\partial}{\partial \cos \theta} \right). \quad (38)$$

Here, again, only the even ℓ -values contribute to the sum. It is also shown in Appendix B that the first integrals in (37) and (38) can be evaluated analytically, while the remaining two can be reduced to *finite* sums of integrals of the type $I_{2j} = \int_{\xi_0}^{\pi/2} \cos^{2j} \xi d\xi$, already discussed in the previous example. Therefore, the integrals of f_ℓ and g_ℓ reduce here too to an evaluation of finite double sums (Appendix B).

4. The Long-Wave Approximation and the Corresponding Source Moment Tensor

In cases where the radius of the cavity is smaller than the radiation's wavelength such that $k_p r_0 < 1$, $k_s r_0 < 1$, we put

$$h_\ell^{(2)}(x) = \frac{1}{(2\ell+1)!!} x^\ell + i(2\ell-1)!! \left[\frac{1}{x^{\ell+1}} + \frac{1}{2(2\ell-1)} \frac{1}{x^{\ell-1}} \right] + O\left(\frac{1}{x^{\ell-3}}\right), \quad (39)$$

and deduce from (8) the suitable approximations for $\ell = 0, 2$:

$$\begin{aligned} F_{0,1}(x) &= -2ix^{-3} - x^{-2} + \dots, \\ F_{0,2}(x) &= -2x^{-2} + ix^{-1} + \dots, \\ F_{2,1} &= -12ix^{-5} - ix^{-3} + \dots, \\ F_{2,2}(x) &= 48ix^{-5} + 3ix^{-3} + \dots, \\ F_{0,3}(x) &= 2ix^{-3} - \left[\frac{i\sigma}{1-2\sigma} \right] x^{-1} + \dots, \\ F_{2,3}(x) &= 36ix^{-5} + i \left[\frac{1-5\sigma}{1-2\sigma} \right] x^{-3} + \dots, \end{aligned} \quad (40)$$

where σ is the Poisson ratio. Using these results we obtain the approximations

$$\begin{aligned} \Delta_0 &= \frac{4i}{x^2 y^3}, & \Delta_2 &= -\frac{12}{x^3 y^5} \frac{7-5\sigma}{1-\sigma}, \\ x &= k_s r_0, & y &= k_p r_0. \end{aligned} \quad (41)$$

In general, for $\ell > 0$

$$\begin{aligned} F_{\ell,1}(x) &\sim -i \left[(\ell+2) \frac{(2\ell-1)!!}{x^{\ell+3}} + \ell \frac{(2\ell-3)!!}{2x^{\ell+1}} \right] + \frac{x^{\ell-2}}{(2\ell+1)!!} (\ell-1), \\ F_{\ell,2}(x) &\sim i \left[2\ell(\ell+2) \frac{(2\ell-1)!!}{x^{\ell+3}} + (\ell^2-1) \frac{(2\ell-3)!!}{x^{\ell+1}} \right] + \frac{x^{\ell-2}}{(2\ell+1)!!} 2(\ell^2-1), \\ F_{\ell,3}(x) &\sim i \left\{ (\ell+1)(\ell+2) \frac{(2\ell-1)!!}{x^{\ell+3}} + \left[\frac{\ell(\ell-1)}{2} - \frac{\sigma(2\ell-1)}{1-2\sigma} \right] \frac{(2\ell-3)!!}{x^{\ell+1}} \right\} \\ &\quad + \frac{x^{\ell-2}}{(2\ell+1)!!} \ell(\ell-1), \end{aligned} \quad (42)$$

$$\Delta_\ell(x, y) \sim -\frac{(\ell+2)(2\ell-1)!!(2\ell-3)!!}{y^{\ell+3}x^{\ell+1}} \left[\frac{(\ell^2 + \ell + 1) - \sigma(2\ell+1)}{1-\sigma} \right]. \quad (43)$$

The corresponding values of A_ℓ and B_ℓ [Eqs. (25)–(26)] for $\ell < 3$, are

$$\begin{aligned} A_0 &= f_0 \frac{F_{0,2}(k_s r_0)}{2\Delta_0} = \frac{i}{4} f_0 (k_p r_0)^3, \\ A_2 &= f_2 \frac{F_{2,2}(k_s r_0)}{2\Delta_2} - 12g_2 \frac{F_{2,1}(k_s r_0)}{2\Delta_2} \\ &= -i(f_2 + 3g_2) \frac{1-\sigma}{7-5\sigma} \left(\frac{k_p^2}{2k_s^2} \right) (k_p r_0)^3, \\ B_2 &= \left[f_2 \frac{F_{2,1}(k_p r_0)}{\Delta_2} - g_2 \frac{F_{2,3}(k_p r_0)}{\Delta_2} \right] \frac{k_p}{k_s} \\ &= i(f_2 + 3g_2) \frac{1-\sigma}{7-5\sigma} \left(\frac{k_p}{k_s} \right) (k_s r_0)^3. \end{aligned} \quad (44)$$

When this approximation is applied to the expression of the *general* displacement field resulting from an *azimuthally-symmetric* surface [Eqs. (21)–(22)], we obtain

$$\begin{aligned} \vec{u}_p(\vec{r}; \omega) &= \frac{ip_0(\omega)}{4\mu k_p} f_0(\epsilon) (k_p r_0)^3 \vec{L}_{0,0}^-(k_p r) - \frac{ip_0(\omega)(1-\sigma)}{2\mu k_p} \sum_{\ell=2,4,\dots}^n \frac{(k_p r_0)^{\ell+1}}{(2\ell-3)!!} \\ &\quad \times \left\{ \frac{\ell[f_\ell(\epsilon) + (\ell+1)g_\ell(\epsilon)]}{(\ell^2 + \ell + 1) - \sigma(2\ell+1)} \right\} \left(\frac{k_p^2}{k_s^2} \right) \vec{L}_{0,\ell}^-(k_p r), \\ \vec{u}_s(\vec{r}; \omega) &= -\frac{ip_0(\omega)(1-\sigma)}{\mu k_s} \sum_{\ell=2,4,\dots}^n \frac{(k_s r_0)^{\ell+1}}{(2\ell-3)!!} \\ &\quad \times \left\{ \frac{f_\ell(\epsilon) + (\ell+1)g_\ell(\epsilon)}{(\ell^2 + \ell + 1) - \sigma(2\ell+1)} \right\} \vec{N}_{0\ell}^-(k_s r). \end{aligned} \quad (45)$$

For large values of ℓ , the dependence of f_ℓ and g_ℓ on ℓ can be estimated from (16)–(17): since f and g are slowly varying functions of θ relative to $P_\ell(\cos \theta)$ and $\frac{\partial}{\partial \theta} P_\ell(\cos \theta)$, respectively, it can be taken out of the integrals, leading to

$$\begin{aligned} f_\ell &\sim \ell f(\theta, \varphi; \epsilon) \int_0^\pi P_\ell(\cos \theta) \sin \theta d\theta = 2\ell f, \\ (\ell+1)g_\ell &\sim g(\theta, \varphi; \epsilon) \int_0^\pi \frac{\partial}{\partial \theta} P_\ell(\cos \theta) \sin \theta d\theta = 0 \quad (\ell \text{ even}). \end{aligned} \quad (46)$$

It is thus guaranteed that for $k_s r_0 < 1$ contributions from summands in (45) for $\ell > 2$ will have small effects on both \vec{u}_p and \vec{u}_s , *irrespective of the specific shape of the surface*.

Note that if instead of the above argument we use the asymptotic form (Magnus *et al.*, 1966)

$$P_\ell^m(\cos \theta) = (-)^m \ell^{m-1/2} \sqrt{\frac{2}{\pi \sin \theta}} \sin \left[\left(\ell + \frac{1}{2} \right) \theta + \frac{\pi}{4} (2m + 1) \right], \quad (47)$$

$$\ell \gg 1, \quad \varepsilon < \theta < \pi - \varepsilon,$$

we shall obtain $f_\ell \propto \frac{f}{\sqrt{\ell}}$, $(\ell + 1)g_\ell \propto \frac{g}{\sqrt{\ell}}$, with a faster convergence rate than in (46).

The termination of the sums in (45) at $\ell = 2$, yields the approximation

$$\begin{aligned} \vec{u}_p &= \frac{ip_0(\omega)}{\mu k_p} (k_p r_0)^3 \left[\frac{1}{4} f_0 \vec{L}_{0,0}^-(k_p r) - 2(f_2 + 3g_2) \frac{k_p^2}{k_s^2} \frac{1 - \sigma}{7 - 5\sigma} \vec{L}_{0,2}^-(k_p r) \right], \\ \vec{u}_s &= -\frac{ip_0(\omega)}{\mu k_s} (k_s r_0)^3 [f_2 + 3g_2] \frac{1 - \sigma}{5 - 7\sigma} \vec{N}_{0,2}^-(k_s r). \end{aligned} \quad (48)$$

Using the far-field approximation [(A-18)-(A-19)], (48) becomes

$$\begin{aligned} \{u_r\}_p &= \frac{ip_0(\omega)}{\mu k_p} (k_p r_0)^3 \left\{ \frac{1}{4} f_0 + 3(f_2 + 3g_2) \right. \\ &\quad \times \left. \left[\frac{v_s}{v_p} \right]^2 \frac{1 - \sigma}{7 - 5\sigma} \left(\cos^2 \theta - \frac{1}{3} \right) \right\} \frac{e^{-ik_p r}}{k_p r}, \end{aligned} \quad (49)$$

$$\{u_\theta\}_s = -\frac{i3p_0(\omega)}{2\mu k_s} (k_s r_0)^3 (f_2 + 3g_2) \frac{1 - \sigma}{7 - 5\sigma} \sin 2\theta. \quad (50)$$

It is useful to identify the displacement field in (48) with an *equivalent point force system* operating at the center of the cavity (Fig. 4). This can easily be achieved when we write down the displacement fields due to three mutually perpendicular dipoles with moments $\{M_1 = M_2, M_3\}$ in the respective x, y, z directions (Ben-Menahem and Singh, 1981, pp. 203-205):

$$\begin{aligned} \vec{u}_3 &= \frac{iM_3 k_s^2}{48\pi\mu} [\gamma_2 (2\vec{L}_{0,0} - 4\vec{L}_{0,2}) - 4\vec{N}_{0,2}], \\ \vec{u}_2 &= \frac{iM_1 k_s^2}{48\pi\mu} [\gamma_2 (2\vec{L}_{0,0} + 2\vec{L}_{0,2} + \vec{L}_{2,2}) + (2\vec{N}_{0,2} + \vec{N}_{2,2})], \\ \vec{u}_1 &= \frac{iM_1 k_s^2}{48\pi\mu} [\gamma_2 (2\vec{L}_{0,0} + 2\vec{L}_{0,2} - \vec{L}_{2,2}) + 2(\vec{N}_{0,2} - \vec{N}_{2,2})], \end{aligned} \quad (51)$$

$$\gamma_2 = 2 \left(\frac{v_s}{v_p} \right)^4.$$

The combined field $\{\vec{u}_3 + \vec{u}_2 + \vec{u}_1\}$ can be split into the following compressional and shear fields

$$\begin{aligned}\vec{u}_p(k_p r) &= \frac{1}{3}(M_3 + 2M_1) \frac{ik_s^2}{4\pi\mu} \left(\frac{v_s}{v_p}\right)^4 \vec{L}_{0,0}^-(k_p r) \\ &\quad + (M_1 - M_3) \frac{ik_s^2}{6\pi\mu} \left(\frac{v_s}{v_p}\right)^4 \vec{L}_{0,2}^-(k_p r), \\ \vec{u}_s(k_s r) &= (M_1 - M_3) \frac{ik_s^2}{12\pi\mu} \vec{N}_{0,2}^-(k_s r).\end{aligned}\quad (52)$$

A complete agreement with (48) is obtained if we set the correspondence

$$\begin{aligned}M_1 &= M_2 = \frac{3(1-\sigma)}{2} w_0 \left[\frac{f_0}{1-2\sigma} - \frac{2(f_2 + 3g_2)}{7-5\sigma} \right], \\ M_3 &= \frac{3(1-\sigma)}{2} w_0 \left[\frac{f_0}{1-2\sigma} + 4 \frac{(f_2 + 3g_2)}{7-5\sigma} \right],\end{aligned}\quad (53)$$

$$w_0 = \frac{4\pi}{3} r_0^3 p_0(\omega). \quad (54)$$

Note that

$$\delta M = M_1 - M_3 = -(f_2 + 3g_2) \frac{9(1-\sigma)}{7-5\sigma} w_0 \left. \begin{array}{l} > 0 \quad \text{line source} \\ < 0 \quad \text{disc source,} \end{array} \right\} \quad (55)$$

cannot assume arbitrary values under the physical conditions of our problem. To see this, let us examine two *limiting* cases of special interest:

(I) A *line-source* is obtained in the limit $k = 1$ for the spheroidal cavity or $\theta_0 = 0$ for the cylindrical cavity. We assume that the source energy w_0 is *fixed* such that in the limiting case $w_0 = \lim_{r_0 \rightarrow 0} \left[\frac{4\pi}{3} r_0^3 p_0 \right]$. It is then found from (32)–(33) and (37)–(38) that for *both* the spheroidal and cylindrical cavities

$$f_0 = \frac{\pi}{4}, \quad f_2 = -\frac{5\pi}{32}, \quad g_2 = -\frac{5\pi}{32}. \quad (56)$$

Equations (52)–(53) then yield the limiting values

$$\begin{aligned}M_3 &= \frac{27\pi}{368} w_0 = 0.23w_0, \quad M_1 = M_2 = \frac{297\pi}{368} w_0 = \frac{2.54}{0.81} w_0, \quad \text{for } \sigma = \frac{1}{4}, \\ M_3 &= 0, \quad M_1 = M_2 = \frac{1}{4} \pi w_0, \quad \text{for } \sigma = \frac{1}{5}.\end{aligned}\quad (57)$$

(II) A *disc-source* is obtained from the cylindrical cavity in the limit $\theta_0 = \frac{\pi}{2}$. Equations (37)–(38) then render

$$f_0 = \frac{1}{2}, \quad f_2 = \frac{5}{8}, \quad g_2 = \frac{5}{8}. \quad (58)$$

$$M_3 = \frac{567}{184}w_0 = 3.08w_0, \quad M_1 = M_2 = \frac{27}{184}w_0 = 0.15w_0, \quad \text{for } \sigma = \frac{1}{4},$$

$$M_3 = 3w_0, \quad M_1 = M_2 = 0 \quad \text{for } \sigma = \frac{1}{5}.$$

Note that (55) predicts $M_2 = M_1 = M_3$, under the condition

$$f_2 + 3g_2 = 0. \quad (59)$$

This indeed occurs for a cylindrical cavity for $\theta_0 = 50.3^\circ$ ($2R \cong 1.2H$). In this case the cylinder mimics a sphere, *with no radiated shear waves* (!), independently of the medium's Poisson's ratio [Figs. 5, 6].

Oblate cavities

As long as the observer is placed in an unbounded homogeneous and isotropic elastic medium, no distinction need be made between oblate and prolate cavity since we can always choose the z -axis to coincide with the major symmetry axis of the spheroid. This symmetry is broken once a stress-free boundary is introduced, for now it makes a great difference whether the cavity is aligned normal or parallel to the free boundary. For tunnels with axis of symmetry parallel to a free surface, the radiation patterns can be obtained by rotating the ones obtained previously by 90° relative to the fixed cartesian coordinate system that was chosen above. In the long-wave approximation this amounts to an equivalent force system of three orthogonal dipoles with moments $\{M_1, M_2 = M_3\}$. Equation (51) is then modified into

$$\begin{aligned} \vec{u}_3 &= \frac{iM_3k_s^2}{48\pi\mu} [\gamma_2(2\vec{L}_{0,0} - 4\vec{L}_{0,2}) - 4\vec{N}_{0,2}], \\ \vec{u}_2 &= \frac{iM_3k_s^2}{48\pi\mu} [\gamma_2(2\vec{L}_{0,0} + 2\vec{L}_{0,2} + \vec{L}_{2,2}) + (2\vec{N}_{0,2} + \vec{N}_{2,2})], \\ \vec{u}_1 &= \frac{iM_1k_s^2}{48\pi\mu} [\gamma_2(2\vec{L}_{0,0} + 2\vec{L}_{0,2} - \vec{L}_{2,2}) + 2(\vec{N}_{0,2} - \vec{N}_{2,2})]. \end{aligned} \quad (60)$$

In this new configuration the x -axis is aligned along the *smaller* moment M_1 , now parallel to the free surface. The combined field $\{\vec{u}_3 + \vec{u}_2 + \vec{u}_1\}$ is then expressible as

$$\begin{aligned} \vec{u}_p(k_pr) &= \frac{1}{3}(2M_3 + M_1) \frac{ik_s^2}{4\pi\mu} \left(\frac{v_s}{v_p}\right)^4 \vec{L}_{0,0}^-(k_pr) \\ &\quad - (M_3 - M_1) \frac{ik_s^2}{12\pi\mu} \left(\frac{v_s}{v_p}\right)^4 \vec{L}_{0,2}^-(k_pr) \\ &\quad + (M_3 - M_1) \frac{ik_s^2}{24\pi\mu} \left(\frac{v_s}{v_p}\right)^4 \vec{L}_{2,2}^-(k_pr), \\ \vec{u}_s(k_sr) &= \frac{ik_s^2}{24\pi\mu} (M_1 - M_3) \vec{N}_{0,2}^-(k_sr) - \frac{ik_s^2}{24\pi\mu} (M_1 - M_3) \vec{N}_{2,2}^-(k_sr). \end{aligned} \quad (61)$$

The source moment tensor

Every dipolar source can be represented by a second order symmetric cartesian tensor $\vec{\vec{M}}$ (Ben-Menahem and Singh, 1981, pp. 168-171). Its corresponding displacement field is given by the expression

$$\vec{u}(\vec{r}) = \vec{\vec{M}} : \text{grad}_0 \{ \vec{G}(\vec{r} | \vec{r}_0) \}, \quad (61a)$$

where \vec{G} is the Green's tensor of the elastic medium. We have first shown that the displacement field of a symmetrical cavity with a symmetry axis in the z -direction is equivalent to the combined fields of three *dipoles*, each along a coordinate axis, at the center of the cavity, with the respective strengths $M_{11} = M_1$, $M_{22} = M_2 = M_1$, $M_{33} = M_3$.

Thus, in the light of (53), the moment tensor of the cavity can be written in the dyadic form

$$\vec{\vec{M}} = M_1 \vec{\vec{I}} + (M_3 - M_1) \vec{e}_3 \vec{e}_3 \quad (61b)$$

where $M_1 \vec{\vec{I}}$ is known as the *isotropic part* of the tensor, and $(M_3 - M_1) \vec{e}_3 \vec{e}_3$ is the *deviatoric part*. This last part is the true signature of the non-spherical cavity which makes it distinct from both symmetrical explosions and earthquakes.

5. Surface Waves from Explosions in An Underground Cavity

Knowing the source-fields in an unbounded domain, the surface-wave fields in the presence of a stress-free planar boundary can be evaluated in a routine manner. This becomes necessary if one wishes to calculate theoretical waveforms of *Rayleigh waves* produced by explosions in underground tunnels. Since usually, the long axis of the cavity is parallel to the free surface, we must use as our *source-field* the displacement produced by an *oblate* cavity as given in Eq. (61), where we now denote it as

$$\vec{u}^{(0)} = \vec{u}_p(k_p r) + \vec{u}_s(k_s r). \quad (62)$$

It is convenient to express the l.h.s. of (61) in terms of the *cylindrical vector harmonics* via (A-1)-(A-8). It yields the source displacements and associated tractions in the form

$$\vec{u}^{(0)} = \frac{p_0(\omega)}{\mu k_p} \int_0^\infty \sum_{\ell, m} i^{m-\ell+1} \vec{u}_m^{(0)}(k) \frac{k dk}{2k_p^2}, \quad (63)$$

where

$$\vec{u}_m^{(0)} = \vec{x}_m^{(0)} \vec{P}_m + \vec{y}_m^{(0)} \vec{B}_m + \vec{z}_m^{(0)} \vec{C}_m, \quad (64)$$

$$(\ell, m) = (0, 0), (0, 2), (2, 2)$$

and

$$\left. \begin{aligned} \bar{x}_m^{(0)} &= -2\epsilon A_\ell P_\ell^m(\eta_p) e^{-\nu_p |z|} + 2B_\ell \frac{k_s}{k_p} \left(\frac{k^2 k_p^2}{k_s^3 \nu_s} \right) \frac{dP_\ell^m(\eta_s)}{i d\eta_s} e^{-\nu_s |z|} \\ \bar{y}_m^{(0)} &= 2A_\ell \left(\frac{k}{\nu_p} \right) P_\ell^m(\eta_p) e^{-\nu_p |z|} - 2\epsilon B_\ell \frac{k_s}{k_p} \left(\frac{k k_p^2}{k_s^3} \right) \frac{dP_\ell^m(\eta_s)}{i d\eta_s} e^{-\nu_s |z|} \\ \bar{z}_m^{(0)} &= 2B_\ell \frac{k_s}{k_p} \left(\frac{k_p^2}{k \nu_s} \right) P_\ell^m(\eta_s) e^{-\nu_s |z|} \end{aligned} \right\} \quad (65)$$

$$\eta_p = i\epsilon \frac{\sqrt{k^2 - k_p^2}}{k_p}, \quad \eta_s = i\epsilon \frac{\sqrt{k^2 - k_s^2}}{k_s}, \quad \epsilon = \text{sgn}(z - z_0), \quad (66)$$

with the coefficients A_ℓ and B_ℓ defined in (25)–(26).

The stress-vector (normal traction) associated with the source displacements, is

$$\begin{aligned} \vec{e}_z \cdot \vec{T}[\vec{u}^{(0)}] &= \vec{e}_z \lambda \text{div } \vec{u}^{(0)} + \mu(\nabla \vec{u}^{(0)} + \vec{u}^{(0)} \nabla), \\ &= p_0(\omega) \int_0^\infty \sum_{\ell, m} i^{m-\ell+1} \vec{T}_m^{(0)}(k) \frac{k dk}{2k_p^2}. \end{aligned} \quad (67)$$

with the dimensionless partial stress expanded as:

$$\vec{T}_m^{(0)} = \bar{X}_m^{(0)} \vec{P}_m + \bar{Y}_m^{(0)} \vec{B}_m + \bar{Z}_m^{(0)} \vec{C}_m, \quad (68)$$

$$\left. \begin{aligned} k \bar{X}_m^{(0)} &= 2 \frac{\partial \bar{x}_m^{(0)}}{\partial z} + \frac{\lambda}{\mu} \left(\frac{\partial \bar{x}_m^{(0)}}{\partial z} - k \bar{y}_m^{(0)} \right) \\ k \bar{Y}_m^{(0)} &= k \bar{x}_m^{(0)} + \frac{\partial \bar{y}_m^{(0)}}{\partial z} \\ k \bar{Z}_m^{(0)} &= \frac{\partial \bar{z}_m^{(0)}}{\partial z}. \end{aligned} \right\} \quad (69)$$

Using (65), this becomes

$$\left. \begin{aligned} \bar{X}_m^{(0)} &= 2A_\ell P_\ell^m(\eta_p) \left[\frac{2k^2 - k_x^2}{\nu_p k} \right] e^{-\nu_p |z|} \\ &\quad - 4B_\ell \left(\frac{k_s}{k_p} \right) \left[\frac{k k_p^2}{k_s^3} \right] \frac{dP_\ell^m(\eta_s)}{id\eta_s} e^{-\nu_s |z|} \\ \bar{Y}_m^{(0)} &= -4\epsilon A_\ell P_\ell^m(\eta_p) e^{-\nu_p |z|} \\ &\quad + 2B_\ell \frac{k_s}{k_p} \left[\frac{k_p^2}{k_s^3 \nu_s} (2k^2 - k_s^2) \right] \frac{dP_\ell^m(\eta_s)}{id\eta_s} e^{-\nu_s |z|} \\ \bar{Z}_m^{(0)} &= -2\epsilon B_\ell \frac{k_s}{k_p} \left[\frac{k_p}{k} \right]^2 P_\ell^m(\eta_s) e^{-\nu_s |z|}, \end{aligned} \right\} \quad (70)$$

$$(\ell, m) = (0, 0), (0, 2), (2, 2).$$

Note that in our formalism, $\{\vec{u}_m^{(0)}, \vec{T}_m^{(0)}, \bar{x}_m^{(0)}, \bar{X}_m^{(0)}\}$ are dimensionless, but $\{\vec{u}^{(0)}, \vec{T}(\vec{u}^{(0)})\}$ have the respective dimensions of displacement and stress.

We can now state our boundary value problem in terms of these source displacements and stresses and the yet undetermined corresponding entities of the half-space. Assume an expansion of latter in terms of cylindrical vector harmonics [Appendix A],

$$\begin{aligned} \vec{u}_m &= \bar{x}_m \vec{P}_m + \bar{y}_m \vec{B}_m + \bar{z}_m \vec{C}_m, \\ \vec{T}_m &= \bar{X}_m \vec{P}_m + \bar{Y}_m \vec{B}_m + \bar{Z}_m \vec{C}_m, \end{aligned} \quad (71)$$

where

$$\begin{aligned} \bar{x}_m &= a_m \nu_p e^{\nu_p z} + b_m k e^{\nu_s z}, \\ \bar{y}_m &= a_m k e^{\nu_p z} + b_m \nu_s e^{\nu_s z}, \\ \bar{z}_m &= c_m e^{\nu_s z}. \end{aligned} \quad (72)$$

Here, (a_m, b_m, c_m) are undetermined amplitude coefficients of dimensions $(length, length, 1)$ respectively

$$\begin{aligned} k \bar{X}_m &= (2k^2 - k_s^2) a_m e^{\nu_p z} + 2k \nu b_m e^{\nu_s z}, \\ k \bar{Y}_m &= 2\nu_p k a_m e^{\nu_p z} + (2k^2 - k_s^2) b_m e^{\nu_s z}, \\ k \bar{Z}_m &= \nu_s c_m e^{\nu_s z}. \end{aligned} \quad (73)$$

Again, $\{\bar{x}_m, \bar{y}_m, \bar{z}_m; \bar{X}_m, \bar{Y}_m, \bar{Z}_m\}$ are dimensionless physical entities. The total field is $\vec{u} + \vec{u}^{(0)}$. Applying the condition of a free surface at $z = h$

$$\vec{e}_z \cdot \vec{T}[\vec{u} + \vec{u}^{(0)}] = 0 \quad \text{at} \quad z = h. \quad (74)$$

we get

$$\overline{X}_m^{(0)} + \overline{X}_m = 0, \quad \overline{Y}_m^{(0)} + \overline{Y}_m = 0, \quad \overline{Z}_m^{(0)} + Z_m = 0 \quad \text{at} \quad z = h. \quad (75)$$

Solving for the coefficients $\{a_m, b_m, c_m\}$ and substituting the results in the expression for the total displacement field, we find for the field on the free surface ($\epsilon = 1, z = h$)

$$\vec{u}^{\text{total}} = \vec{u}^{(0)} + \vec{u} = \frac{p_0(\omega)}{\mu k_p} \int_0^\infty \sum_{\ell, m} i^{m-\ell+1} \vec{u}_m^{\text{total}} \frac{k dk}{2k_p^2}, \quad (76)$$

$$\vec{u}_m^{\text{total}} = U_P \hat{\vec{P}}_m + U_B \hat{\vec{B}}_m + U_C \hat{\vec{C}}_m, \quad (77)$$

$$\begin{aligned} U_C &= 4B_\ell \frac{k_s}{k_p} \left(\frac{k_p^2}{k\nu_s} \right) P_\ell^m(\eta_s) e^{-\nu_s h}, \\ U_P &= -2A_\ell P_\ell^m(\eta_p) e^{-\nu_p h} + 2B_\ell \frac{k_s}{k_p} \left[\frac{k^2 k_p^2}{k_s^3 \nu_s} \right] \frac{dP_\ell^m(\eta_s)}{id\eta_s} e^{-\nu_s h} \\ &\quad - 2A_\ell P_\ell^m(\eta_p) \frac{R_1(k)}{R(k)} e^{-\nu_p h} - 2B_\ell \frac{k_s}{k_p} \frac{dP_\ell^m(\eta_s)}{id\eta_s} \frac{k^2 k_p^2}{k_s^3 \nu_s} \frac{R_2(k)}{R(k)} e^{-\nu_s h}, \\ U_B &= 4A_\ell \left(\frac{k}{\nu_p} \right) P_\ell^m(\eta_p) e^{-\nu_p h} - 2B_\ell \frac{k_s}{k_p} \left(\frac{k k_p^2}{k_s^3} \right) \frac{dP_\ell^m(\eta_s)}{id\eta_s} e^{-\nu_s h} \\ &\quad - 2A_\ell P_\ell^m(\eta_p) \frac{R_2(k)}{R(k)} \frac{k}{\nu_p} e^{-\nu_p h} - 2B_\ell \frac{k_s}{k_p} \frac{dP_\ell^m(\eta_s)}{id\eta_s} \frac{k k_p^2}{k_s^3} \frac{R_1(k)}{R(k)} e^{-\nu_s h}, \\ (\ell, m) &= (0, 0), (0, 2), (2, 2), \end{aligned} \quad (78)$$

$$\begin{aligned} R(k) &= (2k^2 - k_s^2)^2 - 4k^2 \nu_p \nu_s, \\ R^+(k) &= (2k^2 - k_s^2)^2 + 4k^2 \nu_p \nu_s, \end{aligned} \quad (79)$$

$$R_1(k) = R^+(k) - 4k^2(2k^2 - k_s^2), \quad R_2(k) = R^+(k) - 4\nu_p \nu_s(2k^2 - k_s^2).$$

The source-terms in the expressions for U_C , U_P and U_B do not contribute to the surface-wave field and can therefore be ignored in this study. The remaining terms, which have $R(k)$ in their denominator [Eqs. (62)–(63)], contribute to the Rayleigh wave through the pole of $R(k) = 0$ in the lower complex k -plane [$\text{Re } \omega > 0$; see e.g. Ben-Menahem and Singh, pp. 263–265].

The relevant integral in (60) has the form $\int_0^\infty J_m(k\Delta) \frac{F(k)}{R(k)} dk$
 $= \frac{1}{2} \int_{-\infty}^\infty H_m^{(2)}(k\Delta) \frac{F(k)}{R(k)} dk$, where $H_m^{(2)}(k\Delta)$ are the Hankel functions of order m

of the second kind. The pole of $R(k) = 0$ is at $k_R = \gamma k_s$ where γ is a root of the equation $(2\gamma^2 - 1)^2 = 4\gamma^2 \sqrt{\gamma^2 - 1} \sqrt{\gamma^2 - \frac{v_s^2}{v_p^2}}$. For $\sigma = \frac{1}{4}$ ($\lambda = \mu$), $\gamma = \frac{v_s}{v_R} = (2 - \frac{2}{\sqrt{3}})^{-1/2} = 1.0875$.

The residue of the above integral at $k = k_R$ is given by $\{\frac{\pi i F(k_R)}{k_s^3 G(\gamma)}\} H_m^{(2)}(k_R \Delta)$ where $G = \frac{3+16\gamma^6-12\gamma^2}{6\gamma(2\gamma^2-1)^2} = 2.51220 \dots$

The terms in (62)–(64) which do not have $R(k)$ in their denominator (direct waves), do *not* contribute to the residue field and hence do not generate surface waves. Inserting in (76) all the relevant entities from Eqs. (78)–(79), using the relations $k_R = \gamma k_s$, $k_p = \frac{k_s}{\sqrt{3}}$ ($\sigma = \frac{1}{4}$), $\eta_p = i\sqrt{3\gamma^2 - 1}$, $\eta_s = i\sqrt{\gamma^2 - 1}$ and

$$\left. \begin{aligned} R_1(k_R) &= -2k_s^4(2\gamma^2 - 1), & R_2(k) &= k_s^4 \left(\frac{2\gamma^2 - 1}{\gamma} \right)^2 \\ H_m^{(2)}(k_R \Delta) &= \sqrt{\frac{2}{\pi k_R \Delta}} e^{-ik_R \Delta} e^{i(\frac{\pi m}{2} + \frac{\pi}{4})} + O(k_R \Delta)^{-3/2} \end{aligned} \right\} \quad (80)$$

the components of the spectral Rayleigh-wave displacements for $\ell < 4$ at $(z = h, \Delta, \varphi)$ which fall off with distance like $\Delta^{-1/2}$, are

$$\begin{aligned} u_z &= -\frac{6\pi p_0(\omega)}{2\mu k_p} \frac{\gamma(2\gamma^2 - 1)}{G(\gamma)} \sqrt{\frac{2}{\pi k_R \Delta}} e^{i(\frac{\pi}{4} - k_R \Delta)} \\ &\quad \times \left[s_1 e^{-hk_s \sqrt{\gamma^2 - \frac{1}{3}}} - s_2 e^{-hk_s \sqrt{\gamma^2 - 1}} \right], \\ u_\Delta &= -\frac{6\pi p_0(\omega)}{\mu k_p} \frac{\gamma \sqrt{\gamma^2 - 1}}{G} \sqrt{\frac{2}{\pi k_R \Delta}} e^{i(\frac{3\pi}{4} - k_R \Delta)} \\ &\quad \times \left[s_1 e^{-hk_s \sqrt{\gamma^2 - \frac{1}{3}}} - s_2 e^{-hk_s \sqrt{\gamma^2 - 1}} \right], \\ s_1 &= -[(2A_0 + A_2) - 9\gamma^2 A_2 \cos^2 \varphi], \\ s_2 &= -(2\gamma^2 - 1)B_2 \cos^2 \varphi. \end{aligned}$$

6. Numerical Results for Radiation Patterns of Body and Surface Waves

For the numerical calculations of radiation patterns of body waves generated by explosions in prolate spheroidal and cylindrical cavities, we used Eqs. (21) and

(22) normalized by $\frac{P_0(\omega)}{\mu k_p}$. We calculated the first five terms in the infinite series (i.e. expansion up to the 8th order in spherical harmonics). All the vector spherical harmonics $\vec{L}_{0\ell}$ and $\vec{N}_{0\ell}$ ($\ell = 0, \dots, 8$) were calculated exactly using the formulas given in Appendix A. The functions $F_{\ell,1}$, $F_{\ell,2}$, $F_{\ell,3}$ and Δ_ℓ were calculated using formulas (8). The shape-dependent coefficients f_ℓ and g_ℓ were calculated exactly using the equations (32)–(33) for prolate spheroidal cavities and (37)–(38) for cylindrical cavities. The integrals in Eqs. (32)–(33) and (37)–(38) were calculated as finite double sums, using the analysis given in Appendix B.

Spheroidal cavity

Figure 5 presents radiation patterns of body waves in the z - Δ plane for explosions in prolate spheroidal cavities (the z -axis corresponds to the axis of symmetry of the cavity). Radiation patterns were calculated for $k_p r_0 = 0.01$ (long waves), $k_p r = 100.0$ (far-field). The six parts of Figure 5 correspond to the values of the aspect ratio $\epsilon = \frac{a}{c} = 1.0$ (a sphere), 0.8, 0.668, 0.414, 0.199 and 0.0 (line source). For a spherical cavity (Fig. 5I) the radiation pattern of P-waves is symmetric and no S-waves are generated. Since in the far-field terms of order $\frac{1}{k_p r}$ are negligible, the P-patterns are those of the *radial component* of the displacement vector (23), while the S-patterns are those of collatitudinal component of the displacement vector (24).

As the shape of the cavity deviates from spherical, the P-wave radiation pattern becomes stretched in the direction perpendicular to the major (the longest) axis of the cavity. At the same time shear waves are generated.

One can see that radiation patterns are dominated by \vec{L}_{00} , \vec{L}_{02} for P-waves and \vec{N}_{02} for S-waves [the calculated coefficients of higher ($\ell > 2$) order spherical harmonics were several orders of magnitude smaller for $k_p r_0 \ll 1$]. This is consistent with the conclusions of Section 4, that the long wave radiation patterns are dominated by dipole terms. As the shape of the cavity is stretched from a sphere to a line, the vertical (along z -axis) dipole becomes smaller, and the horizontal (along x - and y -axes) dipoles become bigger. Therefore the P-wave radiation pattern becomes stretched in Δ -direction, and shear waves are generated.

Cylindrical cavity

Figure 6 presents radiation patterns of body waves in the z - Δ plane for a cylindrical cavity (the z -axis corresponds to the axis of symmetry of the cavity). Radiation patterns were calculated for $k_p r_0 = 0.01$ (long waves), $k_p r = 100.0$ (far-field). The six parts of Fig. 6 correspond to the cylinder aperture angles of $\theta_0 = 0.0$ (line source), $\frac{\pi}{8}$, $\frac{\pi}{4}$, 0.8779 (50.3°), $\frac{3\pi}{8}$ and $\frac{\pi}{2}$ (disc source). As for the previous case of the prolate spheroidal cavity, the radiation patterns are dominated by dipole terms.

For $\theta_0 = 0.8779$ (50.3°) all three dipoles M_1, M_2, M_3 have equal values [i.e. $f_2 + 3g_2 = 0$ in equations (53)].

In order to study the effects of higher order ($\ell > 2$) spherical harmonics, we calculated radiation patterns for wavelengths comparable with the size of the cavity (the radius of the equivalent sphere). Figure 7 presents radiation patterns of body waves calculated for $k_p r_0 = 1.0$, $k_p r = 10^4$. One can see that higher harmonics change only a little the radiation patterns for this wavelength [probably the strongest effect can be seen in Fig. 6IV for $\theta_0 = 0.8779$ (50.3°)]. The S-wave radiation pattern is given primarily by \vec{N}_{04} .

Higher order ($\ell > 2$) spherical harmonics play a significant role only for wavelengths much smaller than the size of the cavity ($k_p r_0 \gg 1$). However, for realistic cavity sizes (100 meters at most) this wavelength are not observed in far-field seismograms due to attenuation. Therefore we may conclude that the far-field radiation patterns of body waves generated by explosions in arbitrary cavities will be dominated by dipole terms (i.e. two-lobe radiation pattern for P-waves and 4-lobe patterns for S-waves).

This conclusion is consistent with the results of direct numerical simulations by *Stevens et al.* (1991) who presented radiation pattern for an explosion in a prolate spheroidal cavity with aspect ratio $\epsilon = 0.25$.

Figure 8 exhibits the spectral amplitude dependence of the field on the aperture of the cylindrical cavity. We note a node for S-waves at $\theta_0 \approx 50.3^\circ$, at which the P-waves pattern is spherical. The S/P energy ratio is extremal at $\theta_0 = 0$ (line source) and $\theta_0 = \frac{\pi}{2}$ (disc source), but is small over the wide plateau $\theta_0 = \frac{\pi}{5} - \frac{2\pi}{5}$.

Corner-frequencies

In order to calculate the frequency dependence of body waves amplitudes we had to make an assumption about the time dependence of the pressure pulse $P(t)$ applied at the surface of the cavity.

The most straightforward assumption is that $P(t)$ is given by the step function

$$P(t) = \begin{cases} 1 & t > 0 \\ 0 & t < 0. \end{cases} \quad (81)$$

the Fourier transform of which is given by

$$P_0(\omega) = \frac{1}{i\omega} \quad (\omega \neq 0). \quad (82)$$

We calculated amplitudes of body waves given by (21) and (22) using (82) for $\frac{r_0}{r} = 10^{-4}$.

Figure 9 presents frequency dependence of P-wave amplitude generated by the pressure pulse (81) applied at the surface of cylindrical cavity. Figure 9 corresponds to cylinders with apperture angles $\theta_0 = 0.0$ (line source), $\frac{\pi}{8}$, $\frac{\pi}{4}$, 0.8779 (50.3°), $\frac{3\pi}{8}$ and $\frac{\pi}{2}$ (disc source).

Each of the figures contains amplitude-frequency dependences for signals observed at the 5 collatitude angles $\theta = 0, \frac{\pi}{8}, \frac{\pi}{4}, \frac{3\pi}{8}$ and $\frac{\pi}{2}$. We plotted the logarithm of the amplitude versus the logarithm of the dimensionless frequency:

$$k_p r_0 = \frac{r_0 \omega}{v_p}. \quad (83)$$

All calculations are made for $\frac{r_0}{r} = 10^{-4}$.

It is clearly seen that the "corner-frequency" in all these plots corresponds to the wavelength equal to the radius of the equivalent sphere of the cavity.

Figure 10 presents the amplitude-frequency dependences of S-waves for the same situation. The plots contain amplitude-frequency dependences of signals observed at collatitude angles $\theta = \frac{\pi}{8}, \frac{\pi}{4}$ and $\frac{3\pi}{8}$ (the amplitude of S-waves radiated in the direction along and perpendicular to the axis of symmetry of the cavity is negligible in comparison to the P-wave amplitude).

For these plots we used dimensional frequency given by

$$k_s r_0 = \frac{r_0 \omega}{v_s}. \quad (84)$$

It is again obvious that the "corner-frequency" corresponds to a wavelength equal to the radius of the equivalent sphere.

We may therefore conclude that the size of the cavity wherein the explosion takes place can be deduced from the corner-frequency, *provided that there was full decoupling and that the shock wave — medium interaction occurred in the elastic regime.*

Surface waves

For numerical calculations of surface-wave radiation patterns we used the dipole approximation derived in Section 5.

Figure 11 presents radiation patterns of Rayleigh surface waves generated by explosions in cylindrical cavities with an horizontal axis of symmetry parallel to the free surface. Radiation patterns were calculated for $k_p r_0 = 0.01$ (long wave), $k_p r = 100.0$ (far-field), $k_p r = 0.0$ (shallow source), i.e. for a source at depth much smaller than the wavelength. The pattern in Fig. 11 correspond to cylindrical cavities with apperture angles $\theta_0 = 0.0$ (line source), $\frac{\pi}{8}$, $\frac{\pi}{4}$, 0.8779 (50.3°), $\frac{3\pi}{8}$ and $\frac{\pi}{2}$ (disc source).

One notices that for a source-depth much smaller than the wavelength, the Rayleigh-wave radiation patterns resemble the ones for the corresponding P-waves.

Figure 12 presents radiation patterns for the same explosions but for a "deep source" with $k_p r = 1.0$. At this depth, the radiation patterns change considerably relative to the corresponding ones at $h = 0$, due to the amplitude decay with depth.

Corner frequencies for surface waves

Figure 13 presents amplitude-frequency dependences of Rayleigh surface waves generated by pressure pulse (81) applied at the surface of cylindrical cavities with horizontal axes of symmetry. The amplitude-frequency dependences are calculated for $k_p h = 0.0$ (shallow source), $\frac{r_0}{r} = 10^{-4}$ and plotted against dimensionless frequency.

The various patterns in Fig. 13 correspond to cavities with aperture angles $\theta_0 = 0.0$ (line source), $\frac{\pi}{8}$, $\frac{\pi}{4}$, 0.8779 (50.3°), $\frac{3\pi}{8}$ and $\frac{\pi}{2}$ (disc source). The five curves at each figure correspond to the signal observed at the 5 azimuthal angles $\varphi = 0, \frac{\pi}{8}, \frac{\pi}{4}, \frac{3\pi}{8}$ and $\frac{\pi}{2}$.

The left side of all the amplitude-frequency dependences have a slope of $\frac{1}{2}$ (compare with the same curves for body waves for which the left hand side is horizontal). This is because the surface waves decay at $\frac{1}{(k_p r)^{1/2}}$ rather than $\frac{1}{k_p r}$ (body waves), which brings in an extra factor of $\omega^{1/2}$.

For a "shallow source" the "corner-frequency" corresponds to a wavelength that is approximately equal to the radius of the equivalent sphere.

Figure 14 presents the same amplitude-frequency dependences but for a "deep source" with $k_p h = 1.0$. One can see that the amplitude-frequency dependences are mainly controlled by the exponential terms $e^{-k_p h}$ and $e^{-k_s h}$.

7. Discussion

The radiation of seismic body and surface waves from explosions in underground tunnels has been calculated in the far-field of the elastic zone. The following assumptions and approximations were made:

- The reflected *body-wave* field from the free surface was ignored; only direct P and S signals were considered. Since these waves are truly diagnostic of the source, it is perhaps preferred to isolate the direct field from the data and compare the Fourier transformed P and S waveforms with our theoretical model.

- Conversion of body-waves to Rayleigh waves and vice versa was ignored.
- Our theory is valid only for wavelengths which are much larger than the dimensions of the cavity. Shorter wavelengths are assumed to be absorbed and not present in the data.

It is clear from Figs. 5, 6 and 7 that the radiation pattern for P-waves is always *dipolar*, i.e. it can be represented by a single equivalent dipole with at most two lobes and one nodal line. The S-wave, on the other hand, is *quadrupolar*, which is the result of two perpendicular dipoles.

We know, however, that most earthquakes have quadrupolar P-wave patterns (Frohlich, 1994) which arise from the double-couple nature of its equivalent force-system. Thus, for the sake of comparison with (61a), the moment tensor of a standard earthquake has the dyadic form

$$\begin{aligned}\vec{M} &= M_0(\vec{e}_1\vec{e}_1 - \vec{e}_2\vec{e}_2) \\ &= M_0\vec{I} - M_0(2\vec{e}_2\vec{e}_2 + \vec{e}_3\vec{e}_3).\end{aligned}\tag{85}$$

By removing the isotropic part from (61a) and (85), one can examine the deviatoric part of the cavity explosion to see whether it conforms to a standard earthquake source. Obviously the two deviatoric parts are worlds apart because of the extra term $\{-2M_0\vec{e}_2\vec{e}_2\}$. Thus, the explosion will look very strongly like a *'non double couple earthquake'*. This can, and should, serve as a definite test for a suspicious clandestine explosion.

Stump *et al.* (1994) analyzed the near-source seismograms recorded from the Coalora nuclear explosion (Yucca Flats, Nevada Test Site, February 11, 1983). They showed that the source moment tensor had an isotropic part 5 to 10 times greater than the deviatoric part, which according to their analysis was mostly due to spall. We suggest that the data inversion scheme used by the above authors can be applied to signals arising from underground explosions in order to determine the influence of the shape of the cavity upon the deviatoric component of the source's moment tensor.

The theory is valid for a homogeneous elastic medium. However, known algorithms for multilayered media can be applied to our *source fields*, to generalize the results for multilayered media that takes into account such phenomena as dispersion, attenuation and scattering. The fast convergence of our computational scheme will not be affected by this generalization, since this convergence depends only on the shape of the cavity and not on the properties of the elastic medium.

On the other hand, the propagation of the source fields through a vertically heterogeneous media will generate SH and Love waves, the analysis of which may render additional information on the shape of the cavity and the spectrum of the initial pulse. Indeed, Love waves and Lg signals were observed from underground decoupled nuclear explosions.

The present paper does not address directly the problem of *seismic decoupling*, namely, the dependence of the signals spectra upon the shape and strength of the initial pressure pulse, and the dependence of the *seismic yield* on the shape of the cavity and the rock-mechanical properties in the neighborhood of the cavities boundary.

The main thrust of the present paper was concentrated on the extension of Sharpe's naive model to non-spherical cavities. The subject of decoupling and its implication to monitoring of small nuclear explosions in underground cavities will be treated in a sequel paper in this Journal.

Acknowledgements

This research was supported by the Air-Force Office of Scientific Research under Grant No. F49620-93-1-0424DEF. We thank Dr. D.G. Harkrider for helpful discussions and for pointing to us a number of algebraic errors.

We also thank our reviewer, Dr. J. Freeman Gilbert, for drawing our attention to certain consequences of the analysis which escaped our notice, thus enhancing the promulgation of our results. One of us (AMB) is grateful to Dr. M.N. Toksöz, Director of ERL for enabling him to visit M.I.T., where this study was conducted.

References

- Abo-Zena, A.M., 1977. Radiation from a finite cylindrical explosive source. *Geophys.* **42**, 1384-1393.
- Adushkin, V.V., I.O. Kitov, O.P. Kuznetsov and D.D. Sultanov, 1993. *Geophys. Res. Lett.* **20**, 1695-1698.
- Ben-Menahem, A. and A. Cisternas, 1963. The dynamic response of an elastic half-space to an explosion in a spherical cavity. *J. Math. Phys.* **42**, 112-125.
- Ben-Menahem, A. and S.J. Singh, 1981. *Seismic Waves and Sources*, Springer-Verlag, 1108 pp.
- Florence, A.L., S.A. Miller and C.E. Keller, 1993. Underground explosions by rubble-field cavities. *J. Geophys. Res.* **98**, 14197-14209.
- Frohlich, C., 1994. Earthquakes with non-double couple mechanisms. *Science* **264**, 804-809.
- Gelfand, I.M., R.A. Minlos and Z.Y. Shapiro, 1963. *Representations of the Rotation and Lorentz Groups and Their Applications*, Pergamon, New York.
- Glenn, L.A., 1993. Energy-density effects on seismic decoupling. *J. Geophys. Res.* **98**, 1933-1942.
- Glenn, L.A., A.J.C. Ladd, B. Moran and K.A. Wilson, 1985. Elastic radiation from explosively loaded ellipsoidal cavities in an unbounded medium. *Geophys. J.* **81**, 231-241.
- Gradshteyn, I.S. and I.M. Ryzhik, 1980. *Tables of Integrals, Series and Products*. Academic Press, New York, 1086 pp.
- Gregory, R.D., 1967. An expansion theorem applicable to problems of wave propagation in an elastic half-space containing a cavity. *Proc. Camb. Phil. Soc.* **63**, 1341-1367.
- Haskell, N.A., 1961. A static theory of the seismic coupling of a contained underground explosion, *J. Geophys. Res.* **66**, 2937-2944.
- Haskell, N.A., 1967. Analytic approximation for the elastic radiation from a contained underground explosion. *J. Geophys. Res.* **72**, 2583-2587.
- Hazebroek, P., 1966. Elastic waves from a finite line source. *Proc. Roy. Soc. Lond.* **294A**, 38-65.
- Heelan, P.A., 1953. Radiation from a cylindrical source of finite length. *Geophys.* **18**, 685-696.
- Herbst, R.F. *et al.*, 1961. Use of large cavities to reduce seismic waves from underground explosions, *J. Geophys. Res.* **66**, 959-978.

- Johnson, L.R., 1988. Source characteristics of two underground nuclear explosions, *Geophys. J.* **95**, 15-30.
- King, D.S., B.E. Freeman, D.D. Eilers and J.D. Johnson, 1989. The effective yield of a nuclear explosion in a small cavity in geologic material: enhanced coupling revisited. *J. Geophys. Res.* **94**, 12375-12385.
- Latter, A.L. *et al.*, 1959. Seismic scaling law for underground explosions. *The Phys. of Fluids* **2**, 280-282.
- Latter, A.L. *et al.*, 1961. A method of concealing underground nuclear explosions. *J. Geophys. Res.* **66**, 943-946.
- Latter, A.L. *et al.*, 1961. The effect of plasticity on decoupling of underground explosions, *J. Geophys. Res.* **66**, 2929-2936.
- Lewis, H.W. and S.B. Treiman, 1966. Seismic signals from nuclear explosions in overdriven cavities. *J. Geophys. Res.* **71**, 2029-2035.
- Love, A.E.H., 1944. *A Treatise on the Mathematical Theory of Elasticity*. Dover, New York.
- Magnus, W., F. Oberhettinger and R.P. Soni, 1966. *Special Functions of Mathematical Physics*, 3rd edition. Springer-Verlag, New York. 508 pp.
- Moon, P. and D.E. Spencer, 1971. *Field Theory Handbook*. Springer-Verlag, Berlin, 236 pp.
- Patterson, D.W., 1966. Nuclear decoupling, full and partial. *J. Geophys. Res.* **71**, 3427-3436.
- Rawson, D. *et al.*, 1966. Post-explosion environment resulting from the Salmon event, 1966. *J. Geophys. Res.* **71**, 3507-3521.
- Rial, J.A. and B. Moran, 1986. Radiation patterns for explosively-loaded axisymmetric cavities in an infinite elastic medium: analytic approximations and numerical results. *Geophys. J.* **85**, 855-862.
- Rogers, L.A., 1966. Free-field motion near a nuclear explosion in salt: Project Salmon. *J. Geophys. Res.* **71**, 3415-3426.
- Sharpe, J.A., 1942. The production of elastic waves by explosion pressure. I. Theory and empirical field observations. *Geophys.* **7**, 144-154.
- Singh, S.J. and A. Ben-Menahem, 1988. Seismic waves from non-double-couple sources. *Phys. Earth Planet. Int.* **50**, 272-279.
- Springer, D.L., 1966. Calculation of first-zone P-wave amplitudes for Salmon event and for decoupled sources. *J. Geophys. Res.* **71**, 3459-3467.
- Springer, D.L. *et al.*, 1968. The Sterling experiment: decoupling of seismic waves by a shot-generated cavity. *J. Geophys. Res.* **73**, 5995-6011.

- Stump, B.W., R.E. Reinke, K.H. Olsen and L.R. Johnson. 1994. Isotropic and deviatoric characterization of the Coalora nuclear explosion in Yucca Flats. *Geophys. J. Int.* **116**, 538-552.
- Stevens, J.L., J.M. Murphy and N. Rimer, 1991. Seismic source characteristic of cavity decoupled explosion in salt and tuff. *Bull. Seism. Soc. Am.* **81**, 1272-1291.
- Stevens, J.L. *et al.*, 1991. Simulation of seismic signals from partially coupled nuclear explosions in spherical and ellipsoidal cavities. Maxwell, S-Cubed Division Final Report SSS-FR-91-12735, P.O. Box 1620, La Jolla, CA 92038-1620.
- Taylor, S., H.J. Patton and P.G. Richards (Eds.), 1991. *Explosion Source Phenomenology*, American Geophysical Union, Geophysical Monograph **65**, 268 pp.
- Thiruvengkatachar, V.R. and K. Viswanathan, 1965. Dynamic response of an elastic half-space to time-dependent surface tractions over an embedded spherical cavity. *Proc. Roy. Soc. Lond.* **287**, 549-567.
- Toksöz, M.N., A. Ben-Menahem and D.G. Harkrider, 1964. Determination of source parameters by amplitude equalization of seismic surface waves: 1. Underground nuclear explosion. *J. Geophys. Res.* **69**, 4355-4366.
- Usami, T., 1958. Elastic waves generated from an oblate spheroidal cavity whose wall is subjected to normal stress of harmonic type. *Geophys. Mag.* **29**, 11-36.
- Usami, T. and T. Hirono, 1956. Elastic waves generated from an prolate spheroidal cavity whose wall is subjected to normal stresses of harmonic type. *Papers in Meteorol. Geophys.* **7**, 288-321.
- Varatharajulu (Varadan), V. and Y.-H. Pao, 1976. Scattering matrix for elastic waves. I. Theory. *J. Acoust. Soc. Am.* **60**, 556-566.
- Werth, G. and P. Randolph, 1966. The Salmon seismic experiment. *J. Geophys. Res.* **71**, 3405-3413.
- Zhao, L.-S. and D.G. Harkrider, 1992. Wave fields from an off-center explosion in an embedded solid sphere. *Bull. Seism. Soc. Am.* **82**, 1927-1955.

Legend of Figures

- Fig. 1 The geometry of explosion in cavities: (I) spherical cavity in an unbounded solid; (II) prolate spheroidal cavity and its 'equivalent sphere'; (III) oblate spheroidal cavity in a half-space with a free surface ($z = h$).
- Fig. 2 Major axis cross-section of a prolate spheroidal cavity $r(\theta) = \frac{a}{\sqrt{1-k \cos^2 \theta}}$, $k = 1 - (\frac{a}{c})^2$. The equi-volume condition renders $r_0 = a^{2/3} c^{1/3}$ for the equivalent sphere.
- Fig. 3 Cylindrical cavity of radius R and height H . The parameter $\theta_0 = tg^{-1}(\frac{2R}{H})$ controls the radiation-pattern of the source.
- Fig. 4 Simulation of cavities by a combination of three mutually orthogonal dipoles: (a) vertical cavity with $M_1 = M_2 > M_3$; (b) horizontal cavity with $M_3 = M_2 > M_1$.
- Fig. 5 Radiation patterns of body waves displacements generated by explosions in prolate spheroidal cavities with different aspect ratio $\epsilon = \frac{a}{c}$ (Fig. 2). Patterns are drawn in a vertical symmetry plane embedding the z -axis, with the collatitude angle θ increasing from zero ($z = 0$) clockwise: (I) $\epsilon = 1.0$ (sphere); (II) $\epsilon = 0.8$; (III) $\epsilon = 0.668$; (IV) $\epsilon = 0.414$; (V) $\epsilon = 0.199$; (VI) $\epsilon = 0.0$ (line source). Solid line — P-waves (radial, u_r); dashed line — S-waves (collatitudinal, u_θ). $k_p r_0 = 0.01$ (long wave); $k_p r = 100.0$ (far-field); $\sigma = \frac{1}{4}$.
- Fig. 6 Radiation patterns of body waves generated by explosions in cylindrical cavities with different aperture angles θ_0 : (I) $\theta_0 = 0.0$ (line source); (II) $\theta_0 = \frac{\pi}{8}$; (III) $\theta_0 = \frac{\pi}{4}$; (IV) $\theta_0 = 0.8779$; (V) $\theta_0 = \frac{3\pi}{8}$; (VI) $\theta_0 = \frac{\pi}{2}$ (disc source). Solid line — P-waves; dashed line — S-waves. $k_p r_0 = 0.01$ (long wave); $k_p r = 100.0$ (far-field); $\sigma = \frac{1}{4}$.
- Fig. 7 Radiation patterns of body waves generated by explosions in cylindrical cavities with different aperture angles: (I) $\theta_0 = 0.0$ (line source); (II) $\theta_0 = \frac{\pi}{8}$; (III) $\theta_0 = \frac{\pi}{4}$; (IV) $\theta_0 = 0.8779$; (V) $\theta_0 = \frac{3\pi}{8}$; (VI) $\theta_0 = \frac{\pi}{2}$ (disc source). Solid line — P-waves; dashed line — S-waves. $k_p r_0 = 1.0$; $k_p r = 10^4$; $\sigma = \frac{1}{4}$.
- Fig. 8 Dependence of the body wave amplitude on the aperture angle θ_0 for a cylindrical cavity. Observation angles: ——— 0° ; - - - $\frac{\pi}{8}$; - - - - $\frac{\pi}{4}$; $\frac{3\pi}{8}$; ····· $\frac{\pi}{2}$. (I) $|\vec{u}_p|$ versus $2\theta_0/\pi$; (II) $|\vec{u}_s|$ versus $2\theta_0/\pi$; (III) $\frac{|\vec{u}_s|^2}{|\vec{u}_p|^2}$ versus $2\theta_0/\pi$. Note the nodal point (N) at which the P-radiation patterns are spherical (no S-motion).
- Fig. 9 Amplitude ($\ln |\vec{u}_p|$) frequency ($\ln[k_p r_0]$) dependences of P-waves gener-

ated by a pressure-step applied at the surface of a finite cylindrical cavity observed at different collatitude angles: — $\theta = 0$; --- $\theta = \frac{\pi}{8}$; - - - - $\theta = \frac{\pi}{4}$; $\theta = \frac{3\pi}{8}$; ····· $\theta = \frac{\pi}{2}$. Aperture angles of cylindrical cavities assume the values: (I) $\theta_0 = 0$ (line source); (II) $\theta_0 = \frac{\pi}{8}$; (III) $\theta_0 = \frac{\pi}{4}$; (IV) $\theta_0 = 0.8779$; (V) $\theta_0 = \frac{3\pi}{8}$; (VI) $\theta_0 = \frac{\pi}{2}$ (disc source). $\frac{r_0}{r} = 10^{-4}$; $\sigma = \frac{1}{4}$. Note the corner-frequency at $k_p r_0 = 1$.

Fig. 10 Same as 8, but for S-waves. Observation angles are: --- $\theta = \frac{\pi}{8}$; - - - - $\theta = \frac{\pi}{4}$; $\theta = \frac{3\pi}{8}$.

Fig. 11 Azimuthal radiation patterns of the vertical Rayleigh surface wave displacement generated by explosions in cylindrical cavities with different aperture angles: (I) $\theta_0 = 0$ (line source); (II) $\theta_0 = \frac{\pi}{8}$; (III) $\theta_0 = \frac{\pi}{4}$; (IV) $\theta_0 = 0.8779$; (V) $\theta_0 = \frac{3\pi}{8}$; (VI) $\theta_0 = \frac{\pi}{2}$ (disc source). The z -axis of the cavity (Fig. 3) is parallel to the free surface. Note that the pattern of body waves and surface waves from the horizontally cylindrical cavity are both in the *same horizontal plane*, and therefore can be compared.

Fig. 12 Same as 10 but for a deep source ($k_p h = 1.0$).

Fig. 13 Amplitude ($\ln |u_z|$) frequency ($\ln[k_p r_0]$) dependences of Rayleigh surface waves generated by a pressure step applied at the surface of cylindrical cavity, observed at different azimuthal angles: — $\varphi = 0$; --- $\varphi = \frac{\pi}{8}$; - - - - $\varphi = \frac{\pi}{4}$; $\varphi = \frac{3\pi}{8}$; ····· $\varphi = \frac{\pi}{2}$. Aperture angles of cylindrical cavities are: (I) $\theta_0 = 0$ (line source); (II) $\theta_0 = \frac{\pi}{8}$; (III) $\theta_0 = \frac{\pi}{4}$; (IV) $\theta_0 = 0.8779$; (V) $\theta_0 = \frac{3\pi}{8}$; (VI) $\theta_0 = \frac{\pi}{2}$ (disc source). $\frac{r_0}{r} = 10^{-4}$; $\sigma = \frac{1}{4}$; $k_p h = 0.0$ (shallow source). Note the *corner-frequency* at $k_p r_0 = 1$.

Fig. 14 Same as 12 but for deep source $k_p h = 1.0$.

Appendix A: Fundamental Elastodynamic Vectors, Associated Functions and Coordinate Transformation Relations

The Hansen *elastodynamic eigenvectors* in spherical coordinates (r, θ, φ) with unit vectors $(\vec{e}_r, \vec{e}_\theta, \vec{e}_\varphi)$ are:

$$\begin{aligned}\vec{L}_{m\ell}^\pm &= \vec{P}_{m\ell} z_\ell'^\pm(k_p r) + \sqrt{\ell(\ell+1)} \vec{B}_{m\ell} \frac{z_\ell^\pm(k_p r)}{k_p r}, & k_p &= \frac{\omega}{v_p}, \\ \vec{N}_{m\ell}^\pm &= \vec{P}_{m\ell} \ell(\ell+1) \frac{z_\ell^\pm(k_s r)}{k_s r} + \sqrt{\ell(\ell+1)} \vec{B}_{m\ell} \left[\frac{z_\ell^\pm(k_s r)}{k_s r} + z_\ell'^\pm(k_s r) \right], & k_s &= \frac{\omega}{v_s}, \\ \vec{M}_{m\ell}^\pm &= \sqrt{\ell(\ell+1)} \vec{C}_{m\ell} z_\ell^\pm(k_s r).\end{aligned}\quad (A-1)$$

The *spherical vector harmonics* are:

$$\begin{aligned}\vec{P}_{m\ell} &= \vec{e}_r P_\ell^m(\cos \theta) e^{im\varphi}, \\ \sqrt{\ell(\ell+1)} \vec{B}_{m\ell} &= \left(\vec{e}_\theta \frac{\partial}{\partial \theta} + \vec{e}_\varphi \frac{1}{\sin \theta} \frac{\partial}{\partial \varphi} \right) P_\ell^m(\cos \theta) e^{im\varphi}, \\ \sqrt{\ell(\ell+1)} \vec{C}_{m\ell} &= \left(\vec{e}_\theta \frac{1}{\sin \theta} \frac{\partial}{\partial \varphi} - \vec{e}_\varphi \frac{\partial}{\partial \theta} \right) P_\ell^m(\cos \theta) e^{im\varphi}.\end{aligned}\quad (A-2)$$

In (A-1)-(A-2), $z_\ell^+(x) = j_\ell(x)$, spherical Bessel function of the first kind and $z_\ell^-(x) = h_\ell^{(2)}(x)$, spherical Bessel function of the second kind. $P_\ell^m(\cos \theta)$ is the associated Legendre polynomial of degree ℓ and order m . A prime ($'$) denotes differentiation w.r.t. the argument, and $k_i = k_p$ or k_s .

In circular cylindrical coordinates (Δ, φ, z) with unit-vectors $\{\vec{e}_\Delta, \vec{e}_\varphi, \vec{e}_z\}$, the Hansen vectors assume the form:

$$\begin{aligned}\vec{L}_m^\pm &= \frac{1}{k_p} (\pm \nu_p \vec{P}_m + k \vec{B}_m) e^{\pm \nu_p z}, \\ \vec{N}_m^\pm &= \frac{1}{k} (k \vec{P}_m \pm \nu_s \vec{B}_m) e^{\pm \nu_s z}, \\ \vec{M}_m^\pm &= \vec{C}_m e^{\pm \nu_s z}.\end{aligned}\quad (A-3)$$

where

$$\nu_p = \sqrt{k^2 - k_p^2}, \quad \nu_s = \sqrt{k^2 - k_s^2}, \quad Y_m(k\Delta, \varphi) = J_m(k\Delta) e^{im\varphi},$$

$$\begin{aligned}\vec{P}_m(k\Delta, \varphi) &= \vec{e}_z Y_m(k\Delta, \varphi), & m &= 0, 1, 2, \dots, \\ \vec{B}_m(k\Delta, \varphi) &= \left(\vec{e}_\Delta \frac{\partial}{\partial k\Delta} + \vec{e}_\varphi \frac{1}{k\Delta} \frac{\partial}{\partial \varphi} \right) Y_m(k\Delta, \varphi), \\ \vec{C}_m(k\Delta, \varphi) &= \left(\vec{e}_\Delta \frac{1}{k\Delta} \frac{\partial}{\partial \varphi} - \vec{e}_\varphi \frac{\partial}{\partial k\Delta} \right) Y_m(k\Delta, \varphi).\end{aligned}\quad (A-4)$$

We shall need the results,

$$\operatorname{div} \vec{P}_m = 0, \quad \vec{e}_z \operatorname{div} \vec{B}_m = -k \vec{P}_m, \quad \operatorname{div} \vec{C}_m = 0, \quad (A-5)$$

$$\begin{aligned} \vec{e}_z \cdot (\nabla \vec{P}_m + \vec{P}_m \nabla) &= k \vec{B}_m, \\ \vec{e}_z \cdot (\nabla \vec{B}_m + \vec{B}_m \nabla) &= 0, \\ \vec{e}_z \cdot (\nabla \vec{C}_m + \vec{C}_m \nabla) &= 0. \end{aligned} \quad (A-6)$$

Transformation of spherical to cylindrical eigenvectors was treated by *Ben-Menahem and Singh* (1981, p. 78). It is shown there that the exterior Hansen vectors in spherical and cylindrical coordinates are linked through the integral relations,

$$\begin{aligned} \vec{L}_{m\ell}^-(k_p r) &= \frac{1}{k_p} i^{m-\ell+1} \int_0^\infty \vec{L}_m^{(0)}(k_p \Delta) P_\ell^m(\eta_p) \frac{k dk}{\sqrt{k^2 - k_p^2}}, \\ \vec{N}_{m\ell}^-(k_s r) &= -\frac{1}{k_s^2} i^{m-\ell} \int_0^\infty \vec{N}_m^{(0)}(k_s \Delta) \left[\frac{dP_\ell^m(\eta_s)}{d\eta_s} \right] \frac{k^2 dk}{\sqrt{k^2 - k_s^2}} \\ &\quad - i^{m-\ell+1} \int_0^\infty \vec{M}_m^{(0)}(k_s \Delta) P_\ell^m(\eta_s) \frac{dk}{\sqrt{k^2 - k_s^2}}, \\ \vec{M}_{m\ell}^-(k_s r) &= -\frac{1}{k_s^2} i^{m-\ell} \int_0^\infty \vec{M}_m^{(0)}(k_s \Delta) \left[\frac{dP_\ell^m(\eta_s)}{d\eta_s} \right] \frac{k^2 dk}{\sqrt{k^2 - k_s^2}} \\ &\quad - i^{m-\ell+1} \int_0^\infty \vec{N}_m^{(0)}(k_s \Delta) P_\ell^m(\eta_s) \frac{dk}{\sqrt{k^2 - k_s^2}}. \end{aligned} \quad (A-7)$$

Here

$$\epsilon = \operatorname{sgn}(z - z_0), \quad \eta_p = i\epsilon \frac{\sqrt{k^2 - k_p^2}}{k_p}, \quad \eta_s = i\epsilon \frac{\sqrt{k^2 - k_s^2}}{k_s},$$

$$\begin{aligned} \vec{L}_m^{(0)}(k_p \Delta) &= \frac{1}{k_p} (-\epsilon \nu_p \vec{P}_m + k \vec{B}_m) e^{-\nu_p |z|}, \\ \vec{N}_m^{(0)}(k_s \Delta) &= \frac{1}{k_s} (k \vec{P}_m - \epsilon \nu_s \vec{B}_m) e^{-\nu_s |z|}, \\ \vec{M}_m^{(0)}(k_s \Delta) &= \vec{C}_m e^{-\nu_s |z|}, \end{aligned} \quad (A-8)$$

$$\nu_p = \sqrt{k^2 - k_p^2}, \quad \nu_s = \sqrt{k^2 - k_s^2}.$$

The vectors $\vec{M}_m^{(0)}, \vec{N}_m^{(0)}$ are obtained from $\vec{M}_m^{(0)}, \vec{N}_m^{(0)}$ on replacing $Y_m(k\Delta, \varphi)$ in the expressions for \vec{P}_m etc. in (A-4) by $\frac{\partial}{\partial \varphi} Y_m(k\Delta, \varphi)$. Relations (A-7) are also valid when $Y_{m\ell}(\theta, \varphi)$ in $\vec{L}_{m\ell}^-$, etc., is replaced by $Y_{m\ell}^{c,s}(\theta, \varphi)$ and $Y_m(k\Delta, \varphi)$ in $\vec{L}_m^{(0)}$, etc., is replaced by $Y_m^{c,s}(k\Delta, \varphi)$. In (A-7), P_ℓ^m is the Legendre associated polynomial.

By definition

$$Y_{m\ell}^{c,s}(\theta, \varphi) = P_\ell^m(\cos \theta)(\cos m\varphi, \sin m\varphi).$$

The associated vector harmonics are denoted $\vec{P}_{m\ell}^{c,s}$ etc. The same applies to cylindrical coordinates.

The recursion relations needed for our computations are:

$$\begin{aligned} z_{\ell+1}(x) &= \frac{2\ell+1}{x} z_\ell(x) - z_{\ell-1}(x), \\ P_{\ell+1}(\cos \theta) &= \frac{2\ell+1}{\ell+1} \cos \theta P_\ell(\cos \theta) - \frac{\ell}{\ell+1} P_{\ell-1}(\cos \theta), \\ \frac{\partial P_{\ell+1}(\cos \theta)}{\partial \theta} &= \frac{\partial P_{\ell-1}(\cos \theta)}{\partial \theta} - (2\ell+1)(\sin \theta P_\ell(\cos \theta)). \end{aligned} \quad (A-9)$$

The participating scalar eigenfunctions are,

$$\begin{aligned} x j_0(x) &= \sin x, \\ x^2 j_1(x) &= \sin x - x \cos x, \\ x^3 j_2(x) &= (3 - x^2) \sin x - 3x \cos x, \\ x^4 j_3(x) &= (15 - 6x^2) \sin x + (x^3 - 15x) \cos x, \\ x^5 j_4(x) &= (105 - 45x^2 + x^4) \sin x + (10x^3 - 105x) \cos x, \\ x^6 j_5(x) &= (945 - 420x^2 + 15x^4) \sin x + (-x^5 + 105x^3 - 945x) \cos x, \\ x^7 j_6(x) &= (10,395 - 4725x^2 + 210x^4 - x^6) \sin x \\ &\quad + (-21x^5 + 1260x^3 - 10,395x) \cos x, \\ x^8 j_7(x) &= (135,135 - 62,370x^2 + 3150x^4 - 28x^6) \sin x \\ &\quad + (x^7 - 378x^5 + 17,325x^3 - 135,135x) \cos x, \\ x^9 j_8(x) &= (2,027,025 - 945,945x^2 + 51,975x^4 - 630x^6 + x^8) \sin x \\ &\quad + (36x^7 - 6930x^5 + 270,270x^3 - 2,027,025x) \cos x, \end{aligned} \quad (A-10)$$

$$\begin{aligned}
x e^{ix} h_0^{(2)}(x) &= i, \\
x^2 e^{ix} h_1^{(2)}(x) &= -x + i, \\
x^3 e^{ix} h_2^{(2)}(x) &= -3x + i(3 - x^2), \\
x^4 e^{ix} h_3^{(2)}(x) &= (-15x + x^3) + i(15 - 6x^2), \\
x^5 e^{ix} h_4^{(2)}(x) &= (-105x + 10x^3) + i(105 - 45x^2 + x^4), \\
x^6 e^{ix} h_5^{(2)}(x) &= (-x^5 + 105x^3 - 945x) + i(945 - 420x^2 + 15x^4), \\
x^7 e^{ix} h_6^{(2)}(x) &= (-21x^5 + 1260x^3 - 10,395x) \\
&\quad + i(10,395 - 4725x^2 + 210x^4 - x^6), \\
x^8 e^{ix} h_7^{(2)}(x) &= (x^7 - 378x^5 + 17,325x^3 - 135,135x) \\
&\quad + i(135,135 - 62,370x^2 + 3150x^4 - 28x^6), \\
x^9 e^{ix} h_8^{(2)}(x) &= (36x^7 - 6930x^5 + 270,270x^3 - 2,027,025x) \\
&\quad + i(2,027,025 - 945,945x^2 + 41,975x^4 \\
&\quad - 630x^6 + x^8),
\end{aligned} \tag{A-11}$$

$$\begin{aligned}
P_0(\cos \theta) &= 1, \\
P_1(\cos \theta) &= \cos \theta, \\
P_2(\cos \theta) &= \frac{3}{2} \cos^2 \theta - \frac{1}{2}, \\
P_3(\cos \theta) &= \frac{5}{2} \cos^3 \theta - \frac{3}{2} \cos \theta, \\
P_4(\cos \theta) &= \frac{35}{8} \cos^4 \theta - \frac{30}{8} \cos^2 \theta + \frac{3}{8}, \\
P_5(\cos \theta) &= \frac{63}{8} \cos^5 \theta - \frac{70}{8} \cos^3 \theta + \frac{15}{8} \cos \theta, \\
P_6(\cos \theta) &= \frac{231}{16} \cos^6 \theta - \frac{315}{16} \cos^4 \theta + \frac{105}{16} \cos^2 \theta - \frac{5}{16}, \\
P_7(\cos \theta) &= \frac{429}{16} \cos^7 \theta - \frac{693}{16} \cos^5 \theta + \frac{315}{16} \cos^3 \theta - \frac{35}{16} \cos \theta, \\
P_8(\cos \theta) &= \frac{6435}{128} \cos^8 \theta - \frac{12,012}{128} \cos^6 \theta + \frac{6930}{128} \cos^4 \theta \\
&\quad - \frac{1260}{128} \cos^2 \theta + \frac{35}{128}.
\end{aligned} \tag{A-12}$$

Note that

$$x^{\ell+1} e^{ix} h_\ell^{(2)}(x) = a_\ell(x) + i b_\ell(x), \tag{A-13}$$

where $a_\ell(x)$ are *polynomials* obeying the recursion relation

$$a_{\ell+1}(x) = (2\ell + 1)a_\ell(x) - x^2 a_{\ell-1}(x), \tag{A-14}$$

subjected to the initial conditions $a_0(x) = 0$, $a_1(x) = -x$. The polynomials $b_\ell(x)$

obey the same relation, but with the initial conditions $b_0(x) = 1$, $b_1(x) = 1$. Also

$$a_\ell(x) + ib_\ell(x) = \sum_{k=0}^{\ell} 2^{-k} \left[\frac{(\ell+k)!}{k!(\ell-k)!} \right] (ix)^{\ell+1-k}. \quad (A-15)$$

Similarly, if we put in (A-7)

$$x^{\ell+1} j_\ell(x) = \bar{a}_\ell \sin x + \bar{b}_\ell \cos x, \quad (A-16)$$

we find that $\{\bar{a}, \bar{b}\}$ obey (A-14) subjected to the initial conditions

$$\bar{a}_0 = 1, \quad \bar{a}_1 = 1; \quad \bar{b}_0 = 0, \quad \bar{b}_1 = -x. \quad (A-17)$$

In the *far-field* we may assume $k_p r \gg 1$, $k_s r \gg 1$. Consequently, the spherical Hankel functions appearing in (58) may be approximated by

$$\begin{aligned} h_\ell^{(2)}(x) &\cong \frac{i^{\ell+1}}{x} e^{-ix} + O\left(\frac{1}{x^2}\right), \\ \frac{h_\ell^{(2)}(x)}{x} &\cong \frac{i^{\ell+1}}{x^2} e^{-ix} + O\left(\frac{1}{x^3}\right), \\ h_\ell^{(2)'}(x) &\cong \frac{i^\ell}{x} e^{-ix} + O\left(\frac{1}{x^2}\right). \end{aligned} \quad (A-18)$$

Hence

$$\begin{aligned} \tilde{L}_{0,0}(k_p r) &\cong \left[\frac{e^{-ik_p r}}{k_p r} \right] \tilde{e}_r, \\ \tilde{L}_{0,2}(k_p r) &\cong \left[-\frac{e^{-ik_p r}}{k_p r} \right] \left[\frac{3 \cos^2 \theta - 1}{2} \right] \tilde{e}_r, \\ \tilde{N}_{0,2}(k_s r) &\cong \frac{3}{2} \left[\frac{e^{-ik_s r}}{k_s r} \right] \sin 2\theta \tilde{e}_\theta. \end{aligned} \quad (A-19)$$

Appendix B: Quadrature of the 'Cavity Integrals'

We wish to evaluate the non-zero spheroidal cavity coefficients for $\ell = 2n$, $k = 1 - \epsilon^2$, $\eta = 1 - \epsilon^4$

$$f_{2n} = \frac{4n+1}{2} \int_0^\pi \frac{1 - k \cos^2 \theta}{\sqrt{1 - \eta \cos^2 \theta}} P_{2n}(\cos \theta) \sin \theta d\theta, \quad (B-1)$$

$$g_{2n} = \frac{-(4n+1)}{2n(2n+1)} \int_0^\pi \frac{k \sin \theta \cos \theta}{\sqrt{1 - \eta \cos^2 \theta}} P'_{2n}(\cos \theta) \sin^2 \theta d\theta. \quad (B-2)$$

Inserting the expansion

$$P_{2n}(\cos \theta) = \sum_{j=0}^n c_{2n,2j} \cos^{2j} \theta, \quad (B-3)$$

where $c_{2n,2j}$ is the $2j^{th}$ coefficient of the $2n^{th}$ Legendre polynomial, we have

$$f_{2n} = (4n+1) \sum_{j=0}^n c_{2n,2j} \left\{ \int_0^{\pi/2} \frac{\cos^{2j} \theta}{\sqrt{1 - \eta \cos^2 \theta}} \sin \theta d\theta - k \int_0^{\pi/2} \frac{\cos^{2j+2} \theta}{\sqrt{1 - \eta \cos^2 \theta}} \sin \theta d\theta \right\}, \quad (B-4)$$

$$g_{2n} = \frac{-(4n+1)}{n(2n+1)} k \sum_{j=1}^n j c_{2n,2j} \left\{ \int_0^{\pi/2} \frac{\cos^{2j} \theta}{\sqrt{1 - \eta \cos^2 \theta}} \sin \theta d\theta - \int_0^{\pi/2} \frac{\cos^{2j+2} \theta}{\sqrt{1 - \eta \cos^2 \theta}} \sin \theta d\theta \right\}. \quad (B-5)$$

It is thus necessary to evaluate only a single integral-type for both coefficients. It is readily shown that

$$\int_0^{\pi/2} \frac{\cos^{2j} \theta}{\sqrt{1 - \eta \cos^2 \theta}} \sin \theta d\theta = \eta^{-j-1/2} \int_{\xi_0}^{\pi/2} \cos^{2j} \xi d\xi, \quad (B-6)$$

where $\cos \xi_0 = \sqrt{\eta}$ and $\int_{\xi_0}^{\pi/2} \cos^{2j} \xi d\xi$ is given in ³⁵(27). Therefore,

$$f_{2n} = (4n+1) \sum_{j=0}^n c_{2n,2j} \{ \eta^{-j-1/2} I_{2j}(\xi_0) - k \eta^{-j-3/2} I_{2j+2}(\xi_0) \}, \quad (B-7)$$

$$g_{2n} = \frac{-(4n+1)}{n(2n+1)} k \sum_{j=0}^n j c_{2n,2j} \{ \eta^{-j-1/2} I_{2j}(\xi_0) - \eta^{-j-3/2} I_{2j+2}(\xi_0) \}. \quad (B-8)$$

The evaluation of the corresponding integrals (37)–(38) for the circular cylinder cavity proceeds along the same lines. Here we need, in addition, the exact results (Magnus *et al.*, 1966)

$$\int_0^{\theta_0} \cos \theta P_{2n}(\cos \theta) \sin \theta d\theta = \frac{1}{(2n-1)(2n+2)} [-\sin^2 \theta_0 P_{2n}(\cos \theta_0) + \sin^2 \theta_0 \cos \theta_0 P'_{2n}(\cos \theta_0)], \quad (B-9)$$

$$\int_0^{\theta_0} \sin^2 \theta P'_{2n}(\cos \theta) \sin \theta d\theta = -\sin^2 \theta_0 P_{2n}(\cos \theta_0) - \frac{2}{(2n-1)(2n+2)} \times [\sin^2 \theta_0 P_{2n}(\cos \theta_0) - \cos \theta_0 \sin^2 \theta_0 P'_{2n}(\cos \theta_0)], \quad (B-10)$$

$$\left(' = \frac{\partial}{\partial \cos \theta} \right).$$

The remaining integrals in (37)–(38) can again be expressed in terms of I_{2j} . Altogether we find

$$f_{2n} = (4n+1) \left[\frac{-1}{(2n-1)(2n+2)} \{ \sin^2 \theta_0 P_{2n}(\cos \theta_0) - \sin^2 \theta_0 \cos \theta_0 P'_{2n}(\cos \theta_0) \} - \sum_{j=0}^n c_{2n,2j} \{ I_{2j+2}(\theta_0) - I_{2j}(\theta_0) \} \right], \quad (B-11)$$

$$g_{2n} = \frac{4n+1}{2n(2n+1)} \left[-\sin^2 \theta_0 P_{2n}(\cos \theta_0) - \frac{2}{(2n-1)(2n+2)} \{ \sin^2 \theta_0 P_{2n}(\cos \theta_0) - \cos \theta_0 \sin^2 \theta_0 P'_{2n}(\cos \theta_0) \} + \sum_{j=1}^n 2j c_{2n,2j} \{ I_{2j+2}(\theta_0) - I_{2j}(\theta_0) \} \right]. \quad (B-12)$$

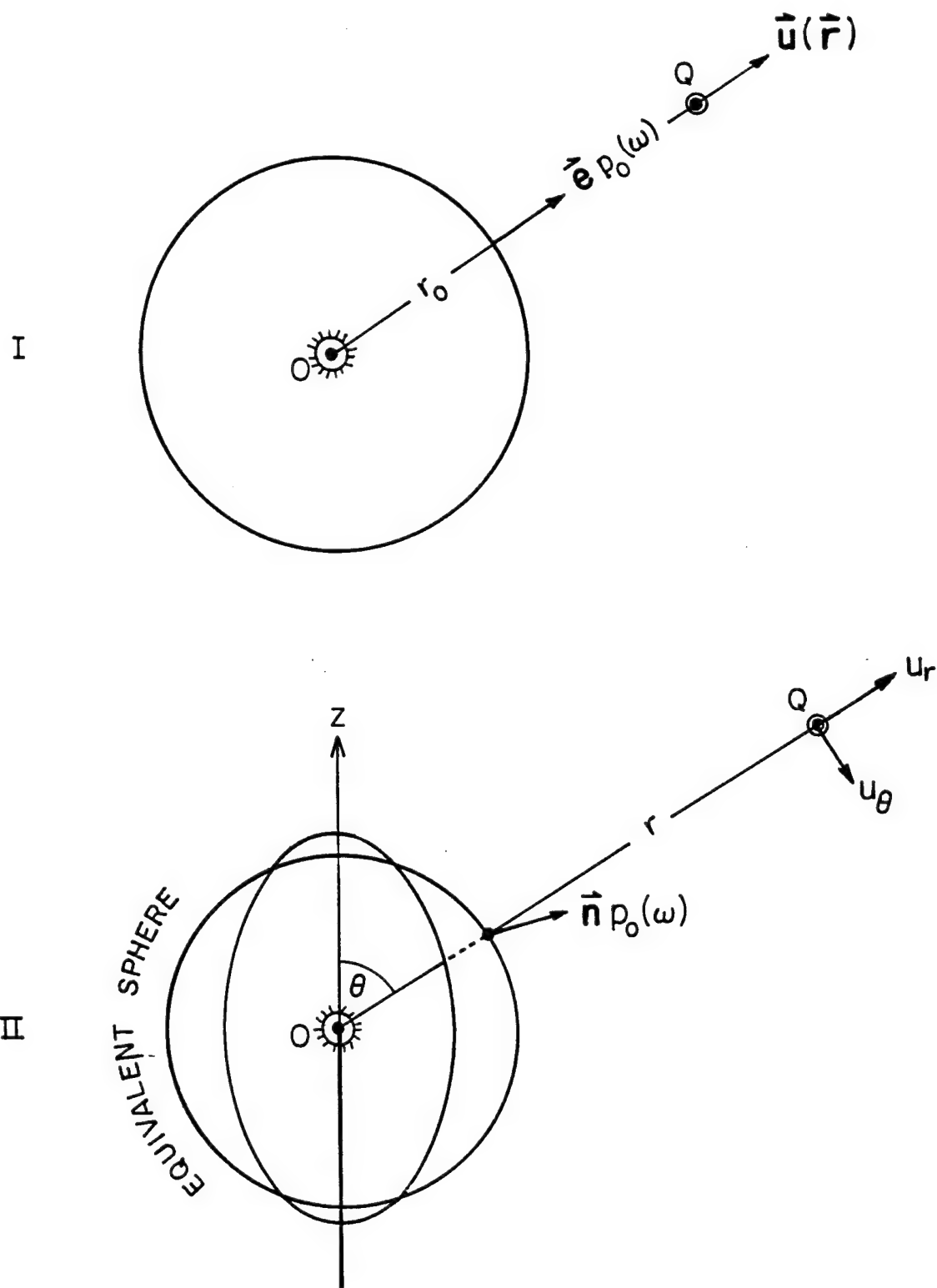


Fig. 1

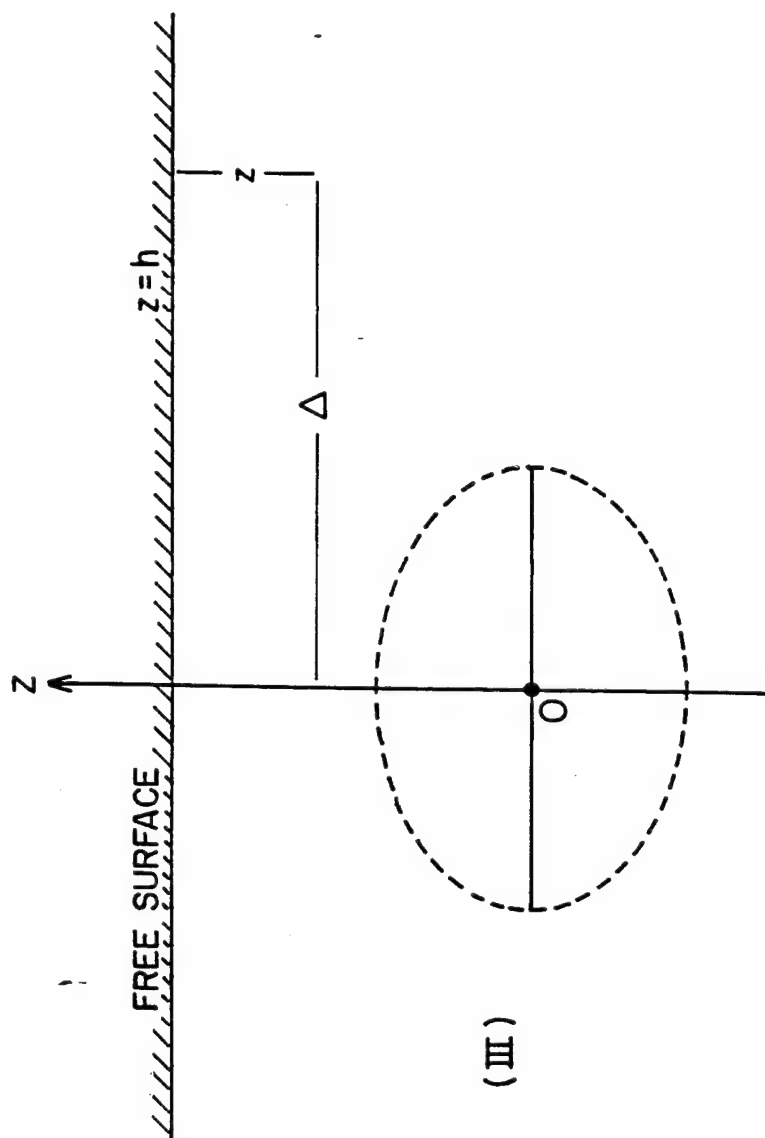


Fig. 1

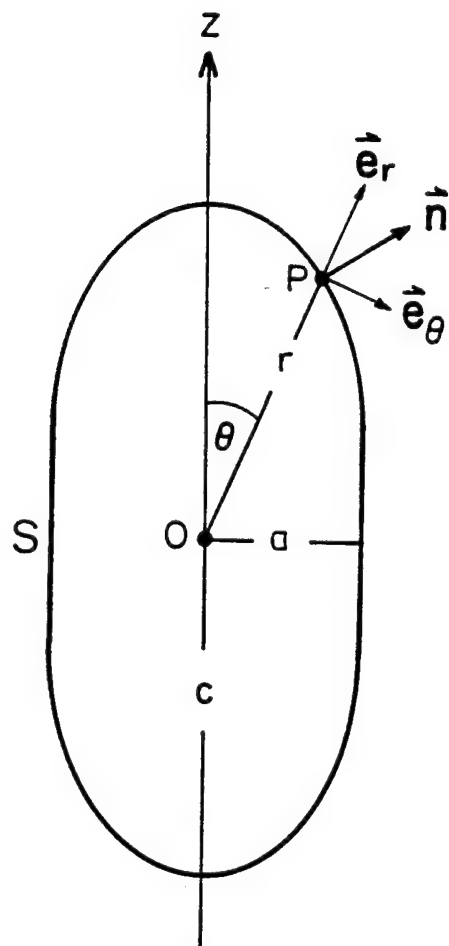


Fig. 2

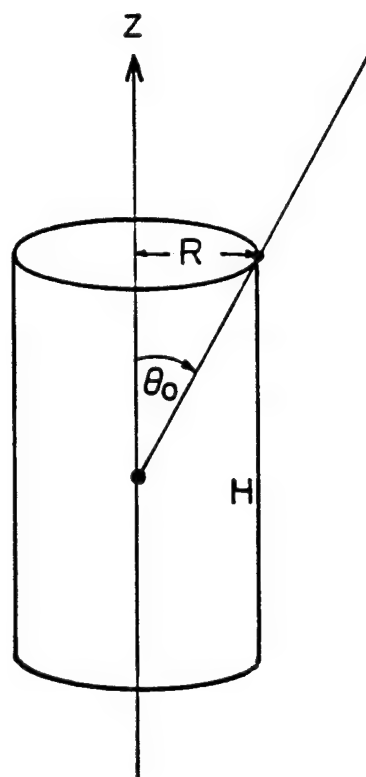


Fig. 3

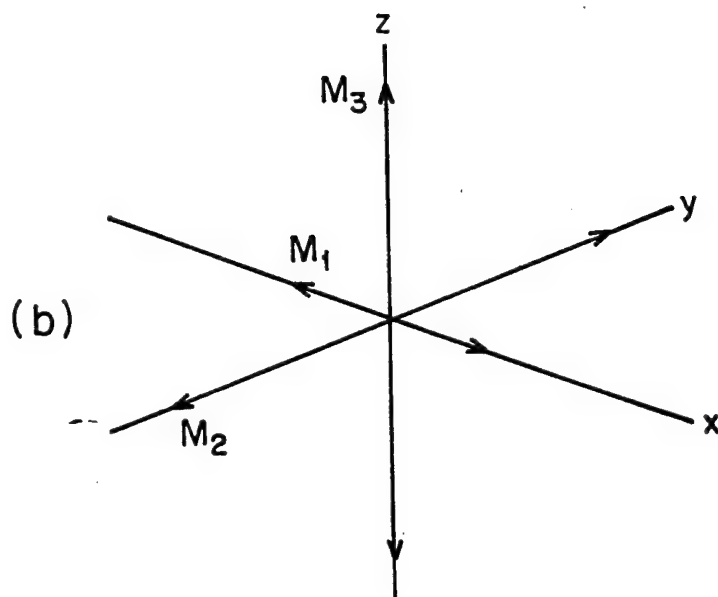
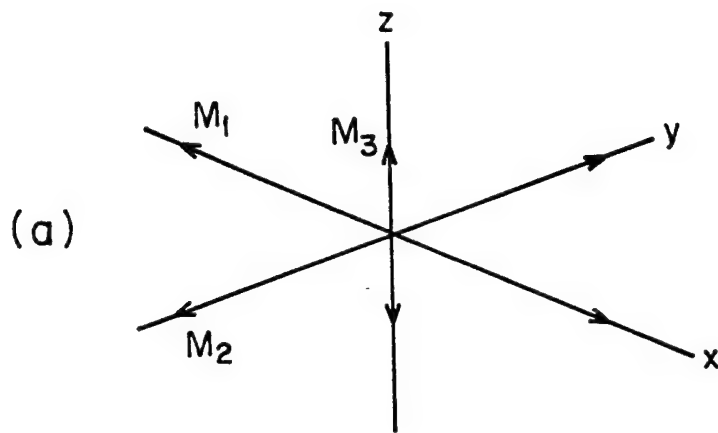


Fig. 4

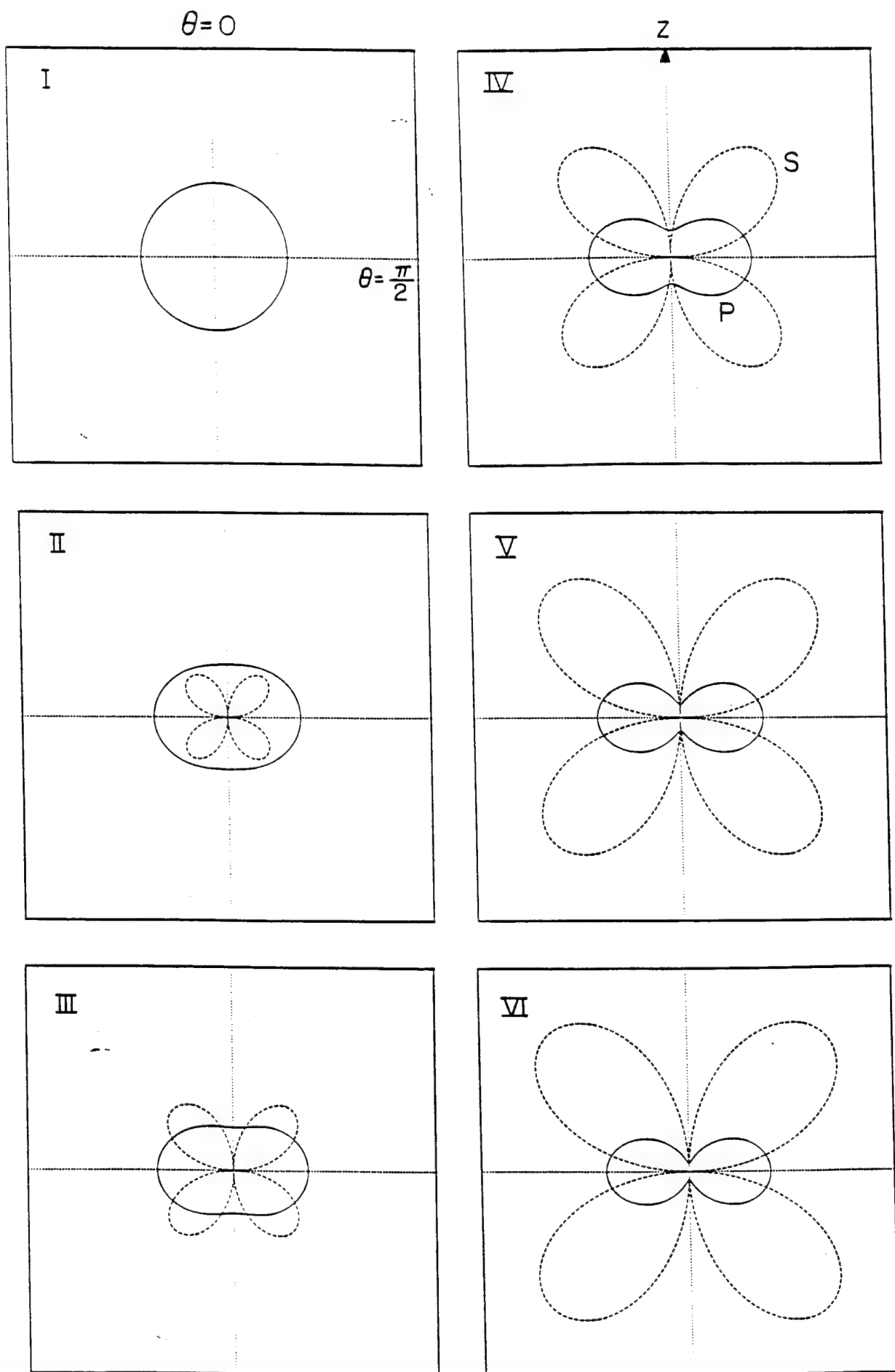


Fig. 5
-93-

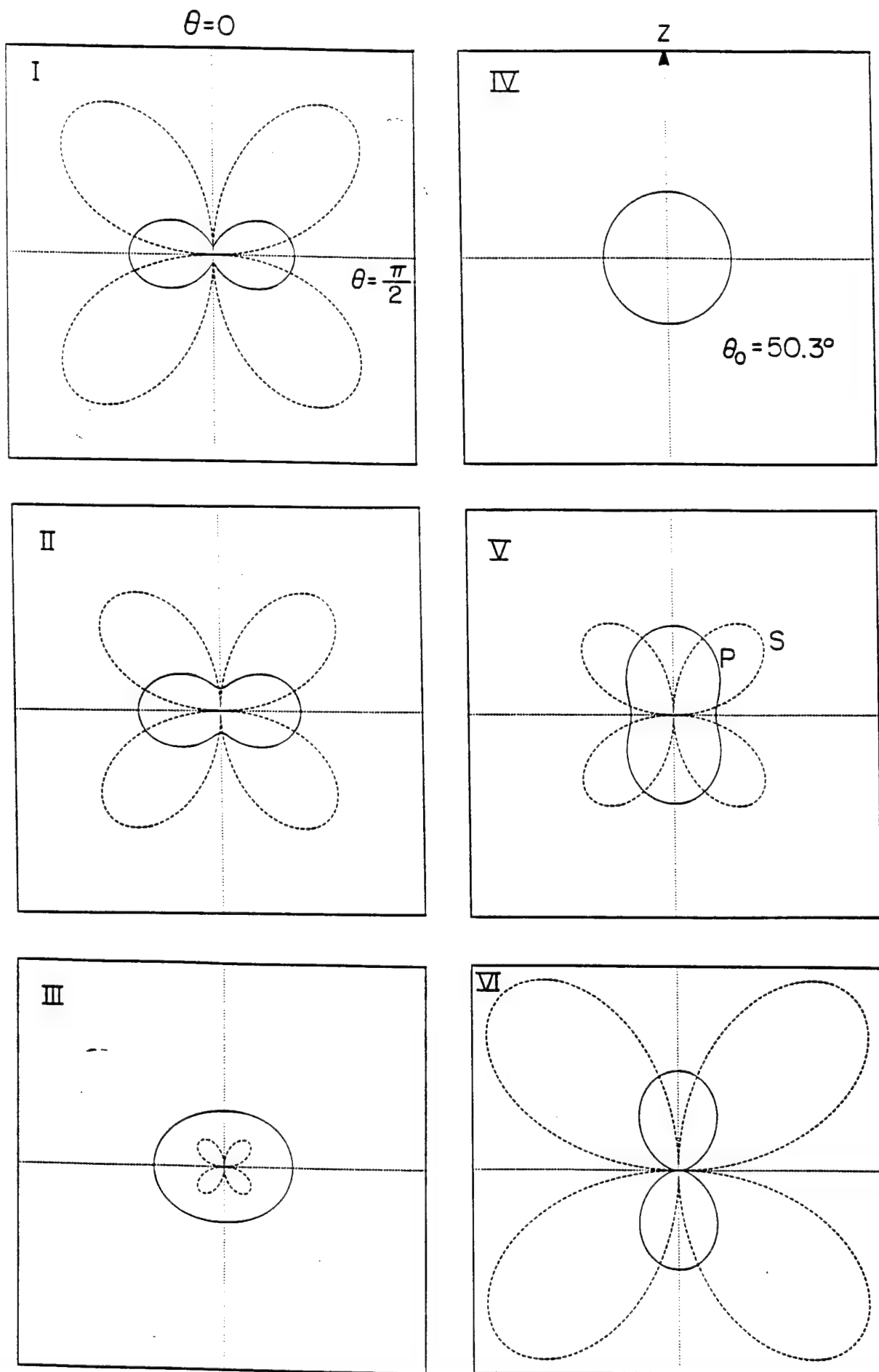


Fig. 6

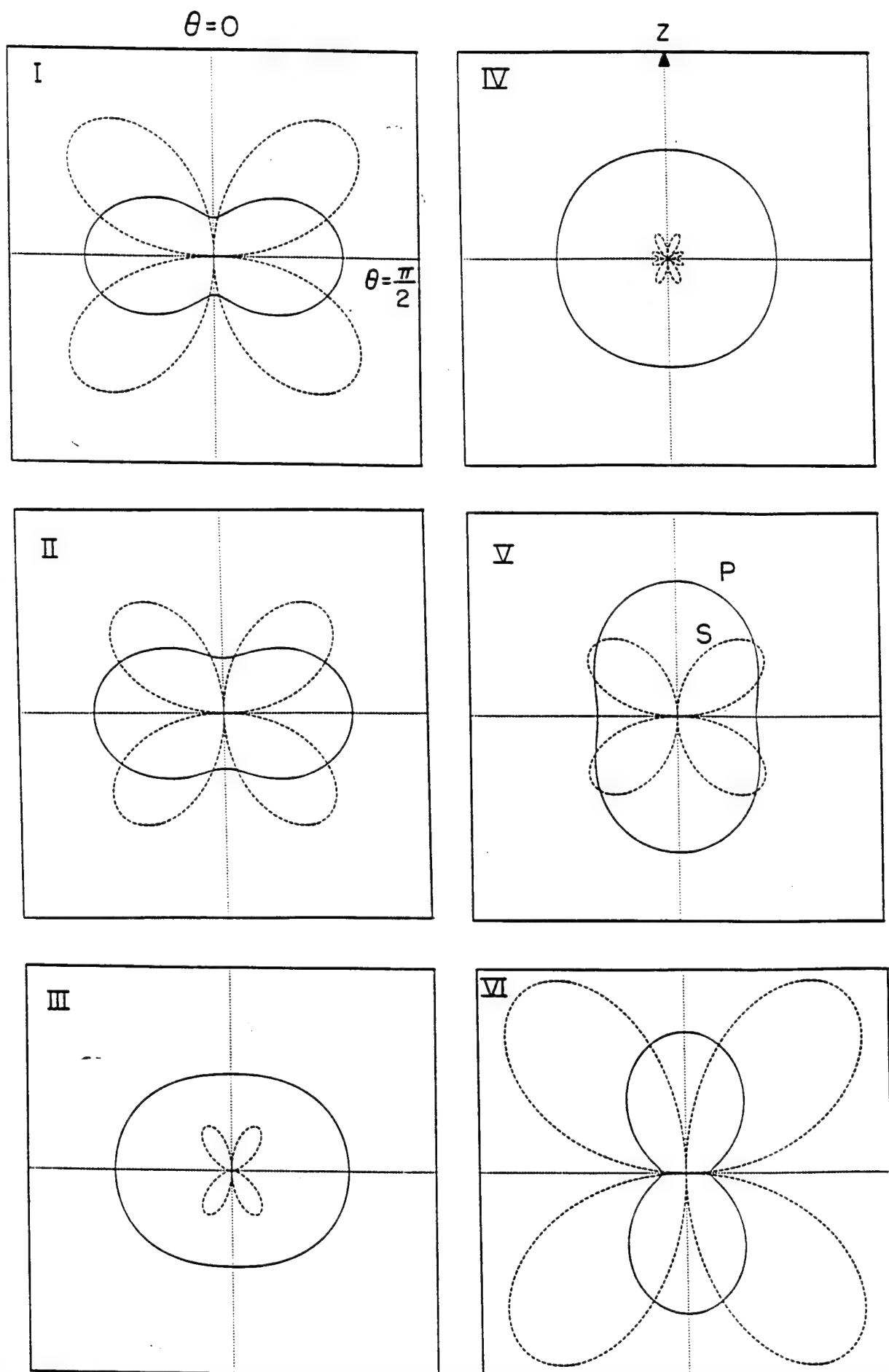


Fig. 7
-95-

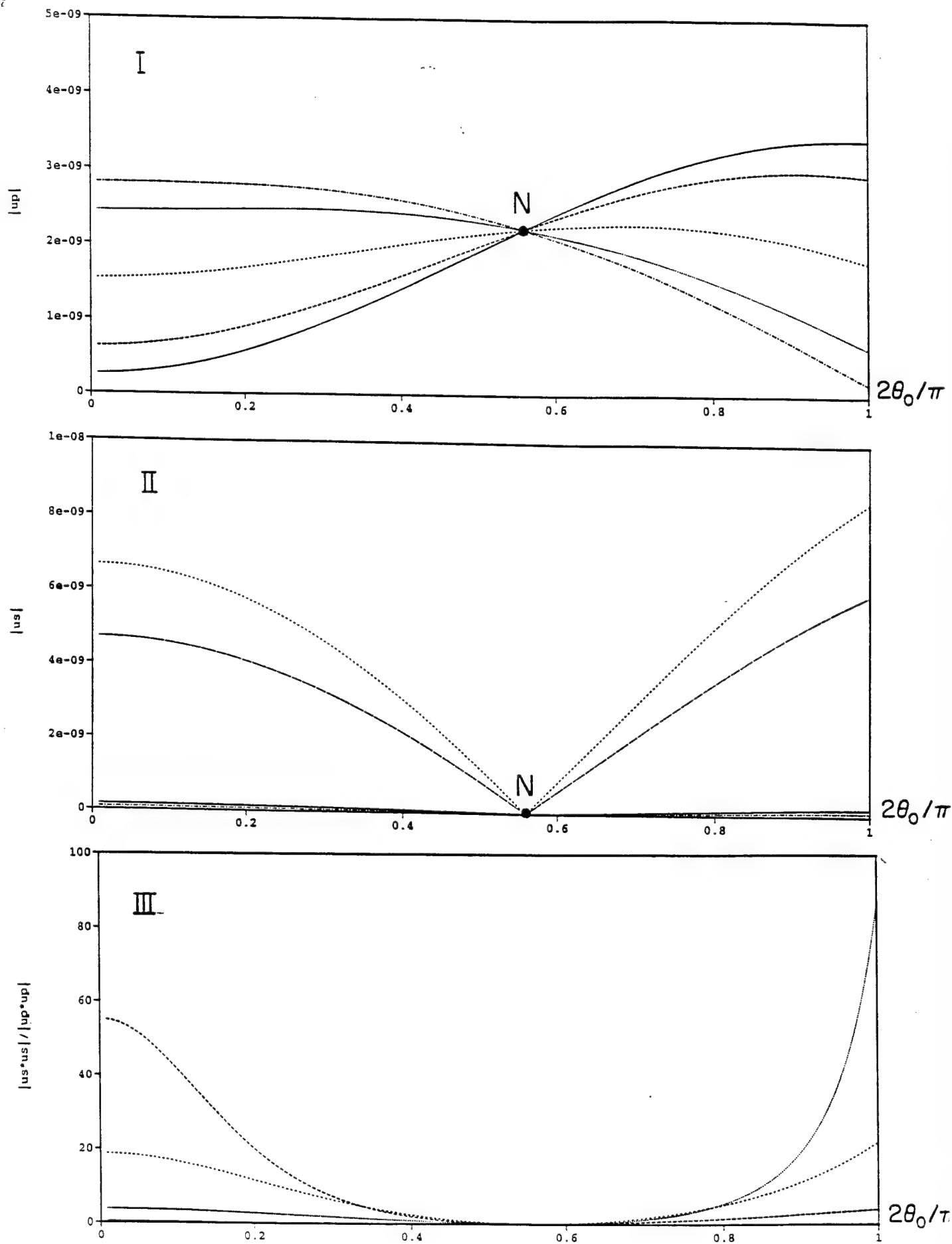


Fig. 8

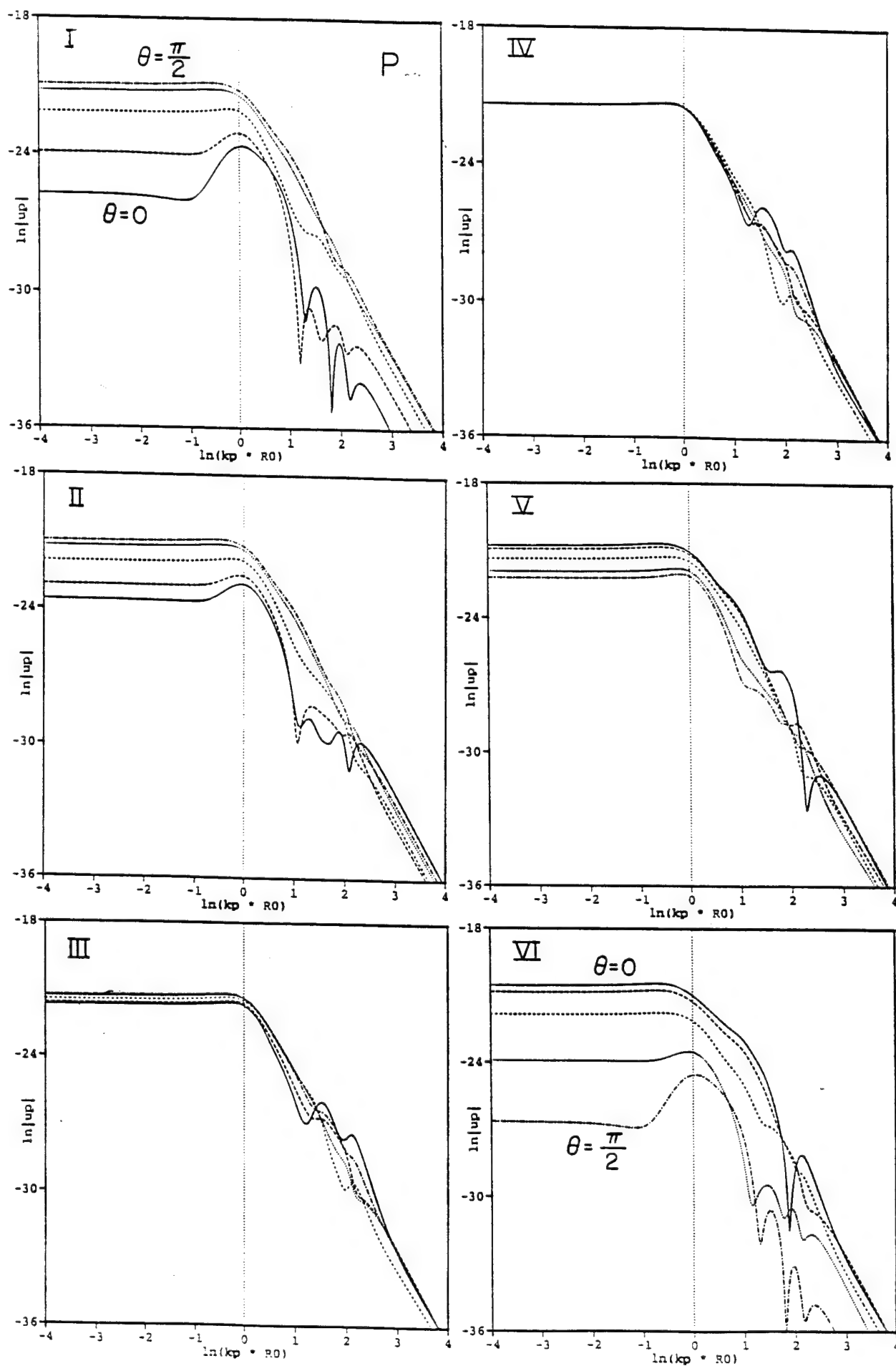


Fig. 9

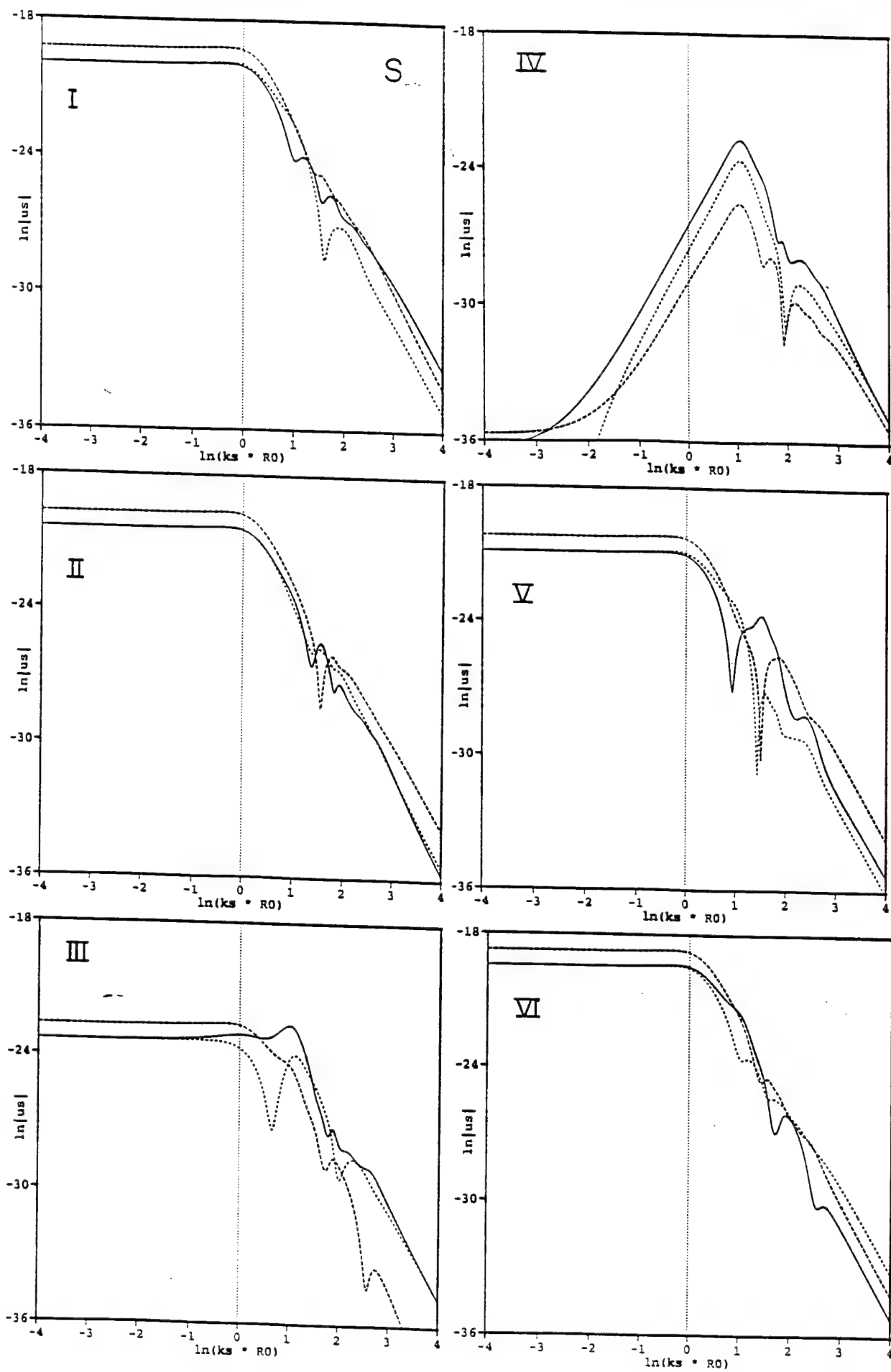


Fig. 10

$$\varphi=0$$

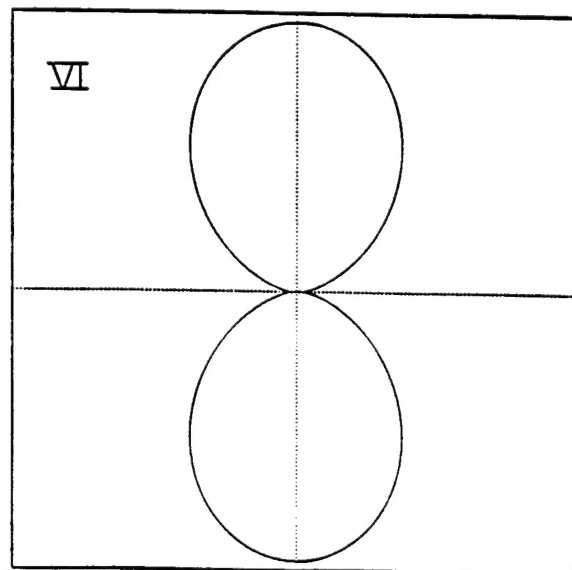
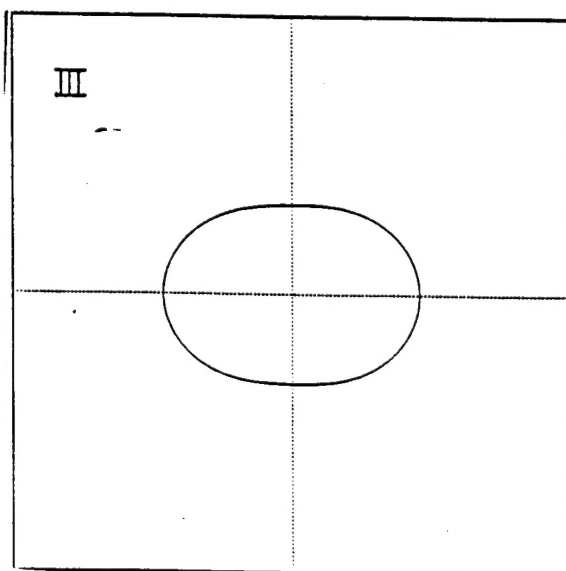
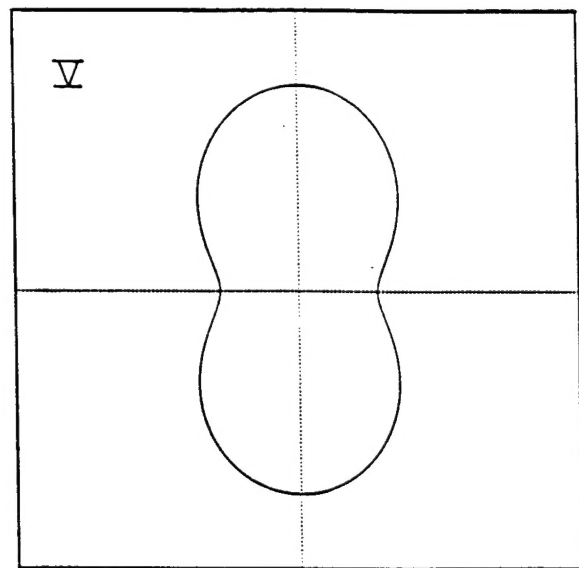
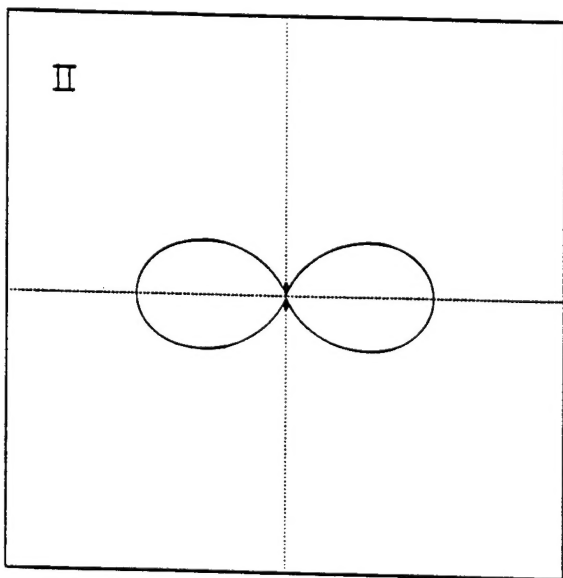
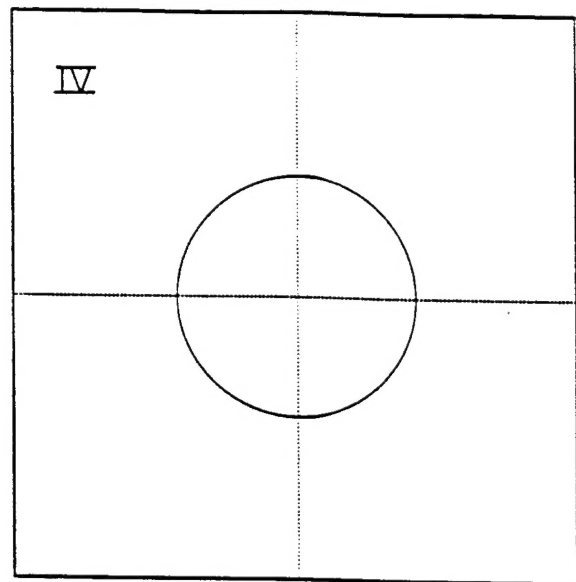
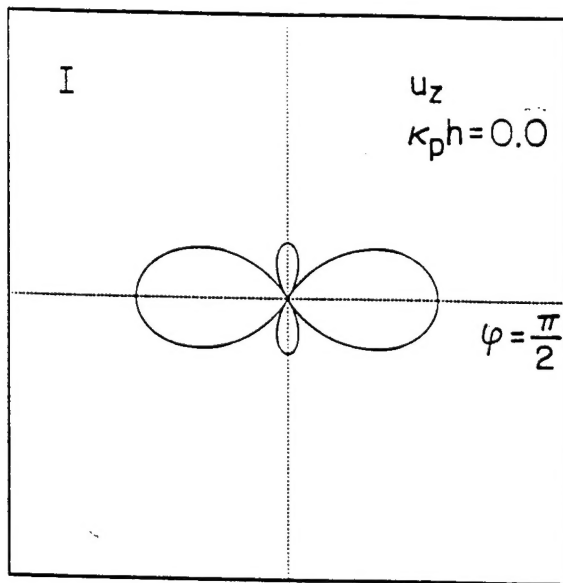


Fig. 11
-99-

$$\varphi = 0$$

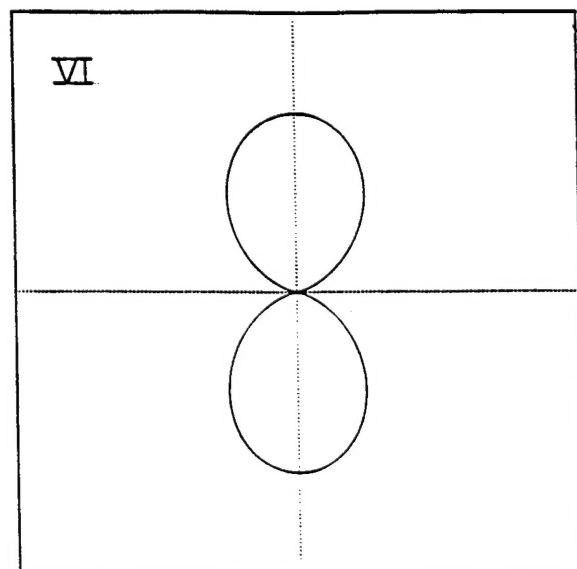
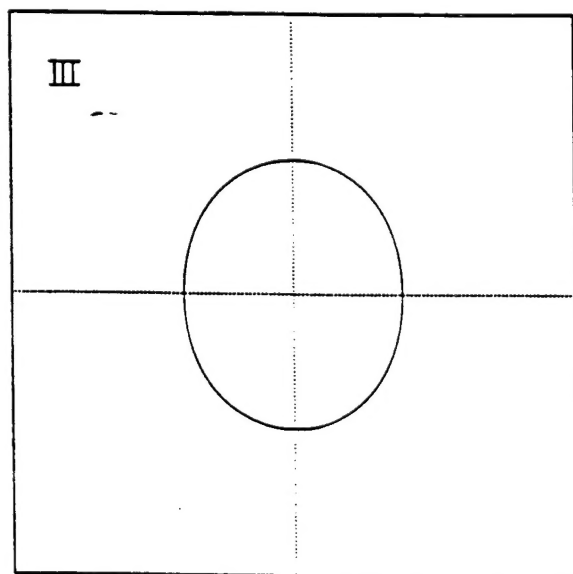
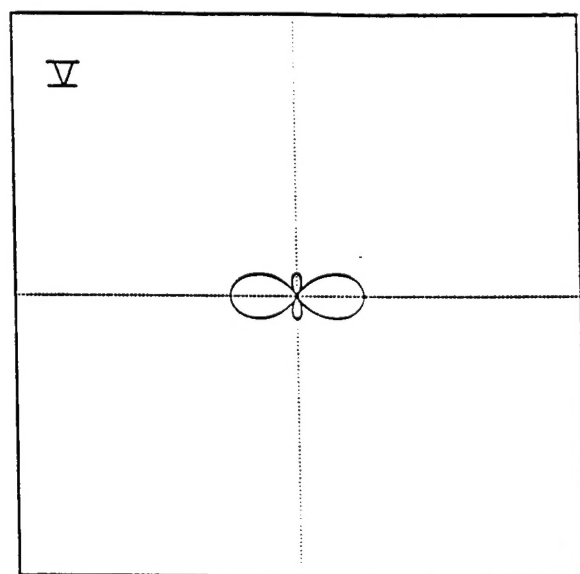
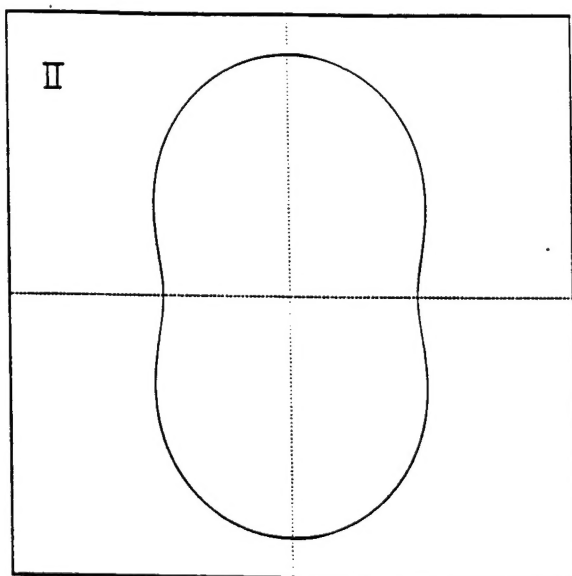
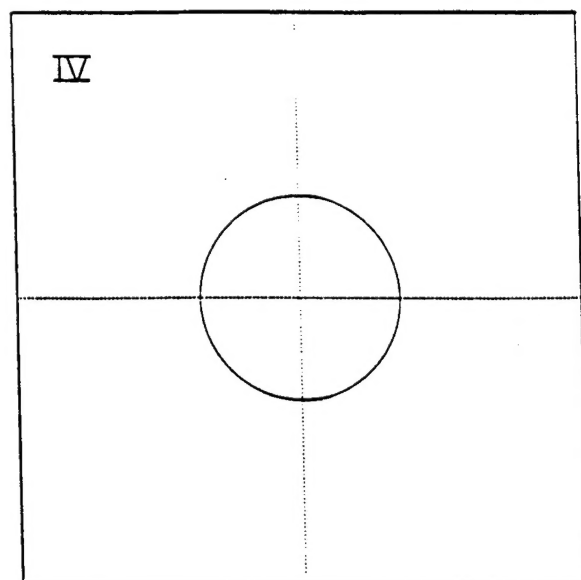
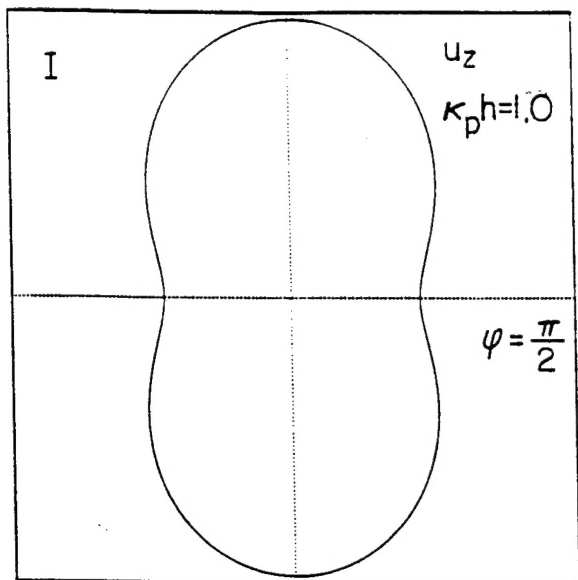


Fig. 12-

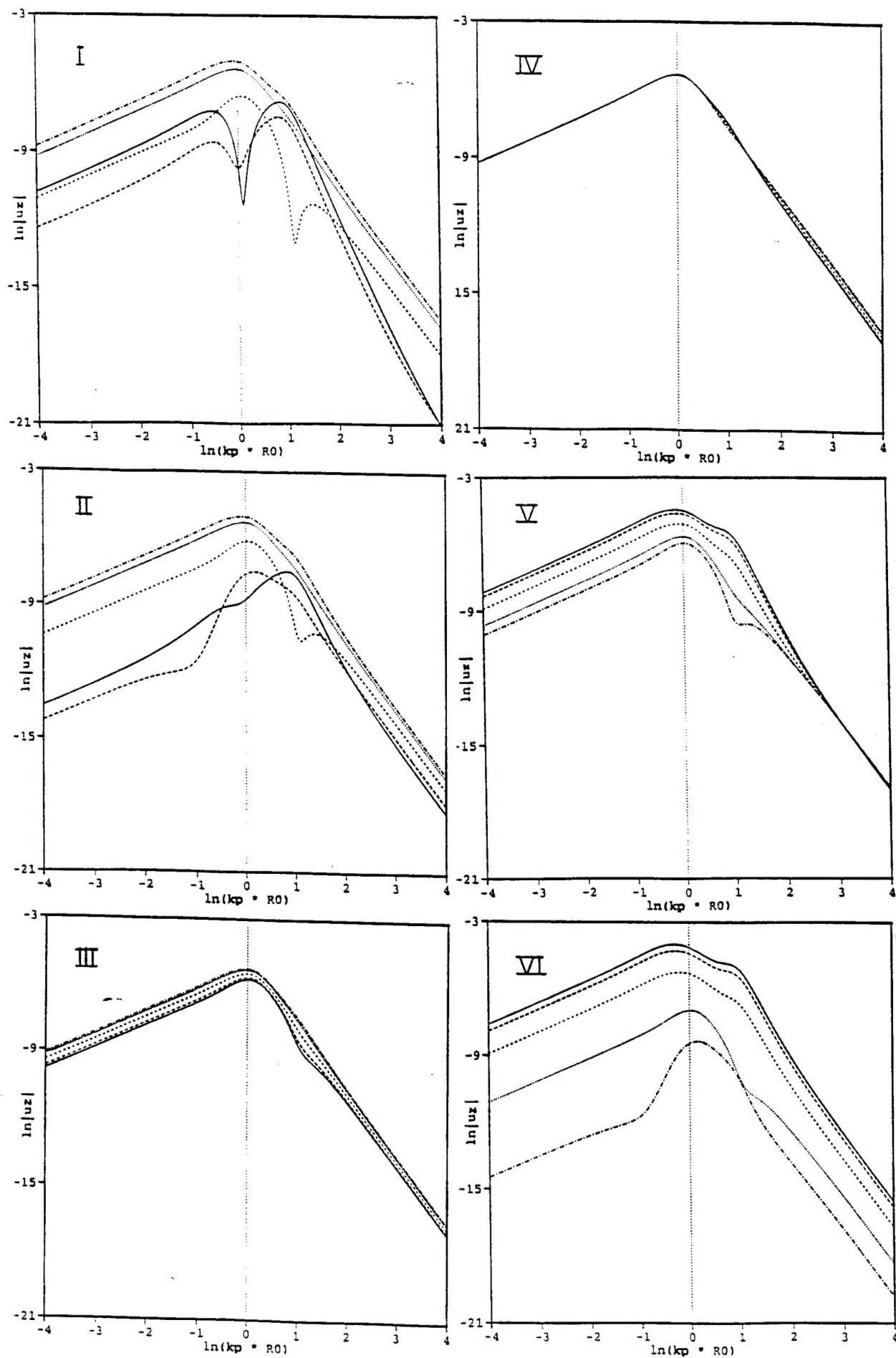


Fig. 13
-101-

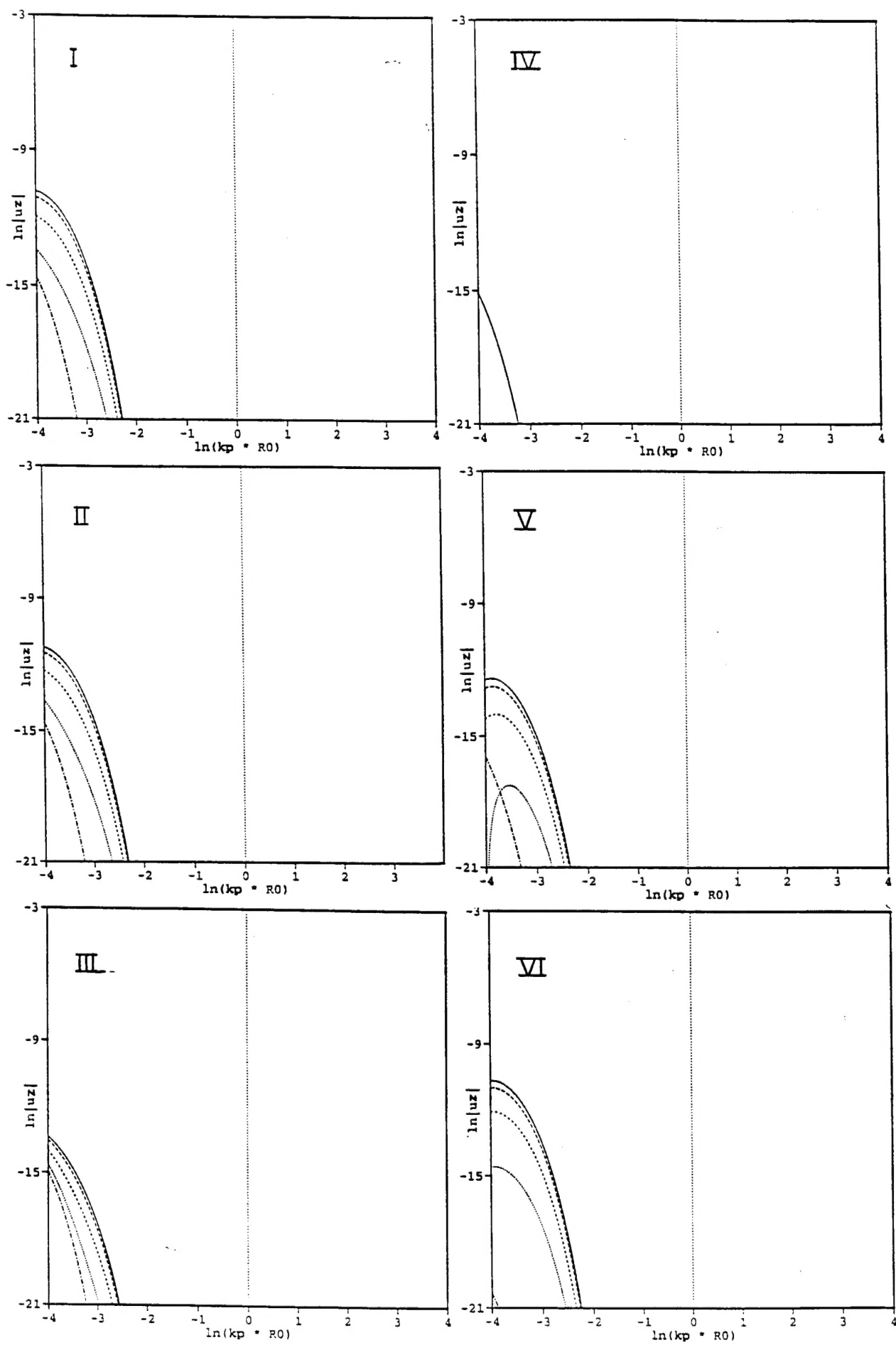


Fig. 14